

Aspects of reduced-order modeling of turbulent channel flows: From linear mechanisms to data-driven approaches

Thesis by
Ryan Michael McMullen

In Partial Fulfillment of the Requirements for the
Degree of
Doctor of Philosophy in Aeronautics

The logo for the California Institute of Technology (Caltech), featuring the word "Caltech" in a bold, orange, sans-serif font.

CALIFORNIA INSTITUTE OF TECHNOLOGY
Pasadena, California

2020
Defended May 15, 2020

© 2020

Ryan Michael McMullen
ORCID: 0000-0003-1371-7150

All rights reserved

ACKNOWLEDGEMENTS

Despite the individual nature of graduate research, a PhD is not achieved in isolation. Accordingly, there are many people to whom I am extremely grateful. Each has in some way made my time at Caltech thoroughly enjoyable and rewarding.

First, funding from the Office of Naval Research under grant N00014-17-1-3022 and from Air Force Office of Scientific Research under grant FA 9550-16-1-0361 is gratefully acknowledged. Next, I would like to thank Dan Meiron, Tony Leonard, and Mike Graham agreeing to be on my thesis committee, and for their helpful comments and suggestions for the thesis. I am especially grateful to Mike for his guidance and encouragement, as well as for teaching me a great deal about viscoelastic fluid mechanics.

Even before I came to Caltech, I hoped to join Beverley McKeon's group, and looking back now, I can say without hesitation that, given the opportunity to make the decision over again, I would make the same choice. It is virtually impossible to express all the ways in which she has guided and inspired my growth as a researcher. As a scientist, mentor, and person, I think one would have a hard time finding a better role model.

I also believe it's no coincidence that Beverley has attracted such an incredible collection of people to the McKeon research group. I am indebted to all students and postdocs past and present, from which I have learned many things about turbulence, fluid mechanics, and beyond. Additionally, I have them to thank for all of the experiences – from weekly group lunches, bad movie nights, and supper club, to mid-afternoon conversations that always managed to rope in the entire office – that made the day in, day out of grad school a bit more tolerable. As strange as it sounds, I will miss our crowded, windowless office, which is a testament to how much I enjoyed interacting with everyone. I can only hope the rest of my career will be filled with similarly brilliant, thoughtful, and friendly colleagues.

The group could not operate without the help of our administrators over the years: Jamie Meighen-Sei, Denise Ruiz, and Liza Bradulina. I would also like to thank Jamie for the many conversations, for opening her home to the group for what was one of the best meals I've had in my entire life, and for understanding, possibly better than anyone, how much I love Jones Coffee. In addition, I am lucky that GALCIT has had a host of incredible department administrators: Christine Ramirez, Dimity

Nelson, Peggy Blue, and Anne Lindline. I would like to thank all of them for all the work they do, often behind the scenes, to keep everything running smoothly. I am also grateful to Jackie Gish, who volunteered her time to provide me with invaluable feedback on resumes, cover letters, and interviews.

During my time at Caltech, I was fortunate enough to have multiple opportunities to spend time at other institutions. First, the exchange program between GALCIT and École Polytechnique was truly enriching from both an educational standpoint and as a life experience, and I thank everyone involved in organizing the program at both schools for making it possible. More recently, Mike Graham graciously hosted me at the University of Wisconsin-Madison for several weeks. He and his group immediately made me feel welcome, and I learned a great deal from them, even in the short time I was there. In particular, I would like to thank Alec Linot for patiently teaching me about TensorFlow, and Ashwin Shekar for our continued collaborations.

Outside academics, there are many people who have had a major impact on my life and happiness during this time. First, I'd like to thank my first-year roommates, Rich Kennedy and Ian Brownstein. Though both of them ultimately pursued PhDs elsewhere, I am glad we have still kept in touch regularly. The year Rich and I spent in France was one of the best of my life, and I'll always miss walking to our favorite boulangerie to stuff our faces with fresh baguettes. I am lucky to have Ian as a friend and admire his constant drive to plan camping and backpacking trips. Without him, I likely would not have experienced so many amazing weekend trips in California's mountains and deserts, or a nine-day circuit of Iceland. Notably, It was also with Ian that I first experienced Carmela Ice Cream.

During my third year, I took a chance and moved into a house with some other students that I hardly knew. It turned out to be arguably the best decision I made at Caltech. I thoroughly enjoyed living with Nate Thomas, Nick Weadock, Andrew Robbins, Dylan Tozier, Kelly Mauser, and Soichi Hirokawa, who helped make the two years at Steuben house truly feel like home. While most of them have since moved on to bigger and better things, I'm glad that Soichi and I could continue living together, and my appreciation for him as a roommate and friend has only been cemented during our recent time quarantined during the COVID-19 pandemic. I'm also thankful that Nate and his wife, Sarah, decided to remain local and have on numerous occasions generously invited me over and fed me.

I would like to acknowledge all of the people with whom I've spent many, many

hours playing Dungeons & Dragons. Each campaign has been a blast, and I have always enjoyed getting together to share the (real) three pillars of D&D: food, beers, and laughs.

I've been extremely lucky to have some very close friends throughout my life, none more so than Wes Hiatt and Ryan Murphy. I've long since lost track of how many concerts Ryan and I have been to together over the past dozen or so years, but I hope to go to countless more until we become the "old guys" in the crowd. Though Wes' stint in Los Angeles was brief, I'm glad we were able to share some Pasadena favorites, including Lucky Boy breakfast burritos and, of course, Jones Coffee.

Lastly, I would like to thank my mom and dad. Here again, words are wholly insufficient. Without their endless love and support, I could not have done any of this.

ABSTRACT

This thesis concerns three key aspects of reduced-order modeling for turbulent shear flows. They are linear mechanisms, nonlinear interactions, and data-driven techniques. Each aspect is explored by way of example through analysis of three different problems relevant to the broad area of turbulent channel flow.

First, linear analyses are used to both describe and better understand the dominant flow structures in elastoinertial turbulence of dilute polymer solutions. It is demonstrated that the most-amplified mode predicted by resolvent analysis (McKeon and Sharma, 2010) strongly resembles these features. Then, the origin of these structures is investigated, and it is shown that they are likely linked to the classical Tollmien-Schlichting waves.

Second, resolvent analysis is again utilized to investigate nonlinear interactions in Newtonian turbulence. An alternative decomposition of the resolvent operator into Orr-Sommerfeld and Squire families (Rosenberg and McKeon, 2019b) enables a highly accurate low-order representation of the second-order turbulence statistics. The reason for its excellent performance is argued to result from the fact that the decomposition enables a competition mechanism between the Orr-Sommerfeld and Squire vorticity responses. This insight is then leveraged to make predictions about how resolvent mode weights belonging to several special classes scale with increasing Reynolds number.

The final application concerns special solutions of the Navier-Stokes equations known as exact coherent states. Specifically, we detail a proof of concept for a data-driven method centered around a neural network to generate good initial guesses for upper-branch equilibria in Couette flow. It is demonstrated that the neural network is capable of producing upper-branch solution predictions that successfully converge to numerical solutions of the governing equations over a limited range of Reynolds numbers. These converged solutions are then analyzed, with a particular emphasis on symmetries. Interestingly, they do not share any symmetries with the known equilibria used to train the network. The implications of this finding, as well as broader outlook for the scope of the proposed method, are discussed.

PUBLISHED CONTENT AND CONTRIBUTIONS

McMullen, R. M., Rosenberg, K., and McKeon, B. J. (2020). “Interaction of forced Orr-Sommerfeld and Squire modes in a low-order representation of turbulent channel flow”. arXiv: 2001.02785 [physics.flu-dyn].
Performed the optimizations, analyzed the data, and was the primary author of the paper.

Shekar, A., McMullen, R. M., McKeon, B. J., and Graham, M. D. (2020). “Self-sustained elastoinertial Tollmien-Schlichting waves”. *Journal of Fluid Mechanics*. To appear.
Performed the linear analyses, generated figures, and was the primary author of the section *Linear analyses*.

Shekar*, A., McMullen*, R. M., Wang, S.-N., McKeon, B. J., and Graham, M. D. (2019). “Critical-Layer Structures and Mechanisms in Elastoinertial Turbulence”. *Phys. Rev. Lett.* 122 (12). DOI: 10.1103/PhysRevLett.122.124503, p. 124503.
*Equal contribution. Performed the linear analyses, processed the 3D EIT data, generated figures, and was the primary author of the section *Linear analyses*.

McMullen, R. M., Shekar, A., Graham, M. D., and McKeon, B. J. (2018). “Weissenberg number dependence of linear mechanisms in polymer drag-reduced turbulent channel flow”. *12th International ERCOFTAC Symposium on Engineering Turbulence Modelling and Measurements*.
Performed the linear analyses and was the primary author of the paper.

TABLE OF CONTENTS

Acknowledgements	iii
Abstract	vi
Published Content and Contributions	vii
Table of Contents	vii
List of Illustrations	x
List of Tables	xvi
Chapter I: Introduction	1
1.1 Wall-bounded turbulence and coherent structures	2
1.2 Turbulent drag reduction via polymer additives	3
1.3 Systems approaches to nonlinear interactions in wall-bounded turbulence	6
1.4 Exact coherent states	8
1.5 Objectives and organization of the thesis	10
Chapter II: Preliminaries of resolvent analysis	12
2.1 The resolvent operator	12
2.2 Decomposition of the resolvent and low-order approximation	13
Chapter III: Linear analyses of elastoinertial turbulence in channels	16
3.1 Chapter overview	16
3.2 Formulation for viscoelastic fluids	17
3.3 Weissenberg number dependence of linear mechanisms in viscoelastic channel flow	25
3.4 Critical layer mechanisms and structures in EIT	32
3.5 Chapter summary	43
Chapter IV: Interaction of forced Orr-Sommerfeld and Squire modes in a low-order representation of turbulent channel flow	47
4.1 Formulation	47
4.2 Analysis of the optimized spectra	54
4.3 Weights scaling for the universal classes of resolvent modes	71
4.4 Discussion	84
Chapter V: A data-driven approach for generating initial guesses of exact coherent states	88
5.1 Chapter overview	88
5.2 Methods	90
5.3 Results	96
5.4 Discussion	100
Chapter VI: Conclusions and future work	104
Bibliography	108
Appendix A: Additional details of the viscoelastic resolvent formulation	118
A.1 Base flow	118

A.2 Operator definitions	119
A.3 Geometric inner product	120
A.4 Implementation in resolvent code	121
Appendix B: Universal scaling of the Orr-Sommerfeld and Squire resolvent operators	122
B.1 Outer class	122
B.2 Geometrically self-similar class	124

LIST OF ILLUSTRATIONS

<i>Number</i>	<i>Page</i>
2.1 Schematic of resolvent analysis. “IFT” and “FT” denote the inverse and forward Fourier transforms, respectively.	13
3.1 Schematic of the bead-spring dumbbell model for a polymer molecule; \mathbf{p} is the end-to-end vector.	18
3.2 Mean velocity profiles in inner units for $Wi = 0$ (red), $Wi = 7$ (blue), and $Wi = 20$ (green). Also shown are the Kármán log law $U^+ = 2.5 \log y^+ + 5.5$ (solid gray) and the Virk asymptote $U^+ = 11.7 \log y^+ - 17.0$ (dashed gray).	26
3.3 (a) Snapshot of flow structures for $Wi = 7$ in the lower half of the domain: Isosurface of vortex strength $Q = 0.075$, color-coded blue to red based on increasing distance from the wall, and polymer stretch $\text{tr} \tilde{\mathbf{r}}$ in the planes $x = 0$ and $z = 5$; lighter contours indicate high levels. Inset is the time averaged spatial spectrum of v at $y = 0$; significant spectral content is indicated by lighter contours. (b) Same as in (a) for $Wi = 20$, but with $Q = 0.00014$	28
3.4 H_∞ norms of (a),(c) $\mathcal{H}_{x \rightarrow u}$ and (b),(d) $\mathcal{H}_{y \rightarrow u}$, with (a),(b) $Wi = 7$; (c),(d) $Wi = 20$	29
3.5 H_∞ norms of (a),(c) $\mathcal{H}_{x \rightarrow r_{xx}}$ and (b),(d) $\mathcal{H}_{y \rightarrow r_{xx}}$, with (a),(b) $Wi = 7$; (c),(d) $Wi = 20$	31
3.6 Comparison of r_{xx} from DNS and resolvent analysis at $Wi = 20$. The top half of the channel shows the $z = L_z/2$ plane from a DNS snapshot, and the bottom half shows the leading resolvent mode for $(k_x, k_z, \omega) = (1.26, 0, 0.46)$	33
3.7 Comparison of r_{xx} from DNS and resolvent analysis at $Wi = 20$. The same DNS snapshot and resolvent mode shown in Figure 3.6 are shown in the $x = L_x/2$ plane.	34

- 3.8 Scaled friction factor vs. Wi at $Re = 1500$. Abbreviations “NT”, “L” and “EIT” stand for Newtonian-like turbulence, laminar, and elastoinertial turbulence, respectively. In most cases, the error bars are smaller than the symbols. Red dotted lines indicate the intervals of Wi in which the NT solution loses existence and the EIT solution comes into existence, respectively, as Wi increases. Inset shows the spatial spectrum of the wall normal velocity at $y = 0$ for $Wi = 20$. Here, x - and z -wavenumbers k_x and k_z are reported in scaled form, as $k_x L_x / 2\pi$ and $k_z L_z / 2\pi$. For inset, low is blue, high is yellow. Reproduced from Shekar et al. (2019). 35
- 3.9 (a) Eigenvalue spectrum for $(k_x L_x / 2\pi, k_z L_z / 2\pi) = (2, 0)$ with $Wi = 20$ and $Re = 1500$. The eigenvalue labeled “TS” corresponds to the TS mode. (b) Leading singular value of the resolvent operator for the same wavenumbers and Reynolds number as in (a) and $Wi = 0$ (red) and $Wi = 20$ (blue). Reproduced from Shekar et al. (2019). 37
- 3.10 (a) Snapshot of v (line contours) and r_{xx} (filled contours) from 3D nonlinear DNS at $Re = 1500$, $Wi = 20$. (b) Phase-matched average $(k_x L_x / 2\pi, k_z L_z / 2\pi) = (2, 0)$ structures from 3D DNS. (c) Structure of the TS mode for $Re = 1500$, $Wi = 20$, and the same wavenumbers as in (b). (d) Structure of the most strongly amplified resolvent mode for $Re = 1500$, $Wi = 20$, the same wavenumbers as in (b), and $c = 0.37$. In all plots, contour levels are symmetric about zero. For v , dashed and solid contours indicate negative and positive values, respectively. For r_{xx} , black, red, and yellow indicate negative, zero, and positive values, respectively. Reproduced from Shekar et al. (2019). 40
- 3.11 Zoomed view of the TS mode r_{xx} (filled contours) and streamlines (line contours) in a reference frame co-moving with the wave for $Re = 1500$, $Wi = 20$. For r_{xx} , blue, white, and red indicate negative, zero, and positive values, respectively. 41
- 3.12 Structure of nonlinear self-sustaining TS wave at $Re = 3000$, $Wi = 3$. White streamlines, shown in a reference frame moving with the wavespeed $c = 0.39$, are superimposed on color contours of \tilde{r}_{xx} . Green lines indicate the instantaneous critical layer positions, and white dots indicate the locations of hyperbolic stagnation points. Reproduced from Shekar et al. (2019). 42

- 3.13 (a) Solid blue line: ratio of peak amplitudes of \hat{r}_{xx} and \hat{v} for the linear TS mode as a function of Wi ; circles: amplitude ratio for the VNTSA. (b) Magnitude of \hat{r}_{xx} for the linear TS mode for several values of Wi in the range $[1, 20]$. Darker lines indicate higher values of Wi . The thick red line shows the averaged magnitude of \hat{r}_{xx} from the VNTSA for $Wi = 13$. For comparison, the linear TS mode profile for the same Wi is shown in blue, and the vertical dashed line marks the critical layer location $y_c = 0.825$. The arrow indicates the value of Wi corresponding to the arrow in (a). 44
- 4.1 Premultiplied one-dimensional spectra from the resolvent (filled contours) and DNS (black contours) for $Re_\tau = 2003$. (a,c,e,g) Standard resolvent decomposition using $N = 6$ modes per wavenumber-frequency triplet; (b,d,f,h) OS-SQ resolvent decomposition using $N^{OS} = N^{SQ} = 3$ modes per wavenumber-frequency triplet. (a,b) $k_x E_{uu}$, (c,d) $k_x E_{vv}$, (e,f) $k_x E_{ww}$, (g,h) $-k_x E_{uv}$. Contour levels are from 10% to 90% of the DNS maximum in 20% increments. 55
- 4.2 Intensities from the resolvent with $N^{OS} = N^{SQ} = 3$ modes per wavenumber-frequency triplet (blue) and DNS (black) for $Re_\tau = 2003$. Also shown in dashed lines are the intensities obtained from the standard resolvent decomposition approach using the same total number of modes. 57
- 4.3 Relative errors in $\langle u^2 \rangle$ (blue), $\langle v^2 \rangle$ (red), $\langle w^2 \rangle$ (green), and $\langle -uv \rangle$ (orange), as a function of $N^{OS} = N^{SQ} = N$ 58
- 4.4 Comparison of DNS (black) and the optimization results with $y_{\min}^+ = 5$ (red) and $y_{\min}^+ = 50$ (green) using $N^{OS} = N^{SQ} = 6$ modes for $(\lambda_x^+, \lambda_z^+) \approx (3.83 \times 10^4, 2.78 \times 10^3)$ 59
- 4.5 2D premultiplied streamwise velocity power spectra at $y^+ \approx 15$ for $Re_\tau = 185$. (a) $\omega k_x E_{uu}$, (b) $\omega k_z E_{uu}$. Filled contours: Optimized weights with $N^{OS} = N^{SQ} = 3$. Line contours: DNS; levels are 10% (thin) and 50% (thick) of the maximum value. The slope of the dashed line indicates the the local mean velocity $U(y^+ = 15)$ 61
- 4.6 2D forcing spectra at $y^+ \approx 15$ for $Re_\tau = 185$. (a) $E_{g_v g_v}$, (b) $E_{g_\eta g_\eta}$. Filled contours: Optimized weights with $N^{OS} = N^{SQ} = 3$. Line contours, reproduced from Rosenberg (2018): DNS; levels are 10% (thin) and 50% (thick) of the maximum value. 63

- 4.7 Magnitudes of the total leading mode coefficients (a) $\sigma_1^{\text{OS}} \sqrt{X_{11}^{\text{OS/OS}}}$, (b) $\sigma_1^{\text{SQ}} \sqrt{X_{11}^{\text{SQ/SQ}}}$ larger than 1% of the maximum value over all of spectral space for $Re_\tau = 2003$. Marker sizes are proportional to the magnitude and are normalized by the maximum. The axes show the full range of wave parameters included in the optimization. 64
- 4.8 (a) First ten singular values of the OS (blue), SQ (red), and standard (black) resolvent operators for $(k_x, k_z, c) = (0.25, 2.5, 24)$ and $Re_\tau = 2003$. (b)-(d) Magnitudes of the vorticity responses from the first, second, and third mode pairs (same color scheme as in (a)); modes having the same wall-normal symmetry have been selected from each pair. The standard resolvent (black) and OS (blue) modes are visually indistinguishable. The gray lines in (b)-(d) are the locations of the critical layers, $y_c = \pm 0.194$ 67
- 4.9 (a),(c),(e) Magnitudes of the forcing modes corresponding to the response modes shown in Figure 4.8, using the same color scheme. ϕ_v for the standard resolvent (solid black) is indistinguishable from OS (blue). Dotted lines are the standard resolvent ϕ_η . Gray lines are the locations of the critical layers, $y_c = \pm 0.194$. (b),(d),(f) SQ and standard resolvent ϕ_η normalized by their maximum values. 68
- 4.10 (a) $\langle u^2 \rangle$, (b) $\langle w^2 \rangle$, (c) $\langle -uv \rangle$ decomposed into OS (blue), SQ (red), and C (green) terms for $N = 3$. The totals are plotted in black. 69
- 4.11 (a) Mean velocity profile $U(y^+)$ and (b) velocity defect $U_{cl} - U(y)$ for $Re_\tau = 934$ (blue), $Re_\tau = 2003$ (red), and $Re_\tau = 4219$ (green). The gray boxes indicate the regions where the profiles are Re_τ -invariant in the respective coordinates. 72
- 4.12 (a) Magnitudes of the scaled OS, SQ, and standard resolvent (color scheme as in Figure 4.8) inner-class leading vorticity response modes for the three Re_τ shown in Figure 4.11, with $k_x^+ = 1/934$, $k_z^+ = 10k_x^+$, and $c = 10$. (b) Corresponding scaled leading forcing mode magnitudes, with the relevant axes indicated by the arrows. ψ_η and ϕ_v for the standard resolvent are indistinguishable from the OS modes. The gray line indicates the location of the critical layer. 75

- 4.13 Leading weights ratio for $Re_\tau = 934$ (blue), $Re_\tau = 2003$ (red), and $Re_\tau = 4219$ (green) with $N = 3$ for several different wavelengths: (a) $(k_x^+, k_z^+) = (2\pi/10^2, 2\pi/10^2)$; (b) $(k_x^+, k_z^+) = (2\pi/10^3, 2\pi/10^2)$; (c) $(k_x^+, k_z^+) = (2\pi/10^3, 2\pi/10^3)$; (d) $(k_x^+, k_z^+) = (2\pi/10^4, 2\pi/10^3)$. Filled circles denote modes belonging to the universal inner class, and the highest inner class wavespeed, $c = 16.4$, is indicated by the gray line. 77
- 4.14 (a) Magnitudes of the scaled OS, SQ, and standard resolvent (color scheme as in Figure 4.8) outer-class leading vorticity response modes for the three Re_τ shown in Figure 4.11, with $\tilde{k}_x = 934$, $\tilde{k}_z = \gamma = 1.5\sqrt{10}$, and $U_{cl} - c = 1$. (b) Corresponding scaled leading forcing mode magnitudes. ψ_η and ϕ_v for the standard resolvent are indistinguishable from the OS modes. The gray line indicates the location of the critical layer. 78
- 4.15 (a)-(d) Leading weights ratio for $Re_\tau = 934$ (blue), $Re_\tau = 2003$ (red), and $Re_\tau = 4219$ (green) with $N = 2$. (e)-(h) Weights ratio scaled according to Equation (4.40). Each column represents a different scaled streamwise wavenumber \tilde{k}_x : (a),(e) $\tilde{k}_x = 4219$; (b),(f) $\tilde{k}_x = 8438$; (c),(g) $\tilde{k}_x = 12657$; (d),(h) $\tilde{k}_x = 16876$. In all cases the spanwise wavenumber is $k_z = \gamma\tilde{k}_x/Re_{\tau,\min}$, with $\gamma = \sqrt{10}$. Filled circles denote modes belonging to the universal outer class, and the largest outer class wavespeed defect, $U_{cl} - c = 6.17$, is indicated by the gray line. 81
- 4.16 (a) Magnitudes of the scaled OS, SQ, and standard resolvent (color scheme as in Figure 4.8) self-similar leading vorticity response modes for five members of a hierarchy at $Re_\tau = 2003$, with $k_{x,l} = 10$ and $k_{z,l} = 10^{3/2}$. (b) Corresponding scaled leading forcing mode magnitudes. ψ_η and ϕ_v for the standard resolvent (black) are indistinguishable from the OS modes (blue). 83
- 4.17 Leading weights ratio along hierarchies for $Re_\tau = 2003$ with $N = 2$. Each panel is a different hierarchy, represented by the streamwise wavenumber at the bottom of the hierarchy: (a) $k_{x,l} = 1$; (b) $k_{x,l} = 5$; (c) $k_{x,l} = 10$; (d) $k_{x,l} = 20$. In all cases, the spanwise wavenumber at the bottom of the hierarchy is $k_{z,l} = \gamma k_{x,l}$, with $\gamma = 5$. The solid gray lines are the least-squares linear fits, with slopes (a) 0.158, (b) 0.145, (c) 0.107, and (d) 0.069. The dashed gray lines are $y^+ = 2.6Re_\tau^{1/2} \approx 116$. 85

5.1	Schematic of “branch jumping”. “UB” and “LB” denote upper- and lower-branch solutions, respectively, and A is some measure of amplitude used to construct the bifurcation diagram. The closed circle represents a known LB solution, the open circle represents the desired UB solution, and \mathcal{F} is the proposed mapping between the two.	89
5.2	Schematic of the neural network “workflow”.	90
5.3	Bifurcation diagram for EQ1-2 (blue) and EQ3-4 (red).	92
5.4	Streamwise-averaged velocity fields of EQ2 (top) and EQ1 (bottom) for $Re \approx 500$. Contours: u , vectors: v, w .	93
5.5	Streamwise-averaged velocity fields of EQ4 (top) and EQ3 (bottom) for $Re \approx 500$. Contours: u , vectors: v, w .	94
5.6	Comparison of EQ2 (left) and the neural network prediction (right) in the plane $x = 0$ for $Re = 1148$. u : top, v : middle, w : bottom.	98
5.7	Comparison of EQ4 (left) and the neural network prediction (right) in the plane $x = 0$ for $Re = 1209$. u : top, v : middle, w : bottom.	99
5.8	Comparison of streamwise averages for EQ2 (left) and the converged state using the neural network initial guess (center), as well as their difference (right) for $Re = 1148$. u : top, v : middle, w : bottom.	101
5.9	Comparison of streamwise averages for EQ4 (left) and the converged state using the neural network initial guess (center), as well as their difference (right) for $Re = 1209$. u : top, v : middle, w : bottom.	102

LIST OF TABLES

<i>Number</i>	<i>Page</i>
4.1 Resolutions of the DNS from which spectra were obtained for the optimization. N_{sp} is the number of planes for which spectra are available.	54
5.1 Details of the neural network architecture.	95

Chapter 1

INTRODUCTION

Turbulence is pervasive. From weather patterns, to ocean currents, to jet engine combustors, it plays a central role in many areas that directly affect daily life. Consequently, the ability to make quantitative predictions about how turbulence behaves is vital for many areas of science and engineering. Unfortunately, a comprehensive theory of turbulence remains elusive after more than a century of research. To appreciate why, one need only drop food coloring in water or stir milk into coffee. What emerges are captivating, astoundingly complex motions of myriad sizes evolving on myriad time scales, all of which influence each other. To get a sense of the complexity turbulence researchers are confronted with, consider the Reynolds number (Re), which quantifies the relative importance of fluid inertia to viscous forces. In turbulent flows, Re also serves as an indicator of the range of length scales present. Typical Re for some real-world systems, including flow over the hull of a cargo ship and the atmospheric surface layer, can be as large as $O(10^5 - 10^7)$ (Smits and Marusic, 2013).

Absent a complete theory, engineers have largely relied on empiricism to determine quantities of interest, such as the drag force on an aircraft wing. While empirical approaches have been enormously successful in aviation and elsewhere, there are still limitations to what can be learned. For example, performing experiments to measure every bit of desired information for every iteration of an aircraft design is clearly infeasible. Similarly, although the advent of high-performance computing has enabled the simulation of some turbulent flows, most that are of technological relevance still lie beyond the capabilities of even the largest modern supercomputers and likely will for some time.

This underscores the need for models of reduced complexity, but which still retain the physics essential for making useful predictions. Simplified models are, of course, not a new idea. However, many of the ones developed for turbulence are largely based on phenomenology, which means that they are unlikely to generalize well. Ideally then, a “reduced-order” model should be produced in some principled fashion.

The purpose of this chapter is to briefly introduce and provide some background for

the concepts discussed at length in subsequent chapters.

1.1 Wall-bounded turbulence and coherent structures

Many turbulent flows of practical significance involve motion past a solid bounding surface. Such flows are categorized as wall-bounded turbulence. The presence of a wall has several important implications. The first is that the geometry of the surface imposes a length scale on the flow, which determines the size of the largest turbulent motions. Second, friction causes the velocity of the fluid relative to the surface to be zero at the wall. Through viscosity, this effect is felt a finite distance from the wall, resulting in a wall-normal gradient of the mean velocity. Importantly, this mean velocity gradient, or mean shear, acts as a source for the production of turbulent fluctuations. For this reason, wall-bounded turbulence, unlike turbulence in the absence of a mean shear, is said to be self-sustaining.

Central to the mechanisms through which wall-bounded turbulence self-sustains are so-called coherent structures. While there is no consensus on a precise definition of a coherent structure (Marusic et al., 2010), they can be broadly described as recurring motions that exhibit spatiotemporal coherence according to some metric. A large body of literature on coherent structures in wall-bounded flows has been produced in recent decades, and a comprehensive review is beyond the scope of this chapter. Instead, we merely identify several classes relevant to the present work.

Close to the wall, alternating low- and high-speed streaks of streamwise velocity flanked by streamwise-oriented vortices comprise what is known as the near-wall cycle (NWC). Significantly, it has been argued that the regeneration cycle of the streaks and vortices is the fundamental process through which near-wall turbulence is sustained (Hamilton et al., 1995). The NWC also has a significant statistical signature, with it being responsible for the peak of the streamwise velocity fluctuation variance close to the wall. It has been proposed that the near-wall vortices form the legs of larger structures known as “hairpin” vortices (Adrian, 2007). Further, individual hairpin vortices can generate secondary hairpins upstream and downstream of the primary one, creating a hairpin “packet” (Zhou et al., 1999), and these packets are hypothesized to be the constituent elements of large scale motions (LSMs) associated with turbulent bulges in the outer region of the flow (Adrian, 2007). Finally, at sufficiently high Re , even larger motions, termed very large-scale motions (VLSMs) or superstructures, emerge and contribute as much as half of the turbulent kinetic energy (Kim and Adrian, 1999; Guala et al., 2006; Hutchins and

Marusic, 2007).

From a reduced-order modeling standpoint, the persistence and energetic dominance of coherent structures is encouraging, as they support the view that, despite the complexity of wall-bounded turbulence, perhaps much of the crucial dynamics can be described in terms of a small set of (relatively) simple features.

1.2 Turbulent drag reduction via polymer additives

Since Toms (1948), it has been known that the addition of minute amounts of long, flexible polymers to a liquid can result in substantial turbulent drag reduction (DR). For example, addition of only 18 parts per million of polyethylene oxide of molecular weight $\sim 10^6$ to water can reduce the skin friction in pipe flow by roughly a third (Virk et al., 1967); other polymer solutions can achieve drag reduction as high as 80% (Virk, 1975). Due to the potentially enormous energy savings, polymer additives have been adopted in many industrial settings involving large-scale transport of fluids, the most famous example being in the Trans-Alaska pipeline (Burger et al., 1980; Burger et al., 1982).

The field of polymer DR has seen sustained research activity for over 70 years now. This is partly because, from a practical perspective, a better mechanistic understanding of how the significant DR is achieved could potentially enable a similar mechanism to be exploited via other means of flow control applicable in a broader class of flows. Fundamentally, the strong modifications to the turbulence imply an alteration of the processes that sustain it, situating polymer additives as a unique way to better understand them.

Early attempts at a theoretical explanation of polymer DR can be broadly classified as either viewing the effects of the polymers as primarily a local modification of the viscosity (Lumley, 1969; L'vov et al., 2004), or as the result of elastic energy being stored by the polymers (Tabor and de Gennes, 1986; de Gennes, 1990; Sreenivasan and White, 2000). The modified viscosity viewpoint posits that the intense turbulent fluctuations present in the buffer region of the flow near the wall cause the polymer molecules to be highly stretched, resulting in a dramatic increase in their extensional viscosity. This locally enhanced viscosity is then supposed to weaken the eddies, which thickens the buffer layer and reduces the mean wall shear. The elastic explanation argues that the strain rates in the buffer layer have too much spatiotemporal variation to fully extend the polymers, and instead that once the elastic energy stored in the partially-stretched molecules is comparable to

the kinetic energy contained in length scales larger than those for which viscous dissipation dominates, the cascade of energy from large to small scales will be truncated prematurely. Again, the hypothesized effect on the flow is a thickening of the buffer layer, leading to DR. Both theories have shown qualitative agreement with experiments and simulations, and it has been suggested that commonly-used models of the polymers formally admit both interpretations (Sreenivasan and White, 2000; White and Mungal, 2008), making it difficult to argue that one is superior to the other. One takeaway, however, is that such theories are likely too simplistic, in that they neglect many details of the complex polymer-flow interactions.

Fortunately, recent developments in both experimental measurement techniques and computing capabilities have enabled investigations of such interactions. For example, particle image velocimetry (PIV) has allowed detailed study of how turbulent structures are modified in the presence of polymers (Warholic et al., 2001; White et al., 2004). In particular, it has been observed that a decrease in number and strength of the near-wall quasi-streamwise vortices, typically associated with wall-ward transport of high momentum fluid, accompanies increasing DR (White et al., 2004). Using continuum-level models for the polymer molecules, direct numerical simulations give access to the state of the polymers in a turbulent flow, information that is largely unavailable using modern flow diagnostics. Such simulations also show a weakening of near-wall vortical activity and link it to polymers doing work against the vortices as they are drawn up between and subsequently stretched by them (Dubief et al., 2004; Dubief et al., 2005; Graham, 2014). The same mechanism also suppresses the autogeneration process of hairpin vortices (Kim et al., 2008). At high levels of drag reduction, the polymers are even responsible for sustaining the near-wall turbulence by injecting energy into the streamwise streaks as they relax (Dubief et al., 2005).

One of the most intriguing aspects of polymer DR is the existence of the maximum drag reduction (MDR) state, which is an experimental upper bound on the level of achievable drag reduction (Virk et al., 1970). MDR is, to a first approximation, independent of the details of polymer solution, e.g., concentration, molecular weight, and even the monomer itself (Virk, 1975; White and Mungal, 2008; Graham, 2014). Measurements of bulk flow rate at MDR collapse on a curve that depends logarithmically on Re , similar to the Newtonian case, but with different constants (Virk, 1975). This is often referred to as the MDR or Virk asymptote. From the MDR asymptote, Virk (1975) inferred that the mean velocity profile should also

obey a log-law. While there exist some phenomenological theories for the origin of a logarithmic MDR profile (e.g., L'vov et al., 2004), a close examination of simulation data indicates that the mean velocity profile in the MDR state is, in fact, not logarithmic (White et al., 2012). This is supported by recent analysis of the mean momentum balance using data from additional simulations (White et al., 2018) and experiments (Elsnab et al., 2019), which indicates that the region of inertial dynamics associated with logarithmic behavior of the mean velocity profile diminishes with increasing drag reduction, and that MDR corresponds to complete loss of logarithmic dependence.

Clearly, a comprehensive understanding of MDR remains elusive. One explanation, which originates from the dynamical systems view of turbulence, is that MDR corresponds to a state of “hibernating” turbulence (Graham, 2014), a low-drag state supposed to exist even in the Newtonian limit, in which case it is approached only infrequently. In this picture, the effect of increasing flow elasticity is to increase the frequency of excursions to the hibernating state, with MDR corresponding to the flow spending almost all of its time there. That is, the turbulence becomes marginalized by the action of the polymers (Graham, 2014). Support for this view comes from the existence of a family of traveling wave solutions for Newtonian pressure-driven flow in a channel, the “upper branch” of which has a mean profile resembling that of Newtonian turbulence, while the corresponding lower branch mean profile approaches the Virk log-law (Park and Graham, 2015). Moreover, averages of mean velocity profiles from experiments of transitional Newtonian channel flow conditioned on low drag events reveal similarities to these invariant solutions (Whalley et al., 2017).

Another explanation of MDR is related to elastoinertial turbulence (EIT), a novel chaotic state first observed in measurements of pipe flow at modest $Re = O(10^3)$ with high polymer concentrations (Samanta et al., 2013). Therefore, as the name suggests, the interplay of inertia and elasticity is believed to be important in EIT. It is thus distinct from so-called elastic turbulence, which exists in creeping flows of polymer solutions with curved streamlines (Groisman and Steinberg, 2000; Groisman and Steinberg, 2001). Notably, for sufficiently high levels of elasticity, EIT can be found at Re lower than that for the onset of turbulence in a Newtonian fluid (Samanta et al., 2013; Choueiri et al., 2018).

Simulations of EIT in channels (Samanta et al., 2013; Dubief et al., 2013; Terrapon et al., 2014; Sid et al., 2018) have elucidated its structure, which is found to be

markedly different from Newtonian turbulence or turbulence at modest levels of DR. The quasi-streamwise vortices and near-wall streamwise streaks are entirely absent, and the flow is instead dominated by very weak spanwise-oriented vortical structures. The polymers undergo large stretching in thin, highly inclined sheet-like structures that emanate from the near-wall region and are nearly two-dimensional (Samanta et al., 2013; Dubief et al., 2013). In fact, 2D simulations display qualitatively similar structures, implying that the mechanism of EIT is fundamentally two-dimensional (Sid et al., 2018). Additionally, PIV measurements (Choueiri et al., 2018) and simulations with long domains in pipes show the existence of weak, extremely long (~ 50 diameters) streamwise velocity structures.

Importantly, the friction factor scaling of EIT agrees with that for MDR, and, upon increasing Re , the mean velocity profile approaches the Virk profile, suggesting that the two states are linked (Samanta et al., 2013). Furthermore, it was shown that EIT is dynamically distinct from Newtonian turbulence. By gradually increasing polymer concentration, Choueiri et al. (2018) demonstrated that for Re sufficiently low but still above the transition Re for Newtonian fluids, the flow undergoes a reverse transition leading to relaminarization. Further increase in the concentration results in different instability, and the flow transitions directly into EIT. At higher Re , which has been the focus of the majority of the previous experimental and numerical studies, this elastic instability is apparently initiated before relaminarization occurs, yielding the classic picture of a continuous path between Newtonian turbulence and MDR (Choueiri et al., 2018).

1.3 Systems approaches to nonlinear interactions in wall-bounded turbulence

Techniques borrowed from developments in nonmodal stability theory (Trefethen et al., 1993; Jovanović and Bamieh, 2005; Schmid, 2007) have been met with much success in the analysis of wall-bounded turbulent shear flows. For example, analyses of the Navier-Stokes equations (NSE) linearized about the turbulent mean velocity predict the spanwise length scales associated with the near-wall cycle and large-scale structures in the outer region of the flow from both a transient growth (del Álamo and Jiménez, 2006; Cossu et al., 2009; Willis et al., 2010) and energy amplification of harmonic and stochastic forcing perspective (Hwang and Cossu, 2010; Willis et al., 2010). More recently, the linearized equations have been used to develop linear estimators (Illingworth et al., 2018; Madhusudanan et al., 2019; Towne et al., 2020) and compute impulse responses (Vadarevu et al., 2019) that qualitatively reproduce the coherence and self-similarity of large-scale motions.

As turbulence is an inherently nonlinear phenomenon, a complete model must account for nonlinear interactions. A common approach to incorporate the effects of nonlinearity into linear models is to augment the linearized equations with an eddy viscosity, such that the turbulent mean profile is fixed as an equilibrium solution of the modified mean momentum equation (del Álamo and Jiménez, 2006; Cossu et al., 2009; Willis et al., 2010; Hwang and Cossu, 2010; Illingworth et al., 2018; Madhusudanan et al., 2019; Vadarevu et al., 2019). While this approach justifies linearization about the turbulent mean profile, it precludes the study of finite-amplitude fluctuations, since their nonlinear interactions would feed back on and further alter the mean. Instead of using an eddy viscosity, Zare et al. (2017) considered colored-in-time stochastic forcing of the linearized NSE in the problem of completing partially-known second-order statistics. Notably, they demonstrated that their approach can be equivalently represented as a low-rank modification of the original equations.

In a different approach to dealing with nonlinearity, the resolvent analysis framework introduced by McKeon and Sharma (2010) retains the nonlinear term and interprets it as endogenous forcing of the linear dynamics through triadic interactions with the velocity fluctuations at other wavenumber-frequency combinations. This framework eliminates the need to incorporate an eddy viscosity for self-consistency, as no linearization is performed. Landahl (1967) arrived at a similar formulation, deriving a forced Orr-Sommerfeld equation in the study of wall-pressure fluctuations. However, Landahl sought approximate solutions in eigenfunction expansions, while resolvent analysis uses a gain-based approach, in which the fluctuations are expressed in terms of the most linearly amplified functions, obtained from a singular value decomposition of the resolvent operator associated with the linearized NSE.

Closure of the loop requires determination of the forcing such that it yields the correct velocity Fourier modes, as well as the mean velocity profile, which is assumed known. The forcing can be expanded as a sum over a set of basis functions such that the unknowns are the complex amplitudes, called the resolvent weights. An exact equation for the weights can be formulated (McKeon et al., 2013), though it is intractable to solve for most complex flows of interest. Consequently, there have been previous attempts to estimate the weights from data, e.g., by using either a single time series or power spectral density of the velocity fluctuations (Gómez et al., 2016; Beneddine et al., 2016). Alternatively, Moarref et al. (2014a) used convex optimization to compute the weights for a resolvent-based low-order representation

of time-averaged velocity spectra that minimize the deviation from spectra obtained from a direct numerical simulation (DNS) of channel flow (Hoyas and Jiménez, 2006). Towne et al. (2018) established a link between resolvent analysis and spectral proper orthogonal decomposition (SPOD) and showed that if the resolvent weights are treated as stochastic quantities, their covariance matrix can be calculated from the SPOD modes, which inherently rely on statistical data.

In special cases where full information of the nonlinear forcing is available, such as for exact coherent states (ECS), which are simple invariant solutions of the full NSE and will be discussed in detail in the next section, the resolvent weights can be computed exactly by projecting the forcing onto the aforementioned set of basis functions (Sharma et al., 2016). For ECS families in channel and pipe flow, which come in pairs of upper and lower branch solutions, the lower branch ones are typically well-represented by only a few resolvent modes, whereas many of the upper branch solutions are not captured as efficiently. Furthermore, the wall-normal and spanwise velocity components converge much more slowly than the streamwise velocity. However, an alternative decomposition of the resolvent operator recently proposed by Rosenberg and McKeon (2019b) yields two families of modes related to the Orr-Sommerfeld and Squire operators from classical linear stability theory. By projecting the same channel ECS, they demonstrated that the new sets of basis functions enable a much more compact representation of both branches of solutions, and, notably, all three velocity components converge at roughly the same rate. Subsequent analysis attributed the improved efficacy of the alternative decomposition to the isolation of the wall-normal velocity response into the Orr-Sommerfeld modes, such that the Squire wall-normal vorticity is free to interact with that generated by the Orr-Sommerfeld modes (Rosenberg, 2018).

1.4 Exact coherent states

Exact coherent states (ECS) is a term coined by Waleffe (1998) for special solutions of the full nonlinear NSE. Most known examples of ECS are either equilibria (of which the laminar state is a trivial example) and periodic orbits, that is, flows which are time-periodic, such as the classical von Kàrmàn vortex shedding in the wake of a circular cylinder. The first three-dimensional ECS for one of the canonical shear flow geometries was the Couette flow equilibrium reported by Nagata (1990), obtained by continuing the Taylor vortex flow solution for flow between concentric rotating cylinders to the case of zero average rotation rate. Since then, numerous other equilibria have been discovered for Couette flow (Gibson et al., 2008; Nagata,

1997; Itano and Generalis, 2009; Ahmed and Sharma, 2020) and other canonical shear flow geometries (Waleffe, 1998; Waleffe, 2001; Faisst and Eckhardt, 2003; Pringle and Kerswell, 2007; Park and Graham, 2015), as have periodic orbits (Clever and Busse, 1997; Kawahara and Kida, 2001; Viswanath, 2007b; Duguet et al., 2008; Willis et al., 2016).

In the dynamical systems interpretation of turbulence, a turbulent flow, represented by a chaotic trajectory through the (nominally infinite-dimensional) state space of all possible velocity fields satisfying the NSE, may spend a significant amount of time in the vicinity of various ECS. This has led researchers to hypothesize that the coherent structures observed in turbulence are the signature of a nearby ECS, and therefore that ECS form the state space “skeleton” of turbulence. Indeed, known solutions reproduce features such as the near-wall regeneration cycle (Kawahara and Kida, 2001). This perspective is enticing because it situates ECS as a reduced-order model of sorts, where individual solutions can be thought of analogously to (nonlinear) basis functions, from which turbulence can be reconstructed. While there is presently no means to practically implement such a model, it is nonetheless a valuable conceptual tool.

The most common numerical method for finding an ECS is Newton iteration. While this method converges rapidly once in the vicinity of a solution, convergence depends on a sufficiently good initial guess. Numerous techniques for generating initial guesses have been employed in the literature, most of which are reviewed in Kawahara et al. (2012). In a bisection method, two guesses are generated. If one leads to turbulence, and the other decays to laminar, another is chosen between the first two, and this process is repeated until the flow neither relaminarizes or becomes fully turbulent for a sufficiently long time. Using homotopy, an extra parameter is introduced (e.g., rotation rate in the original Nagata solution), and a solution is obtained for the original system by continuing solutions to the case of the parameter value being zero. Filtered snapshots from a turbulent field can also be used as initial guesses. This often entails the use of recurrence plots, in which a time series is closely examined for quasi-periodic behavior. Recently, Page and Kerswell (2020) applied dynamic mode decomposition (DMD) (Schmid, 2010) to turbulent time series to generate robust initial guesses for nearby periodic orbits. Another approach proposed recently by Ahmed and Sharma (2020) uses resolvent analysis to generate low-dimensional projections of known ECS, which resulted in the discovery of numerous new families of equilibria in Couette flow. Finally, Rosenberg

and McKeon (2019a) demonstrated that an iterative resolvent-based method can generate converged ECS starting from the laminar state.

ECS often appear in saddle-node bifurcations at a finite Re , which yield two branches. One is typically closer to the laminar state and is thus referred to as the lower branch (LB). The other is called the upper branch (UB), and is usually more “turbulent-like”. Because LB solutions are more like the laminar state, they are typically easier to compute. Moreover, some LB solutions exhibit the same Re scaling as the finite amplitude vortex-wave interaction solutions for asymptotically large Re (Hall and Sherwin, 2010). Computing UB can be more difficult. Typically, one starts from a known solution at a given Re , often close to the bifurcation point and then continues the solution branch to larger Re , using the previous converged state as the initial guess for the next search. However, this can be a computationally expensive procedure, particularly at higher Re where smaller steps are required, and convergence requires more iterations at each step. It would therefore be valuable to have a method that can generate good initial guesses for UB solutions that do not necessitate costly continuations.

1.5 Objectives and organization of the thesis

The present thesis concerns the application of reduced-order modeling techniques to particular problems in wall-bounded turbulent flows. These are presented as three relatively self-contained case studies pertaining to the broad themes of linear mechanisms, nonlinear interactions, and data-driven methods. While specific objectives are given in the relevant chapters, the overarching goals are to (1) gain deeper physical insight into the flow through reduced-order modeling, and (2) augment equations-based techniques with data to expand their utility.

The remainder of the thesis is organized as follows: First, Chapter 2 introduces resolvent analysis for a general nonlinear system. Then, Chapter 3 details the application of resolvent analysis to viscoelastic fluids in an attempt to elucidate the linear mechanisms underlying the origin of the dominant structures observed in EIT. In Chapter 4 it is demonstrated that an efficient, low-order representation of second-order statistics in Newtonian turbulent channel flow can be constructed using an alternative decomposition of the resolvent operator (Rosenberg and McKeon, 2019b), and this representation is used to probe nonlinear interactions within the resolvent framework. Next, Chapter 5 explores the feasibility of using neural networks to generate good initial guesses of upper-branch ECS. Finally, concluding

remarks and possible directions for future work are discussed in Chapter 6.

Chapter 2

PRELIMINARIES OF RESOLVENT ANALYSIS

The purpose of this chapter is to introduce the basics of resolvent analysis in a general setting. Details relevant to the formulation for viscoelastic fluids and nonlinear interactions are given in Chapters 3 and 4, respectively.

2.1 The resolvent operator

Here we introduce resolvent analysis in the context of a generic nonlinear system:

$$\frac{d\tilde{\mathbf{q}}}{dt} = \mathbf{F}(\tilde{\mathbf{q}}), \quad (2.1)$$

where $\tilde{\mathbf{q}}(t)$ is the state of the system at time t . Presently, the only assumption we make is that Equation (2.1) is statistically stationary, such that a well-defined mean $\mathbf{Q} := \langle \tilde{\mathbf{q}} \rangle$, where $\langle \cdot \rangle$ denotes the averaging operation, exists. In this case, we can decompose the state as $\tilde{\mathbf{q}} = \mathbf{Q} + \mathbf{q}$, where $\mathbf{q} := \tilde{\mathbf{q}} - \mathbf{Q}$ are the fluctuations about the mean. Substituting into Equation (2.1) and subtracting mean quantities yields an equation for the fluctuations:

$$\frac{d\mathbf{q}}{dt} = \mathcal{L}_Q \mathbf{q} + \mathbf{f}(\mathbf{q}, \mathbf{Q}), \quad (2.2)$$

where $\mathcal{L}_Q := \partial \mathbf{F} / \partial \tilde{\mathbf{q}}|_Q$ represents the linearization of Equation (2.1) about the mean \mathbf{Q} , and $\mathbf{f} := \tilde{\mathbf{f}} - \langle \tilde{\mathbf{f}} \rangle$ represents the fluctuations of all terms nonlinear in \mathbf{q} ; as shown in Equation (2.2), \mathbf{f} will also depend on \mathbf{Q} in general. Owing to the stationarity of the system, we express the state and nonlinear terms via their Fourier coefficients, defined as¹

$$\mathbf{q} = \int_{-\infty}^{\infty} \hat{\mathbf{q}} e^{-i\omega t} d\omega, \quad (2.3)$$

$$\mathbf{f} = \int_{-\infty}^{\infty} \hat{\mathbf{f}} e^{-i\omega t} d\omega. \quad (2.4)$$

Substitution into Equation (2.2) gives

$$(-i\omega I - \mathcal{L}_Q) \hat{\mathbf{q}} = \hat{\mathbf{f}}, \quad (2.5)$$

¹The sign of ω in the temporal Fourier Transform is chosen to conform with the convention in hydrodynamic stability literature that positive frequencies and spatial wavenumbers correspond to downstream propagating waves.

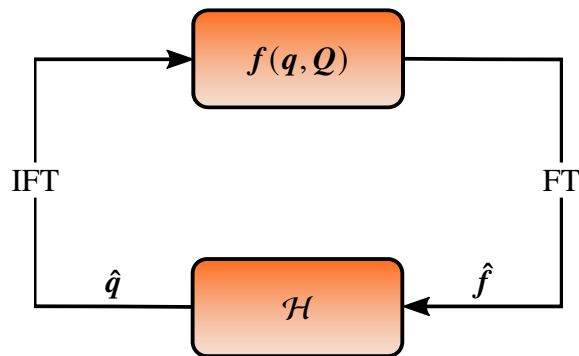


Figure 2.1: Schematic of resolvent analysis. “IFT” and “FT” denote the inverse and forward Fourier transforms, respectively.

where I is the identity operator. Provided $-i\omega$ does not belong to the spectrum of \mathcal{L}_Q , the operator on the left-hand side of Equation (2.5) is invertible, and the Fourier coefficients of the fluctuations can be expressed as

$$\hat{q} = (-i\omega I - \mathcal{L}_Q)^{-1} \hat{f} = \mathcal{H} \hat{f}, \quad (2.6)$$

where $\mathcal{H} := (-i\omega I - \mathcal{L}_Q)^{-1}$ is called the resolvent of \mathcal{L}_Q . We emphasize that Equation (2.6) is an exact representation of the full nonlinear system in Equation (2.1); the only assumption that has been made is one of statistical stationarity. In this formulation, the nonlinear terms \hat{f} are re-interpreted as endogenous forcing that produce the response of the system \hat{q} (McKeon and Sharma, 2010). This is illustrated schematically in the block diagram shown in Figure 2.1, after McKeon et al. (2013). The bottom half of the loop is the pictorial representation of Equation (2.6): the forcing \hat{f} is acted upon by the linear dynamics, represented by \mathcal{H} , to produce the system response \hat{q} . The top half emphasizes the fact that the forcing is produced by the nonlinearity of the system.

2.2 Decomposition of the resolvent and low-order approximation

In some cases, \mathcal{H} may act as a directional amplifier (McKeon and Sharma, 2010). That is, it may preferentially amplify particular forcing inputs. In such cases, an efficient low-order representation of the system can be obtained via a singular value (or Schmidt) decomposition of the resolvent operator:

$$\mathcal{H} = \sum_{j=1}^{\infty} \psi_j \sigma_j (\cdot, \phi_j)_f, \quad (2.7)$$

where ψ_j and ϕ_j , are left and right singular vectors, respectively. They are ordered by the singular values $\sigma_j \geq \sigma_{j+1} > 0$, which quantify the input-output gain. $(\cdot, \cdot)_f$

denotes the inner product defined on the input space, to which \hat{f} belongs. We note that since \mathcal{H} is parameterized by ω , the singular vectors and values are as well.

The left and right singular vectors comprise orthonormal bases for the input (forcing) and output (response) spaces, respectively:

$$(\phi_j, \phi_k)_f = (\psi_j, \psi_k)_q = \delta_{jk}, \quad (2.8)$$

where δ_{jk} is the Kronecker delta. Consequently, the ϕ_j are referred to as forcing modes, and the ψ_j as response modes. \hat{f} can be expanded as

$$\hat{f} = \sum_{j=1}^{\infty} \chi_j \phi_j, \quad (2.9)$$

where $\chi_j = (\hat{f}, \phi_j)_f \in \mathbb{C}$ are referred to as the resolvent weights, and, using Equations (2.6) and (2.7),

$$\hat{q} = \sum_{j=1}^{\infty} \sigma_j \chi_j \psi_j. \quad (2.10)$$

\hat{q} can be approximated using the first N modes:

$$\hat{q}_N = \sum_{j=1}^N \sigma_j \chi_j \psi_j. \quad (2.11)$$

Hereafter, \hat{q}_N is referred to as the rank- N approximation. Ideally, this approximation is good for relatively small N . That is, the error introduced by truncation,

$$\|\hat{q}_N - \hat{q}\|_q^2 = \sum_{j=N+1}^{\infty} \sigma_j^2 |\chi_j|^2, \quad (2.12)$$

is small. However, as discussed in Section 1.3, the forcing is rarely known, making such an error estimate impossible to compute *a priori*.

In the special case of (unit amplitude) white noise forcing, $\chi_j = 1 \forall j$, and the truncation error becomes

$$\|\hat{q}_N - \hat{q}\|_q^2 = \sum_{j=N+1}^{\infty} \sigma_j^2. \quad (2.13)$$

Thus if $\sigma_N \gg \sigma_{N+1}$, the approximation \hat{q}_N is expected to be good, and the resolvent operator is said to be effectively low rank (McKeon and Sharma, 2010). A special case worthy of particular attention is the case $N = 1$, i.e., the rank-1 approximation, which states that

$$\hat{q} \propto \psi_1. \quad (2.14)$$

This implies that the dynamics of the system for a particular value of ω are dominated by a single mechanism that is strongly linearly amplified by the resolvent operator, and that the resulting features are captured by the leading resolvent mode. It has been demonstrated that the rank-1 approximation qualitatively reproduces structures observed in wall-bounded turbulence (Sharma and McKeon, 2013), and that the region of parameter space where the resolvent operator is effectively rank-1 has significant overlap with the region where turbulent fluctuations are highly energetic (Moarref et al., 2013a). In Chapter 3, the rank-1 approximation is employed in an analysis of the predominant structures in elastoinertial turbulence.

However, the assumption of white noise forcing is not valid for many systems, including turbulent flows (Zare et al., 2017; Towne et al., 2018). Therefore, quantitatively accurate approximations require calculation or estimation of the resolvent weights. This is the subject of Chapter 4.

Chapter 3

LINEAR ANALYSES OF ELASTOINERTIAL TURBULENCE IN CHANNELS

Portions of this chapter have been previously published in¹:

McMullen, R. M., Shekar, A., Graham, M. D., and McKeon, B. J. (2018). “Weissenberg number dependence of linear mechanisms in polymer drag-reduced turbulent channel flow”. *12th International ERCOFTAC Symposium on Engineering Turbulence Modelling and Measurements*.

Shekar*, A., McMullen*, R. M., Wang, S.-N., McKeon, B. J., and Graham, M. D. (2019). “Critical-Layer Structures and Mechanisms in Elastoinertial Turbulence”. *Phys. Rev. Lett.* 122 (12). DOI: 10.1103/PhysRevLett.122.124503, p. 124503.

*Equal contribution.

Shekar, A., McMullen, R. M., McKeon, B. J., and Graham, M. D. (2020). “Self-sustained elastoinertial Tollmien-Schlichting waves”. *Journal of Fluid Mechanics*. To appear.

3.1 Chapter overview

EIT is a puzzling phenomenon that is of great importance for both fundamental and practical reasons. On the one hand, it is a chaotic flow state that is unique to viscoelastic fluids. On the other, there is strong evidence suggesting that EIT is the origin of the maximum drag reduction (MDR) state. Both of these aspects would benefit from a more complete understanding of the mechanisms underlying EIT. Consequently, the goal of the present chapter is to provide some insights into the mechanisms that are responsible for initiating EIT, as well as sustaining it. Both modal and non-modal techniques are employed to highlight the responsible mechanisms and offer an explanation of how they become strongly amplified.

The organization of the chapter is as follows. First, the governing equations for a viscoelastic fluid are presented, and the resolvent formulation is revisited in this context. Next, we demonstrate that the significant structural differences between

¹The DNS presented in this chapter were performed by Ashwin Shekar and Michael D. Graham. Additionally, we are extremely grateful for many discussions with them over the course of a collaboration from which the contents of this chapter stemmed.

low levels of drag reduction and EIT are reflected in the linear dynamics of the flow, as highlighted by componentwise input-output analysis. Further, it is shown that the leading resolvent mode closely resembles the structure of the polymer stress fluctuations that are characteristic of EIT. To gain further insight into the origin of these structures, we next shift our focus to analysis of perturbations to the laminar state, showing that they strongly resemble the viscoelastic extension of Tollmien-Schlichting (TS) waves, which are the most-amplified modes. Finally, analysis of the mode structure shows that critical layer localization is a likely cause of the strong polymer stretching, and these observations are supported by comparison with nonlinear simulations of self-sustaining viscoelastic TS waves.

3.2 Formulation for viscoelastic fluids

First, we introduce the aspects of the resolvent formulation specific to the analysis of viscoelastic fluids.

Continuum modeling of polymers

Given the complexity of long, flexible polymer molecules typical for drag reduction purposes, a coarse-grained representation is desirable in order to make theoretical and computational approaches tractable. The most common one used for complex flows is the bead-spring dumbbell model, in which the polymer molecule is represented by two massless beads connected by a spring, as shown schematically in Figure 3.1. In this model, the molecule's conformation is entirely described by the end-to-end vector \boldsymbol{p} . That is, all internal degrees of freedom are neglected, and only the molecule's orientation and elongation can be described. This may at first seem like an extremely crude approximation. However, such deformations are associated with the slowest relaxation rates and are therefore the first to be excited by the flow, and they also make the largest contribution to the fluid stress (Graham, 2018). Therefore, it may be considered a suitable model to qualitatively reproduce the first-order effects of polymer-flow interactions.

While the bead-spring dumbbell model greatly simplifies the description of the polymers, it is still a microscopic one, and we desire a continuum-level representation that is compatible with the Navier-Stokes equations describing the motion of the fluid. Fortunately, this can be rigorously derived from the kinetic description, starting from a Smoluchowski equation for the probability distribution of the polymers. However, as this is not the focus of the present chapter, we omit the details and instead refer the reader to either Bird et al. (1987) or Graham (2018). Rather than

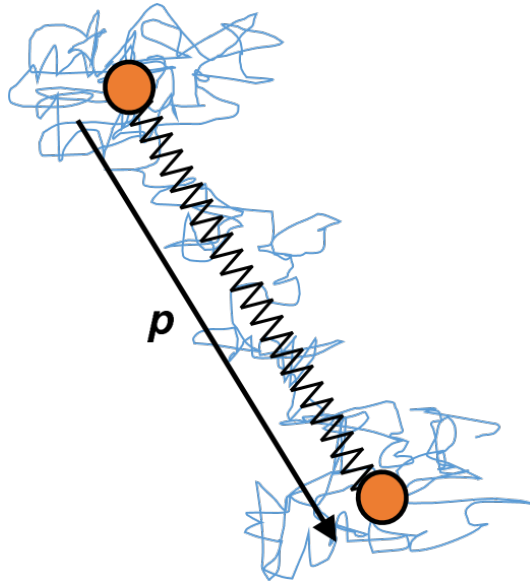


Figure 3.1: Schematic of the bead-spring dumbbell model for a polymer molecule; \mathbf{p} is the end-to-end vector.

solve for the distribution, an adequate level of fidelity can be retained by writing an evolution equation for the conformation tensor

$$\tilde{\mathbf{r}} := \frac{3}{R_0^2} \langle \mathbf{p} \otimes \mathbf{p} \rangle_{\mathbf{p}}, \quad (3.1)$$

which is the second moment of the distribution, here nondimensionalized by the equilibrium mean squared length of the molecule R_0^2 , such that $\tilde{\mathbf{r}} = \mathbf{I}$ at equilibrium, and where

$$\langle f \rangle_{\mathbf{p}}(\mathbf{x}, t) := \int f \psi(\mathbf{x}, \mathbf{p}, t) d\mathbf{p} \quad (3.2)$$

is the average over all conformations and ψ is the conformation probability density. The resulting evolution equation for the conformation tensor is

$$\partial_t \tilde{\mathbf{r}} + (\tilde{\mathbf{u}} \cdot \nabla) \tilde{\mathbf{r}} - \tilde{\mathbf{r}} \cdot \nabla \tilde{\mathbf{u}} - (\tilde{\mathbf{r}} \cdot \nabla \tilde{\mathbf{u}})^T = -\frac{1}{G\lambda} \tilde{\boldsymbol{\tau}} + D \nabla^2 \tilde{\mathbf{r}}. \quad (3.3)$$

The left-hand side of Equation (3.3) is the upper-convected derivative, which is the rate of change of a second-order tensor in a material frame. The first term on the right-hand side is the polymer stress

$$\frac{1}{G\lambda} \tilde{\boldsymbol{\tau}} = -\frac{1}{\lambda} \mathbf{I} + \frac{n}{G\lambda} \langle \mathbf{p} \otimes \mathbf{F} \rangle, \quad (3.4)$$

where $G = nk_B T$ is the shear modulus, n is the number density of the molecules, k_B is the Boltzmann constant, T is the absolute temperature of the solution, and λ

is the stress relaxation time (Graham, 2018). \mathbf{F} is the spring connector force. Here, we use Warner's force law for a finitely extensible nonlinearly elastic (FENE) spring (Bird et al., 1987; Beris and Edwards, 1994; Graham, 2018), which is given by

$$\mathbf{F}(\mathbf{p}) = H \frac{\mathbf{p}}{1 - L^{-2} \mathbf{p} \cdot \mathbf{p}}, \quad (3.5)$$

where L is the maximum length of the spring and $H = 3k_B T / R_0^2$ is the spring constant. Substitution of Equation (3.5) into Equation (3.4) gives an expression that cannot be expressed solely in terms of the conformation tensor. Therefore, an approximation, known as the Peterlin closure, is often invoked (Beris and Edwards, 1994; Graham, 2018); this consists of pre-averaging the denominator of Equation (3.5) to give

$$\left\langle \frac{\mathbf{p} \otimes \mathbf{p}}{1 - L^{-2} \mathbf{p} \cdot \mathbf{p}} \right\rangle \approx \left\langle \frac{\mathbf{p} \otimes \mathbf{p}}{1 - L^{-2} \langle \mathbf{p} \cdot \mathbf{p} \rangle} \right\rangle = \frac{R_0^2}{3} P(\tilde{\mathbf{r}}) \tilde{\mathbf{r}}, \quad (3.6)$$

where

$$P(\tilde{\mathbf{r}}) := \frac{1}{1 - \ell^{-2} \text{tr} \tilde{\mathbf{r}}}, \quad (3.7)$$

is the Peterlin function and $\ell^2 = 3L^2 / R_0^2$ is the dimensionless maximum extensibility. The FENE model with Peterlin closure is referred to as the FENE-P model.

The second term on the right-hand side of Equation (3.3) represents diffusion of the polymer molecules with diffusivity D . Typically, this diffusivity is very small, and this term is usually neglected, as it will be herein. However, this has some mathematical and numerical consequences, which will be discussed later.

To bring the conformation tensor equation Equation (3.3) into dimensionless form, we introduce the velocity and length scales U and h respectively, giving

$$\partial_t \tilde{\mathbf{r}} + (\tilde{\mathbf{u}} \cdot \nabla) \tilde{\mathbf{r}} - \tilde{\mathbf{r}} \cdot \nabla \tilde{\mathbf{u}} - (\tilde{\mathbf{r}} \cdot \nabla \tilde{\mathbf{u}})^T = -\tilde{\boldsymbol{\tau}}, \quad (3.8)$$

$$\tilde{\boldsymbol{\tau}} = \frac{1}{Wi} (P(\tilde{\mathbf{r}}) - \mathbf{I}), \quad (3.9)$$

where $Wi = \lambda U / h$ is the Weissenberg number; it is the ratio of the relaxation time of the polymers to the flow time scale h / U . If $Wi \ll 1$, then the polymers relax too quickly to be significantly stretched by the flow, whereas if $Wi \gg 1$, significant stretching can be expected, and the flow will be strongly viscoelastic.

We conclude this section by stating the assumptions and limitations of the FENE-P model leading to Equation (3.8), apart from those related to the bead-spring dumbbell model already discussed. First is that the number density n , i.e., the

concentration of the polymers, is constant. Therefore, the FENE-P model cannot account for polymer agglomeration. Second, hydrodynamic interactions between polymer molecules are neglected. That is, each molecule behaves as it would in an infinitely dilute solution.

Governing equations

The full set of governing equations for an incompressible FENE-P fluid are

$$\partial_t \tilde{\mathbf{u}} + (\tilde{\mathbf{u}} \cdot \nabla) \tilde{\mathbf{u}} = -\nabla \tilde{p} + \frac{\beta}{Re} \nabla^2 \tilde{\mathbf{u}} + \frac{1-\beta}{Re} (\nabla \cdot \tilde{\boldsymbol{\tau}}), \quad (3.10)$$

$$\nabla \cdot \tilde{\mathbf{u}} = 0, \quad (3.11)$$

$$\partial_t \tilde{\boldsymbol{r}} + (\tilde{\mathbf{u}} \cdot \nabla) \tilde{\boldsymbol{r}} = \tilde{\boldsymbol{r}} \cdot \nabla \tilde{\mathbf{u}} + (\tilde{\boldsymbol{r}} \cdot \nabla \tilde{\mathbf{u}})^T - \tilde{\boldsymbol{\tau}}, \quad (3.12)$$

$$\tilde{\boldsymbol{\tau}} = \frac{1}{Wi} (P(\tilde{\boldsymbol{r}}) - \mathbf{I}), \quad (3.13)$$

where $\beta = \mu_s / (\mu_s + \mu_p)$ is the ratio of the solvent viscosity to the total viscosity, and $Re = \rho U h / (\mu_s + \mu_p)$ is the Reynolds number, and ρ is the fluid density. For all of the results presented here, we fix $\beta = 0.97$ and $\ell = 80$ because these values are representative of a dilute polymer solution used for drag reduction.

Perturbation equations

We now consider additive perturbations to all flow variables: $\tilde{\mathbf{u}} = \mathbf{U} + \mathbf{u}$, $\tilde{p} = P + p$, $\tilde{\boldsymbol{r}} = \mathbf{R} + \mathbf{r}$, where \mathbf{U} , P , \mathbf{R} are either base or mean states. The perturbation equations are obtained by substituting the decompositions into Equations (3.10)–(3.12):

$$\partial_t \mathbf{u} + (\mathbf{U} \cdot \nabla) \mathbf{u} + (\mathbf{u} \cdot \nabla) \mathbf{U} = -\nabla p + \frac{\beta}{Re} \nabla^2 \mathbf{u} + \frac{1-\beta}{Re} (\nabla \cdot \boldsymbol{\tau}), \quad (3.14)$$

$$\nabla \cdot \mathbf{u} = 0, \quad (3.15)$$

$$\begin{aligned} \partial_t \mathbf{r} + (\mathbf{U} \cdot \nabla) \mathbf{r} + (\mathbf{u} \cdot \nabla) \mathbf{R} &= \mathbf{R} \cdot \nabla \mathbf{u} + \mathbf{r} \cdot \nabla \mathbf{U} \\ &+ (\mathbf{R} \cdot \nabla \mathbf{u})^T + (\mathbf{r} \cdot \nabla \mathbf{U})^T - \boldsymbol{\tau}. \end{aligned} \quad (3.16)$$

Because of the form of the Peterlin function, substitution of the decomposition into Equation (3.7) yields the series

$$P(\mathbf{R} + \mathbf{r}) = \sum_{k=0}^{\infty} \frac{\bar{P}^{k+1}}{\ell^{2k}} (\text{tr } \mathbf{r})^k, \quad (3.17)$$

where $\bar{P} = P(\mathbf{R})$. Thus the polymer stress is decomposed as $\tilde{\boldsymbol{\tau}} = \mathbf{T} + \boldsymbol{\tau}$, where

$$\mathbf{T} = \frac{1}{Wi} (\bar{P} \mathbf{R} - \mathbf{I}) \quad (3.18)$$

is the base state stress, and

$$\boldsymbol{\tau} = \frac{\bar{P}}{Wi} \left(\boldsymbol{r} + \frac{\bar{P}}{\ell^2} (\text{tr } \boldsymbol{r}) \boldsymbol{R} + \dots \right) \quad (3.19)$$

is the stress perturbation appearing in Equations (3.14) and (3.16). The terms that are written out explicitly in Equation (3.19) are those that would be retained when considering linear perturbations, and higher-order terms are masked by the ellipses.

Here, it is appropriate to briefly comment on the mathematical nature of the conformation tensor. Apparent from Equation (3.1) is that $\tilde{\boldsymbol{r}}$ is a real, symmetric tensor. Furthermore, since each of its diagonal components $r_{ii} = \langle p_i^2 \rangle_p$, $i = 1, 2, 3$, physically represents a squared length and is thus always positive, all of the conformation tensor eigenvalues $\rho_i > 0$, implying that the conformation tensor is positive-definite. This means that, unlike the velocity field \boldsymbol{u} , the proper mathematical setting for the analysis of the conformation tensor is non-Euclidean in nature (Doering et al., 2006; Balci et al., 2011; Hameduddin et al., 2018). For this reason, Hameduddin et al. (2018) proposed an alternative geometric decomposition of the conformation tensor, arguing that a Reynolds decomposition inhibits physical interpretation since the fluctuation tensor \boldsymbol{r} is necessarily not positive-definite and does not handle extensions and compressions on equal footing. Furthermore, Hameduddin and Zaki (2019) show that the arithmetic mean of the conformation tensor is not necessarily representative of probable individual realizations.

However, within the resolvent framework, the fluctuations \boldsymbol{r} can still be made mathematically consistent by, for example, imposing the additional constraint that the computed weights yield a positive-definite total tensor $\tilde{\boldsymbol{r}}$. Additionally, the mean as defined here still has meaning as the $(k_x, k_z, \omega) = \mathbf{0}$ Fourier component. Furthermore, the primary results of the resolvent analysis presented in this chapter are compared to DNS (which do obey the positive-definite constraint) and are found to be in good qualitative agreement, thereby justifying our choice of formulation. Nonetheless, an interesting avenue for future work would be to see if the geometric decomposition of Hameduddin et al. (2018) can be incorporated within the resolvent analysis framework, as well as to see how this would modify the results.

The viscoelastic resolvent operator

The state vector for resolvent analysis of the viscoelastic fluid is comprised of the three velocity fluctuation components, the pressure fluctuations, and the six

independent components of the conformation tensor fluctuations:

$$\mathbf{q} = \left(u \quad v \quad w \quad p \quad r_{xx} \quad r_{yy} \quad r_{zz} \quad r_{xy} \quad r_{xz} \quad r_{yz} \right)^T. \quad (3.20)$$

Note that while there are ten equations, there are only nine nonzero forcing components since the continuity equation is linear. The forcing components for the momentum equations are denoted with a single subscript, f_a , $a \in \{x, y, z\}$, and the forcing components of the conformation tensor equations are denoted with a double subscript, f_{ab} , $a, b \in \{x, y, z\}$.

Fourier transforming in x , z , and t , the resolvent equation Equation (2.6) takes the form

$$\hat{\mathbf{q}} = \left[-i\omega\mathcal{M} - \begin{pmatrix} \mathcal{L}_{11} & \mathcal{L}_{12} \\ \mathcal{L}_{21} & \mathcal{L}_{22} \end{pmatrix} \right]^{-1} \mathcal{M}\hat{\mathbf{f}}, \quad (3.21)$$

where $\mathcal{M} := \text{diag}(I_{3 \times 3}, 0, I_{6 \times 6})$, \mathcal{L}_{11} is the linear Navier-Stokes operator, \mathcal{L}_{22} represents advection and stretching of the polymers by the base flow, \mathcal{L}_{12} represents the (linear contribution of) polymer stress fluctuations in the momentum equations, and \mathcal{L}_{21} represents the effects of the velocity fluctuations on the polymer field. Detailed definitions of these operators are given in Appendix A.2.

Choice of inner product

As discussed in Section 2.1, a choice of inner product must be made when computing the resolvent modes. For viscoelastic fluids, this choice is not as obvious as for incompressible Newtonian fluids. This is because, in addition to kinetic energy, the fluid can store elastic energy through polymer stretching. A measure of perturbation magnitude should thus account for this. Unfortunately, the most straightforward definition of the elastic potential energy does not yield a quadratic form amenable to defining an inner product and associated norm (Doering et al., 2006). Indeed, integrating Warner's force law Equation (3.5) using the Peterlin closure Equation (3.6), one obtains for the elastic energy density in a FENE-P fluid (Beris and Edwards, 1994),

$$\begin{aligned} e_p &= \left\langle \int \mathbf{F}(\mathbf{p}) \cdot d\mathbf{p} \right\rangle_p \\ &= \int HP(\tilde{\mathbf{r}}) \langle \mathbf{p} \cdot d\mathbf{p} \rangle_p \\ &= \frac{k_B T \ell^2}{2} \log P(\tilde{\mathbf{r}}). \end{aligned} \quad (3.22)$$

Neither is this true for the simpler Oldroyd-B model ($\ell \rightarrow \infty$), for which $e_p \sim \text{tr } \tilde{\mathbf{r}}$. In this case, factorizing the conformation tensor as $\tilde{\mathbf{r}} = \tilde{\mathbf{b}}^T \tilde{\mathbf{b}}$, where $\tilde{\mathbf{b}}$ is the symmetric square root (SSR) tensor, allows the elastic energy density to be expressed in terms of the standard Frobenius norm: $e_p \sim \|\tilde{\mathbf{b}}\|_F^2$ (Balci et al., 2011; Wang et al., 2014). However, this formulation poses difficulties for implementation within the resolvent framework, as relating the fluctuations of $\tilde{\mathbf{b}}$ to \mathbf{r} is not straightforward. Moreover, the vast majority of the extant literature is formulated in terms of the conformation tensor, making comparison and interpretation of results difficult. For these reasons, the SSR formulation is not adopted here.

In the absence of a well-defined physically-motivated measure of the conformation tensor perturbation magnitude, some of the previous nonmodal stability work for viscoelastic fluids focuses on amplification of velocity fluctuations (Hoda et al., 2008; Hoda et al., 2009; Zhang et al., 2013), the reasoning being that transition would be accompanied by large velocity fluctuations. However, this potentially overlooks the scenario in which amplification of conformation tensor fluctuations, and hence polymer stress fluctuations, become large enough to trigger nonlinear effects that then drive nonlinear velocity fluctuations. Other previous work has demonstrated that polymer stress fluctuations for streamwise-constant disturbances in flows with zero or low levels of inertia can be highly amplified (Jovanović and Kumar, 2010; Jovanović and Kumar, 2011; Lieu et al., 2013), though the need for an appropriate measure of the conformation tensor was circumvented by focusing on individual components of the stress.

In the present analysis, we adopt one that is mathematically consistent with the underlying geometry of positive-definite tensors. For linear perturbations $\mathbf{r}_1, \mathbf{r}_2$ to the base state \mathbf{R} , Hameduddin et al. (2019) proposed using

$$[\mathbf{r}_1, \mathbf{r}_2]_{\mathbf{R}} := \text{tr } \mathbf{R}^{-1} \mathbf{r}_2 \mathbf{R}^{-1} \mathbf{r}_1, \quad (3.23)$$

which is the scalar product on the tangent space of the manifold of positive-definite tensors at the point \mathbf{R} . We refer to this as the geometric inner product. Further details are provided in Appendix A.3. Though not included here, additional calculations were performed using the Frobenius norm as a measure of the conformation tensor perturbation magnitude. It was found that while there are quantitative differences, e.g., in the singular values, the results are qualitatively similar to those using Equation (3.23) and do not change the conclusions of this chapter. For the total perturbation magnitude, we use the sum of the kinetic energy density and

Equation (3.23). The norm is thus defined as

$$\|\hat{q}\|^2 := \int_{-1}^1 \left(\hat{u}^* \hat{u} + \text{tr} \mathbf{R}^{-1} \hat{\mathbf{r}}^* \mathbf{R}^{-1} \hat{\mathbf{r}} \right) dy. \quad (3.24)$$

As noted, Equation (3.23) applies only to linear perturbations to a *base state*. An analysis of such perturbations to the laminar solution (c.f. Appendix A.1) is the focus of Section 3.4. For resolvent analysis, i.e., for finite-amplitude fluctuations about a *mean* conformation tensor, the subject of Section 3.3, we instead analyze individual components of the conformation tensor, which are measured using the standard L^2 norm (Lieu et al., 2013).

Numerical considerations

In the absence of stress diffusivity in the conformation tensor equation Equation (3.3), the associated linear operator \mathcal{L} has a continuous spectrum. For the Oldroyd-B model, the continuous spectrum is comprised of two strips in the lower half of the complex c plane, one with imaginary part $-1/k_x Wi$, and the other with $-1/(1-\beta)k_x Wi$ (Sureshkumar and Beris, 1995b). The continuous spectrum therefore moves closer to the real axis with increasing Wi or k_x . An analytical expression for the continuous spectrum of the FENE-P model is not available but has a similar shape to the Oldroyd-B one. An example is shown in Figure 3.9(a); note that the numerical approximation of the continuous spectrum is actually comprised of a set of discrete eigenvalues, and that it only appears to be continuous due to limitations in plotting precision.

The eigenfunctions associated with the continuous spectrum are highly singular. Previous work has identified the existence of both distribution-valued (Kupferman, 2005) and non-integrable solutions (Graham, 1998). Consequently, these functions cannot be accurately resolved numerically. Furthermore, discretization results in “ballooning” of the continuous spectrum, possibly resulting in spurious unstable eigenvalues. A numerical scheme in which the resolvent operator is first recast as a two-point boundary value problem and then converted to a system of integral equations and solved numerically with Chebfun (Driscoll et al., 2014) helps alleviate some of the numerical instability issues (Lieu and Jovanović, 2013). Inclusion of stress diffusivity has also been considered to circumvent these issues (Sureshkumar and Beris, 1995a). However, resolution of the length scale $\sqrt{D\lambda}$ associated with a realistic value of the stress diffusivity D would require an enormous number of grid points and is therefore not practical, especially for large Wi .

For the range of k_x and Wi considered in this chapter, discretization using a standard Chebyshev pseudospectral method (Weideman and Reddy, 2000) was found to be feasible, albeit with a relatively large number of Chebyshev polynomials. From about $N_y = 150$ to 250 are required for satisfactory convergence of the singular values, while convergence of (discrete) eigenvalues requires as many as $N_y = 400$.

3.3 Weissenberg number dependence of linear mechanisms in viscoelastic channel flow

In this section, we show that the structural contrasts between low drag reduction and EIT are reflected in the linear dynamics of the flow, and that predictions from resolvent analysis are in good qualitative agreement with the DNS. We focus on two cases of viscoelastic channel flow at transitional $Re = 1500$: $Wi = 7$ and $Wi = 20$, representative of low drag reduction and EIT, respectively.

Direct numerical simulations

In order to frame the results from the resolvent analysis, we begin by discussing some of the features observed in direct numerical simulations. The details of the numerics are provided in Shekar et al. (2019).

Figure 3.2 shows the mean velocity profiles for both cases, along with that for Newtonian flow at the same Re for comparison; also shown are the Kármán log law for Newtonian turbulence and the log law proposed by Virk for MDR (Virk, 1975). The $Wi = 7$ profile lies slightly above the Newtonian one, indicating a low level of drag reduction, whereas the $Wi = 20$ profile falls nearly on the Virk asymptote.

In addition to the change in statistical quantities, the flow structures at low levels of drag reduction and EIT are drastically different (Samanta et al., 2013). To illustrate this, snapshots of vortical structures, identified with isocontours of the Q -criterion (Hunt et al., 1988), and contours of polymer stretch $\text{tr } \tilde{\mathbf{r}}$ for $Wi = 7$ and $Wi = 20$ are shown in Figure 3.3(a) and Figure 3.3(b), respectively. For $Wi = 7$, the flow is populated with quasi-streamwise vortices that are familiar from Newtonian wall-bounded turbulence. The polymers are stretched and advected upward between the vortices, forming the “plumes” shown in the plane at $x = 0$ in Figure 3.3(a). In stark contrast, the flow at $Wi = 20$ exhibits weak, spanwise-oriented vortices and quasi-two-dimensional, highly-inclined sheets of polymer stretch that are localized near the wall.

Additionally, the spatial spectra of the wall-normal velocity fluctuations v at the

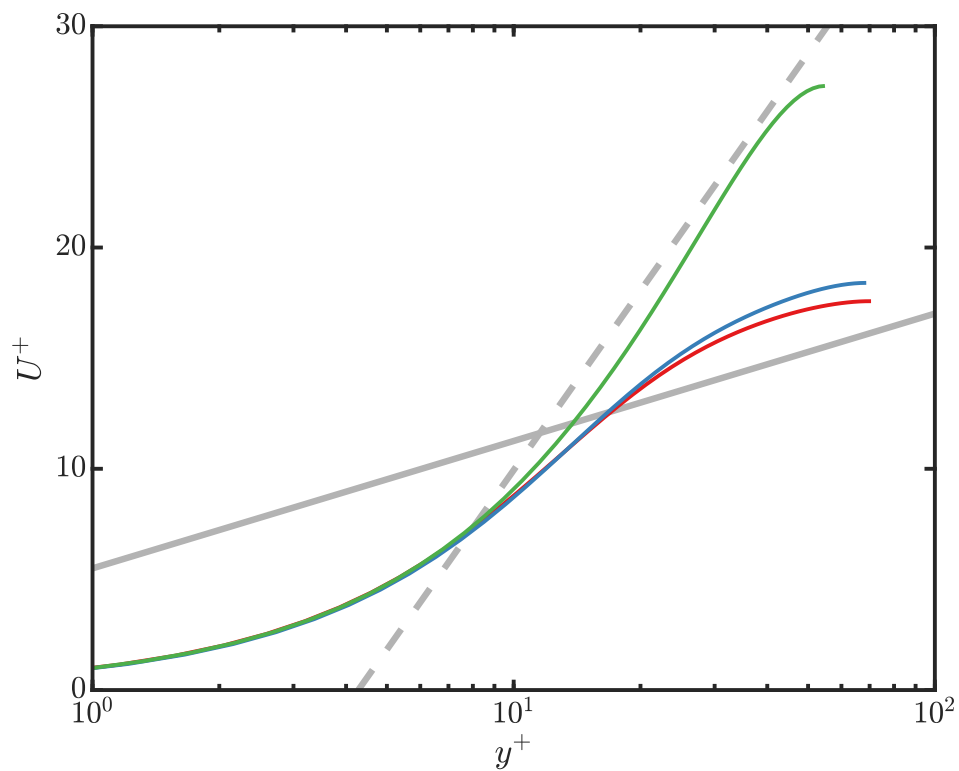


Figure 3.2: Mean velocity profiles in inner units for $Wi = 0$ (red), $Wi = 7$ (blue), and $Wi = 20$ (green). Also shown are the Kármán log law $U^+ = 2.5 \log y^+ + 5.5$ (solid gray) and the Virk asymptote $U^+ = 11.7 \log y^+ - 17.0$ (dashed gray).

channel centerline $y = 0$ are shown as insets in Figure 3.3 in terms of the scaled wavenumbers $k_x L_x / 2\pi$ and $k_z L_z / 2\pi$, where $L_x = 10$ and $L_z = 5$ are the streamwise and spanwise dimensions of the DNS box, respectively. Consistent with the qualitative observations made above, there is a shift from streamwise-oriented structures at $Wi = 7$, represented by spectral content at $k_x L_x / 2\pi = 0$, to spanwise-oriented structures at $Wi = 20$, represented by spectral content at $k_z L_z / 2\pi = 0$.

Componentwise amplification analysis

Next, we demonstrate that some of the most important structural differences between the $Wi = 7$ and $Wi = 20$ DNS cases discussed above, namely the emergence of spanwise-constant structures, are captured by resolvent analysis. Our focus is on the largest amplification over all temporal frequencies ω for a given spatial scale (k_x, k_z) , which is quantified by the H_∞ norm of the resolvent operator (Zhou et al., 1996):

$$\|\mathcal{H}\|_\infty(k_x, k_z) := \sup_{\omega \in \mathbb{R}} \sigma_1(k_x, k_z, \omega). \quad (3.25)$$

Further insight can be gained by considering componentwise amplification (Jovanović and Bamieh, 2005; Schmid, 2007; Lieu et al., 2013), that is, the amplification from a particular forcing component to a particular response component. This can be achieved by appropriately altering the input and output operators \mathcal{B} and \mathcal{C} of the resolvent², as in, e.g., $\mathcal{H}_{x \rightarrow u} := \mathcal{C}_u (-i\omega\mathcal{M} - \mathcal{L})^{-1} \mathcal{B}_x$, which maps the nonlinear streamwise velocity forcing f_x to the streamwise velocity response u . In this case, we choose the underlying norm on the input and output to be the standard $L^2[-1, 1]$ norm. With a total of nine forcing components and ten response components, there are 90 possible input-output operators. Here we focus on only two forcing components and two response components: The response components are u and r_{xx} , since they typically dominate the velocity and conformation tensor fields, respectively. The forcing components are f_x and f_y . With the exception of $k_z \rightarrow 0$, the response to f_z is qualitatively similar to that for f_y , and it has been found that the velocity forcing typically elicits a much larger response than the conformation tensor forcing. Moreover, the observations presented here, particularly the Wi trends, hold qualitatively for the other input-output pairs not shown.

Figure 3.4 shows the H_∞ norm of $\mathcal{H}_{s \rightarrow u}$, with $s = \{x, y\}$ for the wavenumber ranges $k_x \in [10^{-3}, 3]$, $k_z \in [10^{-2}, 10]$. Results for $Wi = 7$ are shown in Figure 3.4(a) and Figure 3.4(b), and those for $Wi = 20$ in Figure 3.4(c) and Figure 3.4(d).

²In Equation (3.21) $\mathcal{B} = \mathcal{M}$ and $\mathcal{C} = I_{10 \times 10}$.

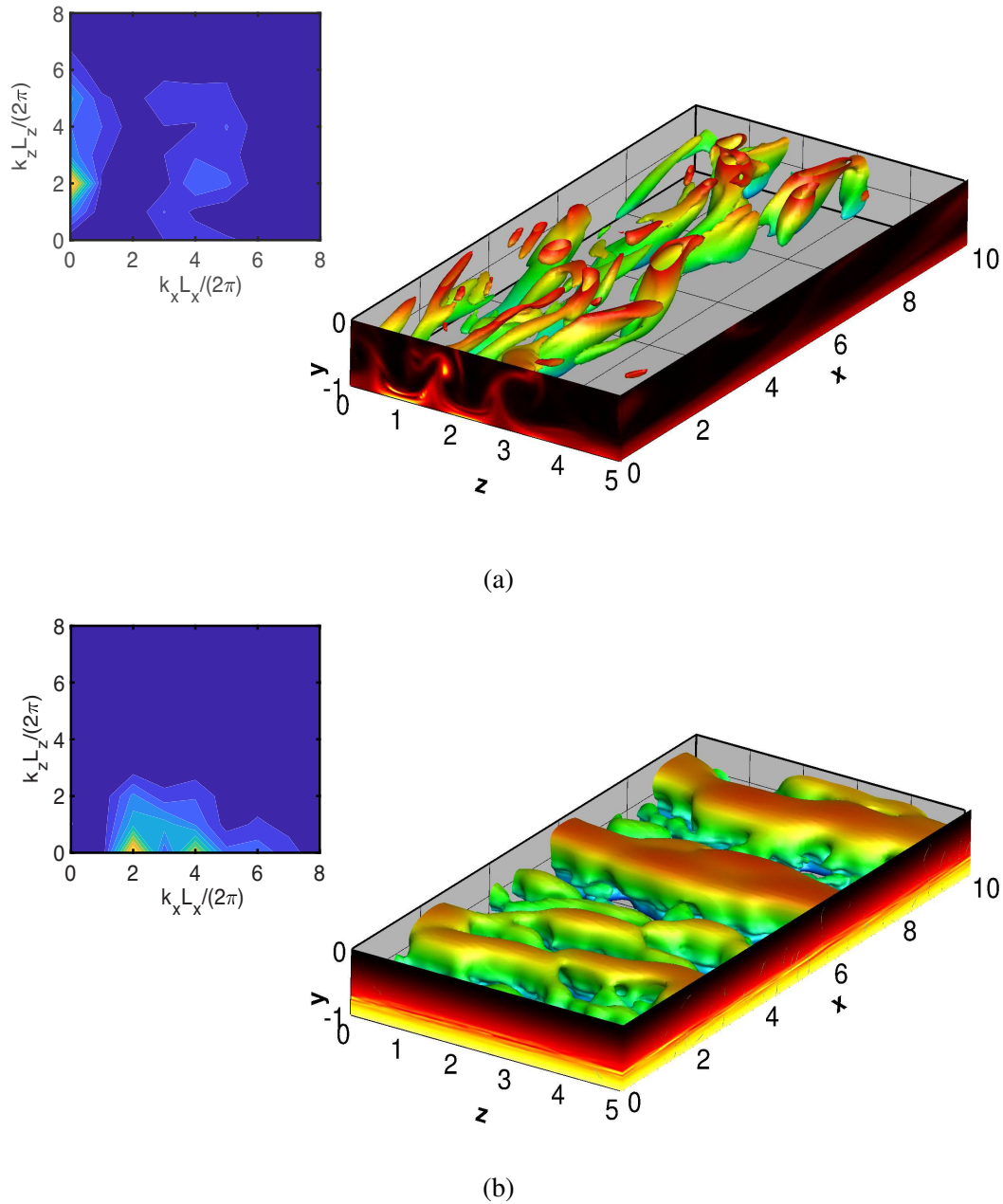


Figure 3.3: (a) Snapshot of flow structures for $Wi = 7$ in the lower half of the domain: Isosurface of vortex strength $Q = 0.075$, color-coded blue to red based on increasing distance from the wall, and polymer stretch $\text{tr } \tilde{\mathbf{r}}$ in the planes $x = 0$ and $z = 5$; lighter contours indicate high levels. Inset is the time averaged spatial spectrum of v at $y = 0$; significant spectral content is indicated by lighter contours. (b) Same as in (a) for $Wi = 20$, but with $Q = 0.00014$.

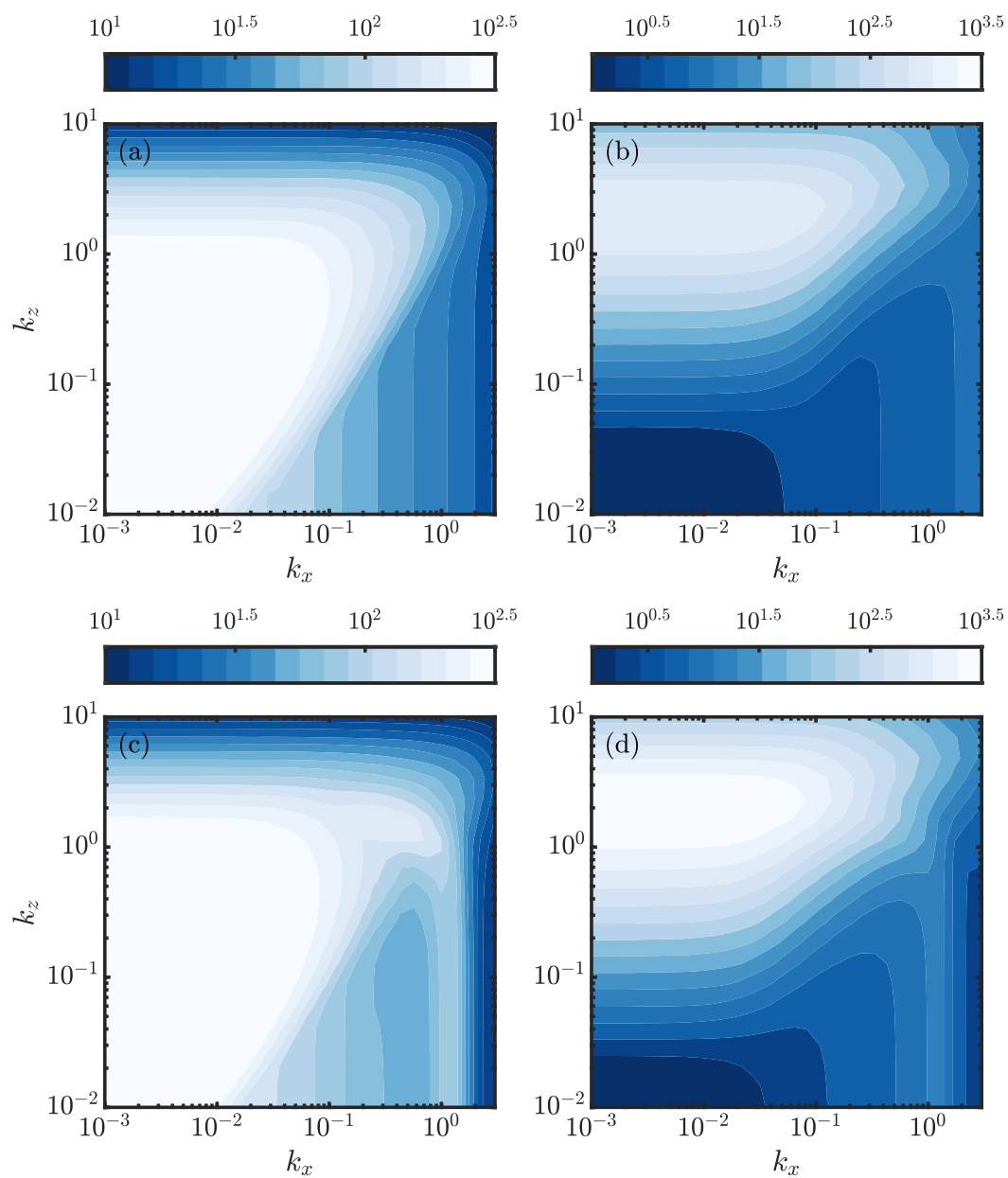


Figure 3.4: H_∞ norms of (a),(c) $\mathcal{H}_{x \rightarrow u}$ and (b),(d) $\mathcal{H}_{y \rightarrow u}$, with (a),(b) $Wi = 7$; (c),(d) $Wi = 20$.

For $Wi = 20$, there is a visible strip for $k_z \rightarrow 0$ and $k_x = O(1)$ that is absent at $Wi = 7$ and is reminiscent of the signature of Tollmien-Schlichting waves (Schmid, 2007). This is perhaps not altogether surprising considering that the mean velocity profile at $Wi = 20$ is almost identical to the laminar parabolic profile. However, for both Wi , streamwise-elongated modes, i.e., $k_x \rightarrow 0$, are the globally most amplified, with the peak for wall-normal forcing (Figure 3.4(b) and Figure 3.4(d)) occurring for $k_z = O(1)$, suggesting that streamwise rolls and streaks are still the optimal linearly amplified velocity structures at EIT. Additionally, the magnitude of the peak amplification does not change appreciably between $Wi = 7$ and $Wi = 20$.

Next, we consider the amplification for the dominant conformation tensor component r_{xx} . Figure 3.5 shows the \mathcal{H}_∞ norm of $\mathcal{H}_{s \rightarrow r_{xx}}$, $s = \{x, y\}$, for the same wavenumber ranges in Figure 3.4. The wall-normal forcing cases in Figure 3.5(b) and Figure 3.5(d) closely resemble their counterparts for u in Figure 3.4(b) and Figure 3.4(d), respectively, with the signature of $k_z = 0$ modes emerging for the higher of the two Wi , but still with the overall highest amplification occurring for $k_x = 0$ modes. For the streamwise forcing shown in Figure 3.5(a) and Figure 3.5(b), however, $k_z = 0$ modes become the globally most amplified for $Wi = 20$. Note also that the peak amplifications for r_{xx} are several orders of magnitude higher than those for u , and that the amplification increases by at least an order of magnitude from $Wi = 7$ to $Wi = 20$, indicating that at EIT, forcing of the conformation tensor is significantly more amplified than that for the velocity field.

The presence of highly amplified $k_z = 0$ modes for $Wi = 20$ is consistent with the observations of the structural changes in the DNS. Indeed, Figure 3.3(b) shows that the largest spectral content occurs for $k_x L_x / 2\pi = 2$. For a box length $L_x = 10$, this corresponds to $k_x \approx 1.26$, which is in very good agreement with the location of the strip displayed in Figures 3.4 and 3.5. Furthermore, the structure of the most amplified mode for $k_z = 0$ closely resembles the full DNS field. Figure 3.6 shows contours of the r_{xx} component of the most amplified (over ω) resolvent mode for $(k_x, k_z) = (1.26, 0)$ and $Wi = 20$, plotted in the bottom half of the channel only. The peak amplification is attained for a frequency $\omega = 0.46$, or wavespeed $c = \omega/k_x = 0.37$, which corresponds to a critical layer at $y \approx \pm 0.8$. Figure 3.6 indicates that the mode is highly localized around the critical layer. Plotted in the top half of the channel for comparison are contours of r_{xx} in the $z = L_z/2$ plane from a DNS snapshot. The resemblance is striking – the single resolvent mode accurately captures not only the localization near the wall, but the large streamwise inclination

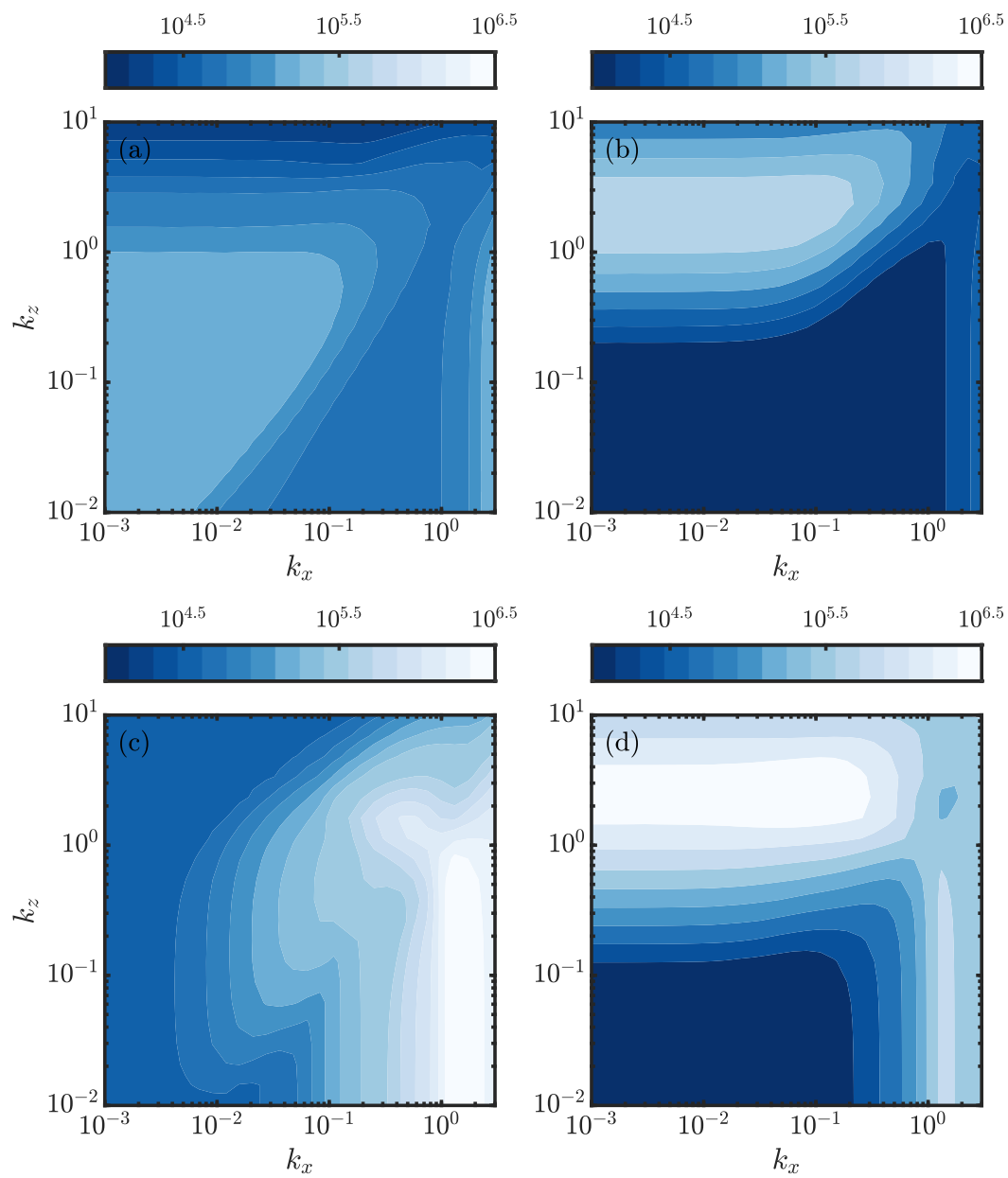


Figure 3.5: H_∞ norms of (a),(c) $\mathcal{H}_{x \rightarrow r_{xx}}$ and (b),(d) $\mathcal{H}_{y \rightarrow r_{xx}}$, with (a),(b) $Wi = 7$; (c),(d) $Wi = 20$.

of the sheets as well. Additionally, the same DNS snapshot and resolvent mode are shown in the $x = L_x/2$ plane in Figure 3.7, which clearly illustrates the nearly two-dimensional nature of EIT. Finally, we emphasize that the only information from the DNS that the resolvent is provided with are the mean profiles, and yet it can still reproduce some of the most salient features from instantaneous flowfields.

3.4 Critical layer mechanisms and structures in EIT

As was demonstrated in the previous section, the most-amplified resolvent mode for $Wi = 20$ reproduces the hallmark structures observed in DNS snapshots of EIT, namely the highly inclined and localized sheet-like structures of large polymer stress fluctuations. While this demonstration is encouraging for resolvent-based low-order modeling of viscoelastic turbulence, we now investigate these structures further, with the goal of gaining some insight into their origin, as well as their role in sustaining EIT. To this end, we briefly take a step back and look at how EIT is approached in a channel at low Re .

Approach to EIT

Figure 3.8 shows the normalized deviation of the friction factor from the laminar value computed from the DNS at $Re = 1500$ as a function of Wi (Shekar et al., 2019). Starting at $Wi = 0$ is Newtonian turbulence. As Wi increases, the friction factor decreases, but the overall flow structure still resembles Newtonian turbulence, consistent with previous results on low levels of drag reduction; correspondingly, this branch is labeled “NT.” The NT state exists up to $Wi \approx 7$, beyond which it abruptly loses existence (schematically illustrated by the dotted red line), causing the flow to relaminarize. This regime of laminar flow persists for a range of Wi , labeled “L” in Figure 3.8. Upon further increase of Wi , however, the laminar state is subject to a new instability and at $Wi \approx 20$ transitions directly into EIT. Further increase in Wi results in only a modest increase in the friction factor, in agreement with the view that EIT corresponds to MDR (Choueiri et al., 2018).

We draw particular attention to the case $Wi = 20$, which was highlighted in Section 3.3 and is shown in Figure 3.3(b). For reference, the inset of Figure 3.8 shows the same spectrum in the inset. What is now apparent is that $Wi = 20$ corresponds to a flow state very near the point where the flow transitions to EIT. Therefore, it is anticipated that this case exhibits the simplest dynamics that are representative of EIT. Furthermore, its proximity to the transition point motivates a stability analysis of laminar state, which we next describe in detail, with a particular emphasis on the

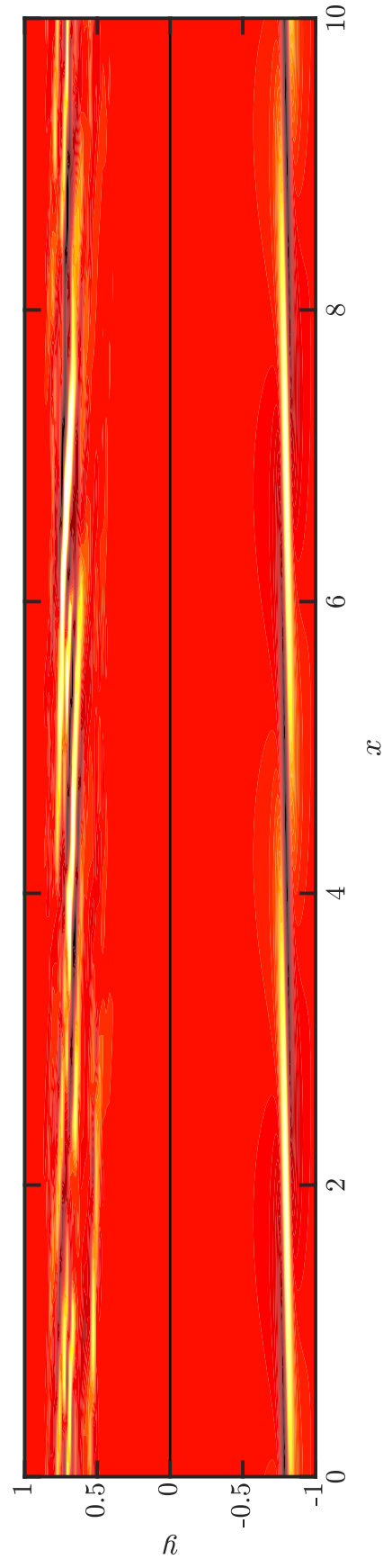


Figure 3.6: Comparison of r_{xx} from DNS and resolvent analysis at $Wi = 20$. The top half of the channel shows the $z = L_z/2$ plane from a DNS snapshot, and the bottom half shows the leading resolvent mode for $(k_x, k_z, \omega) = (1.26, 0, 0.46)$.

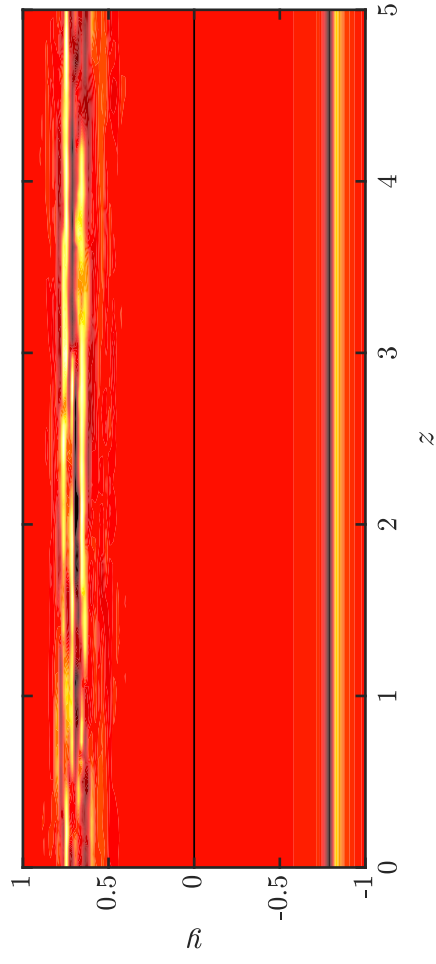


Figure 3.7: Comparison of r_{xx} from DNS and resolvent analysis at $Wi = 20$. The same DNS snapshot and resolvent mode shown in Figure 3.6 are shown in the $x = L_x/2$ plane.

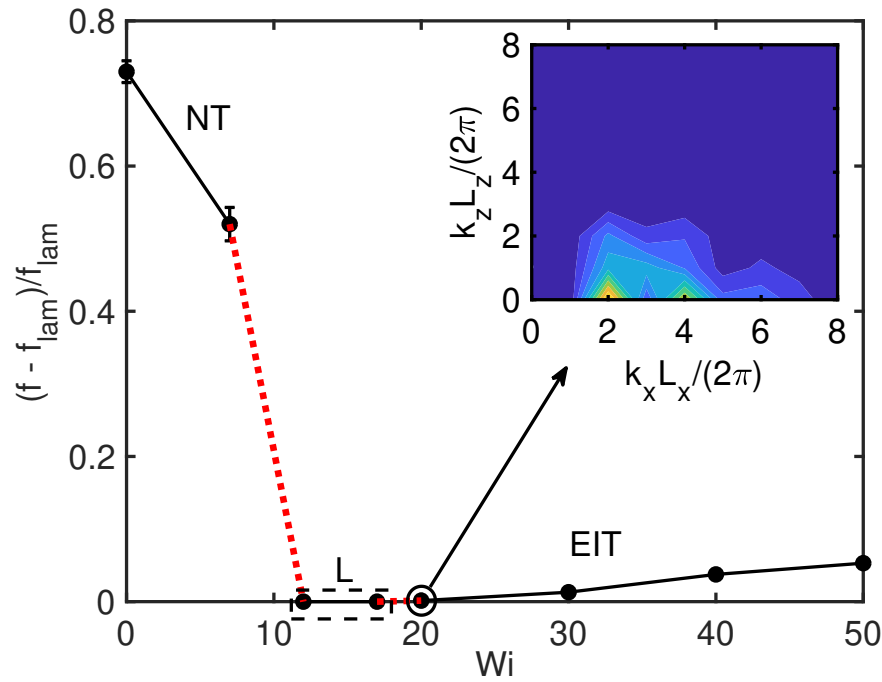


Figure 3.8: Scaled friction factor vs. Wi at $Re = 1500$. Abbreviations “NT”, “L” and “EIT” stand for Newtonian-like turbulence, laminar, and elastoinertial turbulence, respectively. In most cases, the error bars are smaller than the symbols. Red dotted lines indicate the intervals of Wi in which the NT solution loses existence and the EIT solution comes into existence, respectively, as Wi increases. Inset shows the spatial spectrum of the wall normal velocity at $y = 0$ for $Wi = 20$. Here, x - and z -wavenumbers k_x and k_z are reported in scaled form, as $k_x L_x / 2\pi$ and $k_z L_z / 2\pi$. For inset, low is blue, high is yellow. Reproduced from Shekar et al. (2019).

highly localized stress fluctuation structures identified in Section 3.3.

Linear stability analyses of viscoelastic channel flow at high Wi

To shed light on the origin of the highly localized large stress fluctuations, we now consider the evolution of infinitesimal perturbations to the laminar state with given wavenumbers (k_x, k_z) . We perform both modal analyses, i.e., analysis of the spectrum of \mathcal{L} in Equation (3.21), and nonmodal analyses, i.e., resolvent analysis, or analysis of the pseudospectrum of \mathcal{L} (Trefethen et al., 1993; Schmid, 2007; McKeon and Sharma, 2010). In both analyses, the concept of critical layers, i.e., wall-normal positions where the fluid velocity equals the wavespeed of an eigenmode or resolvent mode, is important. While some recent studies suggest the importance of critical layer mechanisms in viscoelastic shear flows (Page and Zaki, 2015; Lee and Zaki, 2017; Haward et al., 2018; Hameduddin et al., 2019), they do not make as direct a connection to EIT as we illustrate here.

Figure 3.9(a) shows the result of the modal analysis (the eigenvalues c) for $Wi = 20$, $(k_x L_x / 2\pi = 2, k_z L_z / 2\pi = (2, 0))$, the wavenumber corresponding to the dominant structures observed in the nonlinear simulations (c.f. Figure 3.3(b)). All eigenvalues fall in the lower half of the complex c plane, implying that the laminar flow is linearly stable³. Of note is the discrete eigenvalue labeled “TS” lying above the continuous spectrum. It is the viscoelastic continuation of the classical Tollmien-Schlichting mode (Drazin and Reid, 2004). For low values of Wi , the mode is less stable than its Newtonian counterpart, while for $Wi \gtrsim 2$, it becomes more stable with increasing elasticity; this non-monotonic behavior has been reported by Zhang et al. (2013), who attribute it to viscoelastic modification of the phase difference between u and v . However, over the range of Wi considered here, viscoelasticity has only a weak effect on the TS eigenvalue. It varies by less than 1% of the Newtonian value, and, importantly, the mode never becomes unstable, implying that finite amplitude disturbances are required to trigger transition to EIT. Despite the small change in c , the conformation tensor disturbance depends very strongly on Wi ; the peak value of r_{xx} grows from zero at $Wi = 0$ to $\sim 10^5$ times the peak value of u at $Wi = 20$.

Although the TS mode ultimately decays, the linear Navier-Stokes equations admit significant disturbance growth at short times or significant amplification of harmonic-in-time disturbances (Schmid, 2007) that may be sufficient for nonlin-

³An extension of Squire’s theorem to Oldroyd-B fluids has been proven by Bistagnino et al. (2007). While there is no such result for FENE-P fluids, we have not observed any three-dimensional linear instabilities in the region of parameter space considered here.

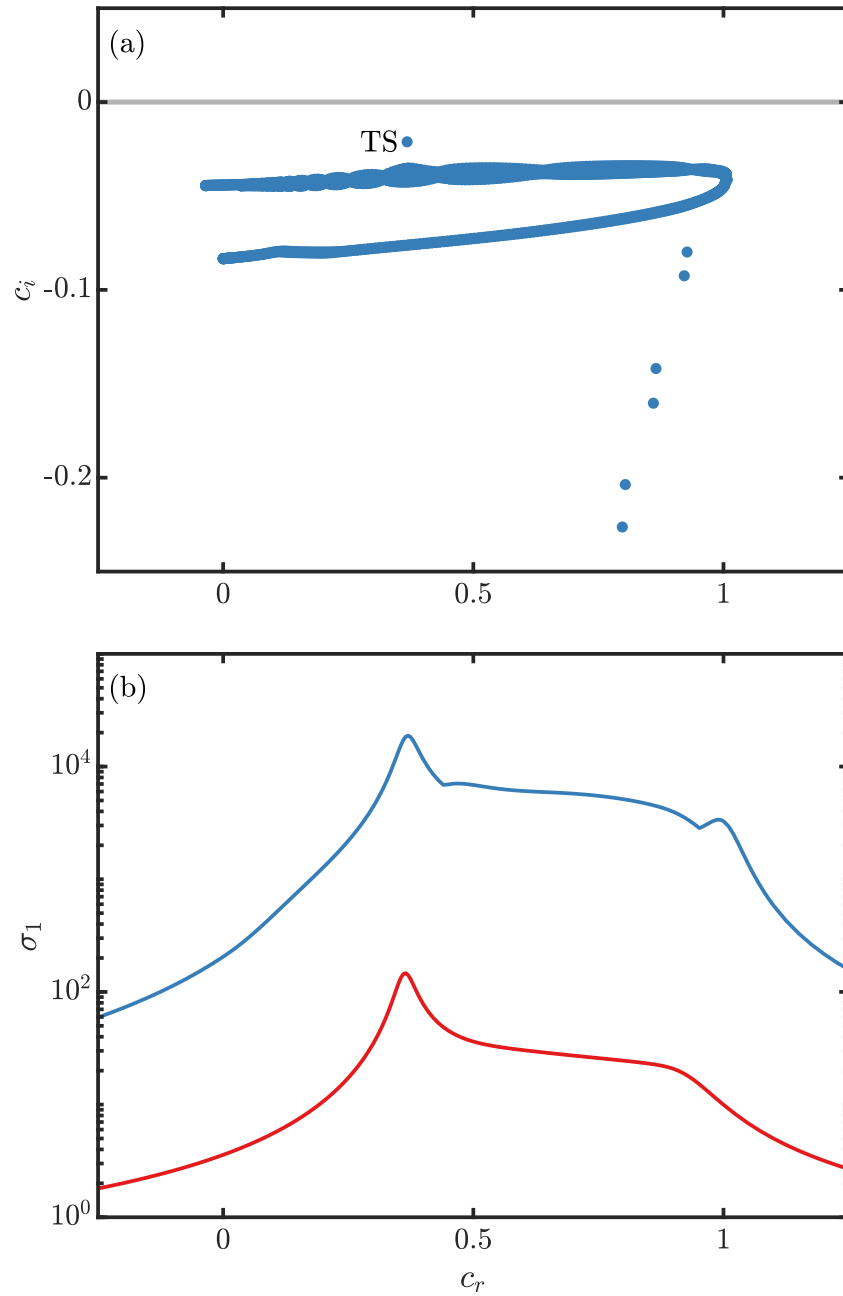


Figure 3.9: (a) Eigenvalue spectrum for $(k_x L_x / 2\pi, k_z L_z / 2\pi) = (2, 0)$ with $Wi = 20$ and $Re = 1500$. The eigenvalue labeled “TS” corresponds to the TS mode. (b) Leading singular value of the resolvent operator for the same wavenumbers and Reynolds number as in (a) and $Wi = 0$ (red) and $Wi = 20$ (blue). Reproduced from Shekar et al. (2019).

ear effects to become significant, potentially triggering EIT. We quantify this amplification by computing the largest singular value σ_1 of the resolvent operator. Figure 3.9(b) shows results for $Wi = 0$ and $Wi = 20$ in the same range of (real) wavespeeds $c = \omega/k_x$ depicted in Figure 3.9(a). The amplification increases dramatically with Wi , with the values at $Wi = 20$ being $\sim 10^2$ times those for $Wi = 0$; this is consistent with the drastic increase in the conformation tensor disturbance amplitude already discussed for the TS mode and suggests that with increasing elasticity, considerably smaller disturbances may be sufficient to trigger self-sustaining nonlinear mechanisms. For both Wi shown in Figure 3.9(b), the maximum amplification occurs for $c \approx 0.37$, which coincides with the wavespeed for the TS mode, suggesting that the most-amplified disturbance may be closely linked to it.

To confirm this, we now examine the structure of the TS eigenmode and the most-amplified resolvent mode, as well as emphasize their connection to the structures observed in EIT. Contours of r_{xx} and v in a 2D slice from a snapshot of the $Wi = 20$ DNS are shown in Figure 3.10(a). Since the structure of the r_{xx} field has been discussed in detail in Section 3.3, here we primarily focus on the v field. While much of the (small scale) v activity is co-located with the stress fluctuations, there are in addition larger-scale v motions that span almost the entirety of the channel. Figure 3.10(b) shows the phase-averaged structures corresponding to $(k_x L_x / 2\pi, k_z L_z / 2\pi) = (2, 0)$, the dominant content in the spectra. To generate this plot, the Fourier mode was extracted from many snapshots, such as the one shown in Figure 3.10(a), and then phase-aligned using the maximum of v before being averaged. The resulting v structures are even across the channel center and extend from one band of the localized r_{xx} sheets to the other.

The structure of the TS eigenmode is shown for $Wi = 20$ in Figure 3.10(c). In the Newtonian case, the disturbance velocity field is a train of spanwise-oriented vortices that span the entire channel; this structure is only weakly modified even at high Wi . The polymer stress disturbance behaves very differently: at $Wi = 20$ it consists of highly inclined sheets that are extremely localized around the critical layers $y = \pm 0.79$ for the TS wavespeed of $c_r \approx 0.37$. Comparison with Figure 3.10(a) and Figure 3.10(b) shows a strong similarity between the eigenmode and the tilted sheetlike structures that are the hallmark of EIT, with the resemblance between the TS mode and the $(k_x L_x / 2\pi, k_z L_z / 2\pi) = (2, 0)$ structure from the DNS in Figure 3.10(b) being particularly striking. Specifically, note that for the TS mode, Figure 3.10(c), v and r_{xx} are even and odd, respectively, with respect to $y = 0$, while

in Figure 3.10(b) these symmetries hold to a good approximation. Figure 3.10(d) shows the leading resolvent mode, which is indeed almost identical to the TS eigenmode in Figure 3.10(c). This result provides additional strong evidence that the structures observed in EIT are closely related to those in viscoelasticity-modified TS waves.

As mentioned above, the fact that the polymer stress fluctuations are localized about the critical layer suggests that they play an important role in the generation of these structures. To elucidate this, Figure 3.11 shows the same r_{xx} as in Figure 3.10 zoomed in on the critical layer in the lower half of the channel. Also shown are streamlines computed in a reference frame co-moving with the wave. In the vicinity of the critical layer, the streamlines exhibit the distinctive Kelvin’s cat’s eye pattern (Drazin and Reid, 2004). Importantly, the cat’s eyes are separated by hyperbolic stagnation points, which are well-known to induce large polymer stretching as the molecules are drawn in and subjected to a large extensional strain rate (Renardy, 2006; Haward and McKinley, 2013). Indeed, the positive fluctuations coincide with the stagnation points, suggesting that they are responsible for the sheet-like structures observed in EIT.

These dynamics carry over into the nonlinear case, as illustrated in Figure 3.12, which shows the structure of a self-sustained nonlinear viscoelastic TS wave for $Re = 3000$, $Wi = 3$. As in Figure 3.11, regions of closed streamlines are separated by stagnation points, from which emerge high values of polymer stretch. Note, however, that unlike Figure 3.11, the highest stretching occurs not at the “instantaneous critical layers” (shown in green lines), but between the stagnation points and the walls. This is due to the lower value of Wi . As we show next, above a certain value of Wi the largest stretching coincides with the critical layer.

Although the amplitude of the linear TS mode is arbitrary, a measure of the relative importance of the conformation tensor and velocity disturbances is the ratio of the peak amplitudes of \hat{r}_{xx} and \hat{v} . This ratio is shown for a range of Wi and $Re = 3000$ in Figure 3.13(a). Two distinct regimes are apparent, with the transition between the two occurring at $Wi \approx 3.1$. The low Wi regime scales as Wi^2 , which is the same scaling as in simple shear flow. The amplitude ratio above the change in slope does not exhibit power law scaling. The change in slope at $Wi \approx 3.1$ can be understood by examining the r_{xx} mode shapes, the magnitudes of which are plotted in Figure 3.13(b) for several values of Wi in the range shown in Figure 3.13(a). For small Wi , the disturbance is largest at the wall and decays rapidly away from

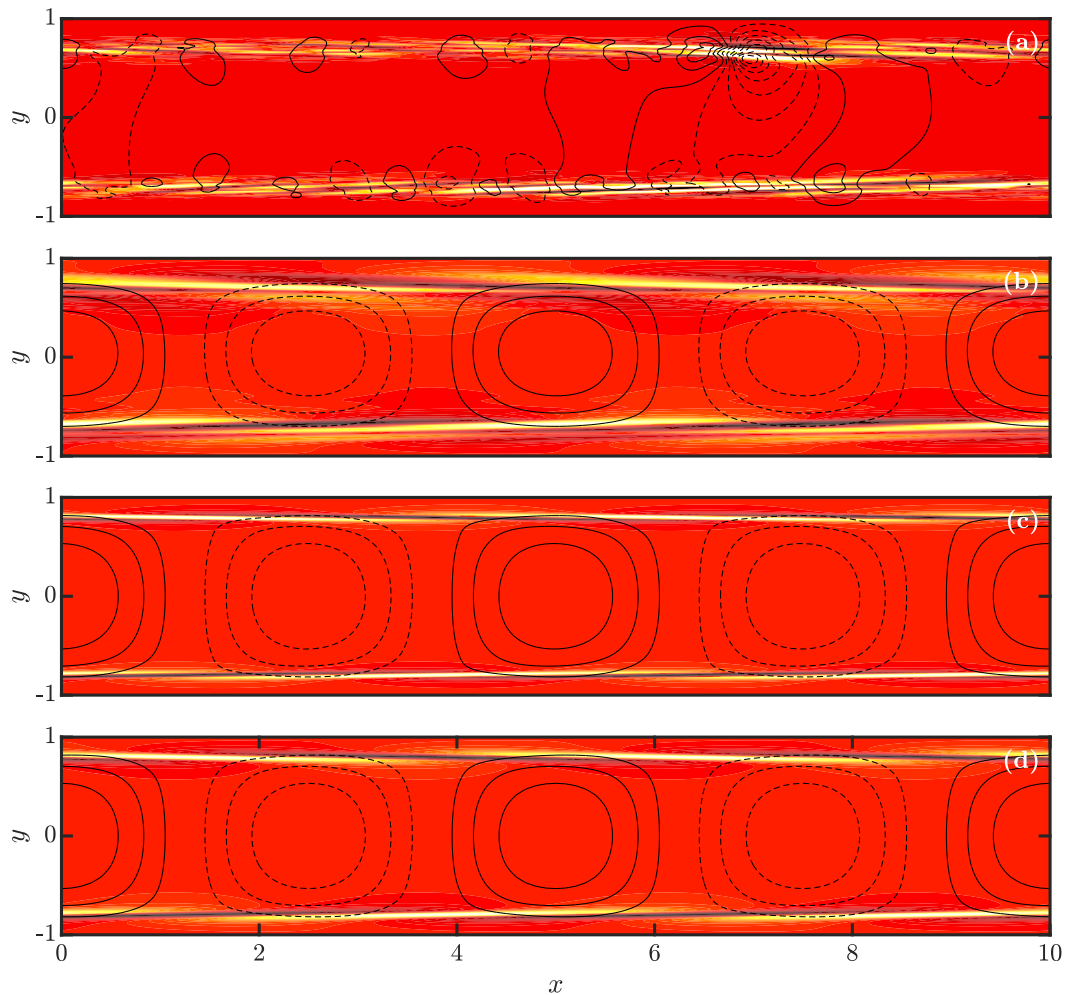


Figure 3.10: (a) Snapshot of v (line contours) and r_{xx} (filled contours) from 3D nonlinear DNS at $Re = 1500$, $Wi = 20$. (b) Phase-matched average $(k_x L_x / 2\pi, k_z L_z / 2\pi) = (2, 0)$ structures from 3D DNS. (c) Structure of the TS mode for $Re = 1500$, $Wi = 20$, and the same wavenumbers as in (b). (d) Structure of the most strongly amplified resolvent mode for $Re = 1500$, $Wi = 20$, the same wavenumbers as in (b), and $c = 0.37$. In all plots, contour levels are symmetric about zero. For v , dashed and solid contours indicate negative and positive values, respectively. For r_{xx} , black, red, and yellow indicate negative, zero, and positive values, respectively. Reproduced from Shekar et al. (2019).

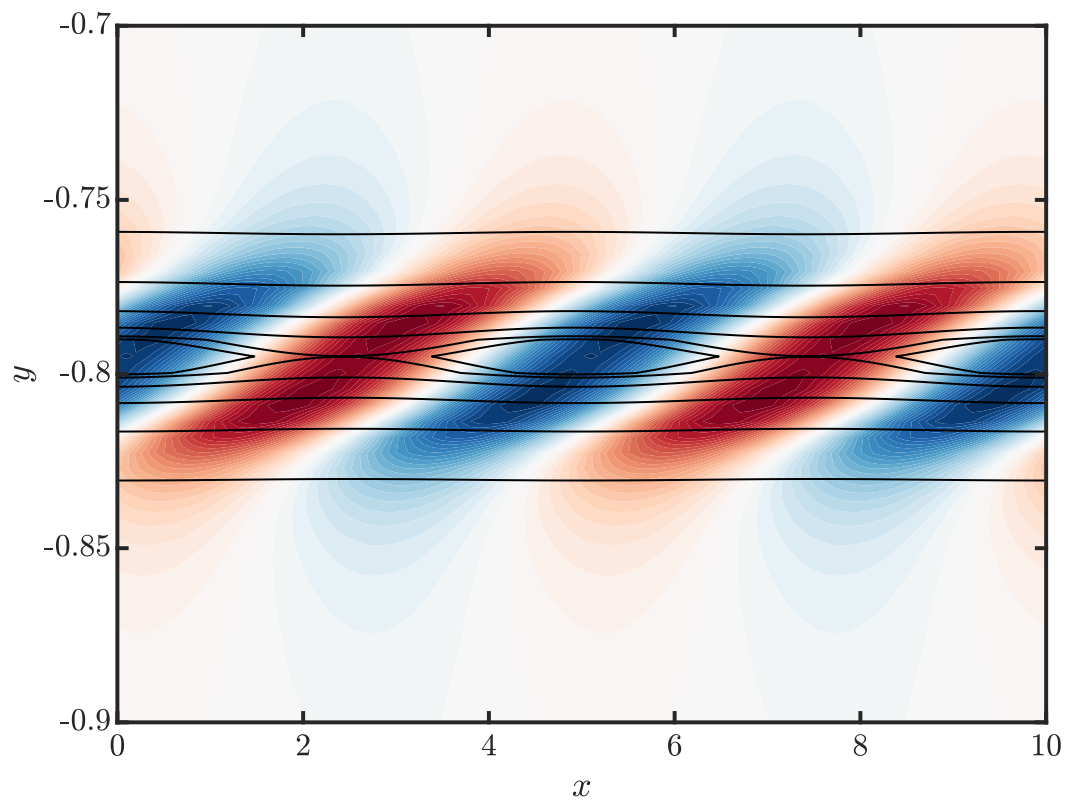


Figure 3.11: Zoomed view of the TS mode r_{xx} (filled contours) and streamlines (line contours) in a reference frame co-moving with the wave for $Re = 1500$, $Wi = 20$. For r_{xx} , blue, white, and red indicate negative, zero, and positive values, respectively.

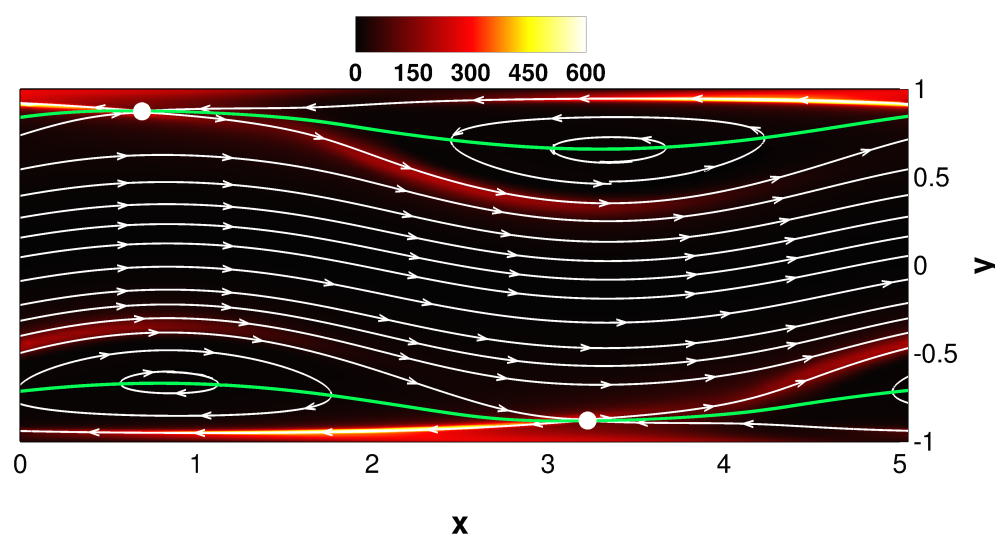


Figure 3.12: Structure of nonlinear self-sustaining TS wave at $Re = 3000$, $Wi = 3$. White streamlines, shown in a reference frame moving with the wavespeed $c = 0.39$, are superimposed on color contours of \tilde{u}_{xx} . Green lines indicate the instantaneous critical layer positions, and white dots indicate the locations of hyperbolic stagnation points. Reproduced from Shekar et al. (2019).

it. Therefore, the Wi^2 scaling in this regime can be explained by the fact that the leading-order approximation of the base flow very near the wall is simple shear. As Wi increases, this value decreases, while a new local maximum emerges and grows, becoming the global maximum just above $Wi = 3$; the arrow in the figure indicates the profile where this occurs. Upon further increase in Wi , the maximum gradually shifts away from the wall, and the modes become increasingly localized around the location of the critical layer. The critical layer for $Wi = 13$ is indicated by the vertical dashed line. This suggests that a critical layer mechanism is responsible for the change in scaling at large Wi , though at present we do not understand the specific origin of this result. Interestingly, the Wi at which a new flow state, dubbed the viscoelastic nonlinear TS attractor (VNTSA) (Shekar et al., 2020), comes into existence is only slightly larger than that at which the transition to critical layer scaling occurs.

Also shown in Figure 3.13(b) is the amplitude ratio computed from the VNTSA for several values of Wi . Excellent agreement between the linear and nonlinear results quantitatively reinforces the TS-like nature of the VNTSA. Additionally, the profile of $|\hat{r}_{xx}|$, averaged in the streamwise direction and over many snapshots, for the VNTSA at $Wi = 13$ is shown by the thick red line in Figure 3.13(b), and the blue line highlights the linear mode for the same Wi . The VNTSA profile exhibits the same localization, and the location of the peak value is in close agreement with the critical layer location.

3.5 Chapter summary

The goal of the present chapter has been to shed light on the origin of the structures and mechanisms underlying EIT at low Reynolds number. First, the differences between polymer drag-reduced turbulence in the low drag reduction regime ($Wi = 7$) and in the regime of EIT ($Wi = 20$) were investigated from a linear perspective. To achieve this, the resolvent analysis of McKeon and Sharma (2010) was extended to viscoelastic fluids obeying the FENE-P constitutive model. The most amplified structures as a function of wavenumbers k_x and k_z were identified, with a focus on the streamwise and wall-normal forcing of the streamwise velocity u and streamwise conformation tensor component r_{xx} .

For $Wi = 20$, modes with $k_z = 0$ and $k_x = O(1)$ can be highly amplified, particularly for streamwise forcing of r_{xx} . This is consistent with observations from DNS that spanwise-oriented structures are dominant in EIT. The importance of $k_z = 0$ modes

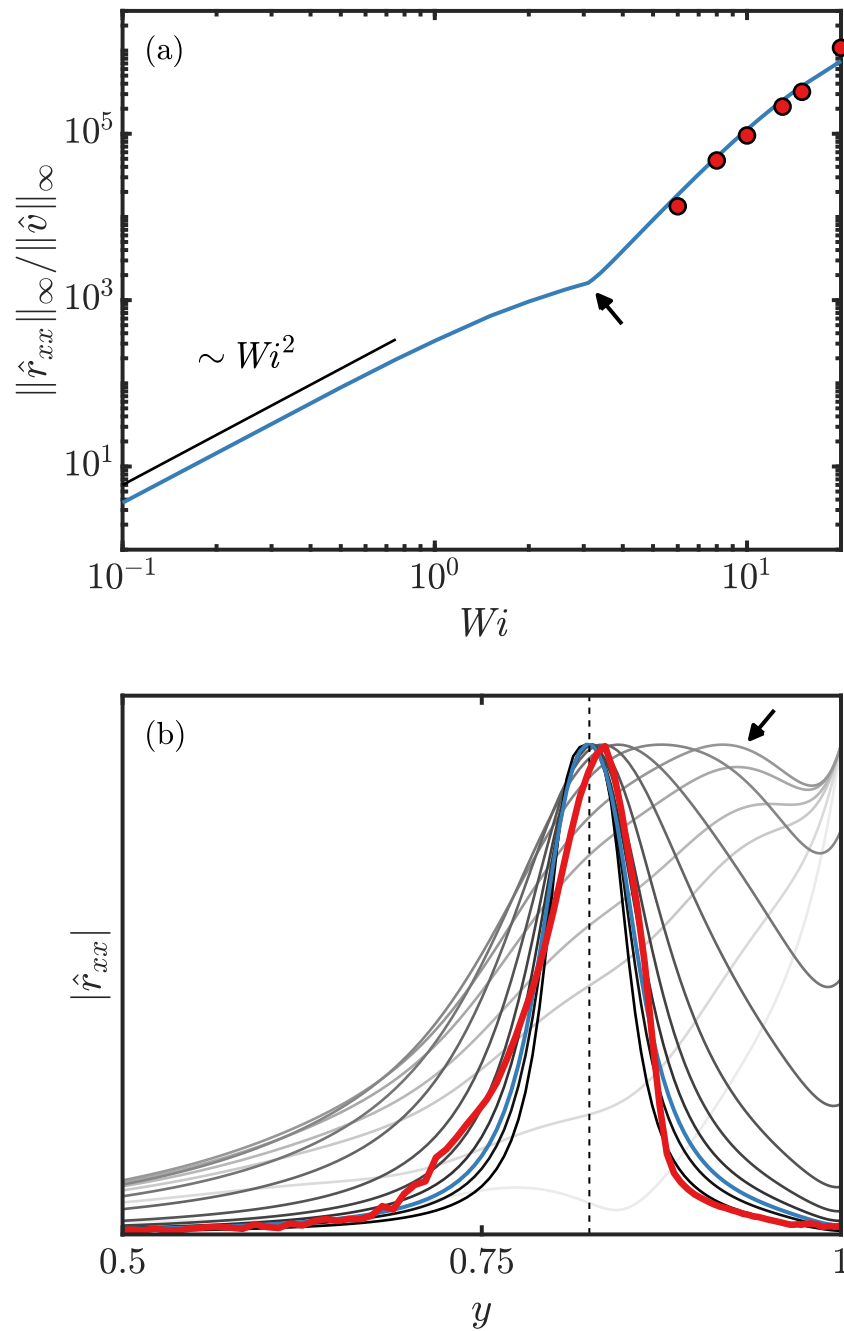


Figure 3.13: (a) Solid blue line: ratio of peak amplitudes of \hat{r}_{xx} and \hat{v} for the linear TS mode as a function of Wi ; circles: amplitude ratio for the VNTSA. (b) Magnitude of \hat{r}_{xx} for the linear TS mode for several values of Wi in the range $[1, 20]$. Darker lines indicate higher values of Wi . The thick red line shows the averaged magnitude of \hat{r}_{xx} from the VNTSA for $Wi = 13$. For comparison, the linear TS mode profile for the same Wi is shown in blue, and the vertical dashed line marks the critical layer location $y_c = 0.825$. The arrow indicates the value of Wi corresponding to the arrow in (a).

in the dynamics of EIT is further underscored by recent work demonstrating that EIT can be sustained in completely two-dimensional simulations (Sid et al., 2018). Additionally, the r_{xx} component of the leading resolvent mode corresponding to the dominant streamwise lengthscale in the $Wi = 20$ DNS bears strong resemblance to snapshots of the full flowfield, reproducing in particular the highly inclined sheets of polymer stretch. Analysis by Page and Zaki (2015) shows that similar tilted sheets of polymer stretch arise in homogeneous viscoelastic shear flow perturbed by a spanwise-oriented vortex.

Streamwise-constant modes remain highly amplified at $Wi = 20$, similar to findings of previous nonmodal stability analyses (Hoda et al., 2009; Lieu et al., 2013), which place a heavy emphasis on such structures, citing them as a possible mechanism for bypass transition analogous to that in Newtonian fluids. While streamwise-elongated structures are not observed in the DNS of EIT shown here, we note that recent experiments (Choueiri et al., 2018) and simulations (Lopez et al., 2019) of EIT in a pipe do observe them. This discrepancy perhaps has to do with the difference of domain size (Lopez et al., 2019).

Next, due to the fact that the $Wi = 20$ case is very close to the point where EIT comes into existence at $Re = 1500$, stability analyses of the laminar state were performed in an attempt to further understand the origin of the structures characteristic of EIT. Through a modal analysis focusing on the wavenumbers corresponding to the dominant spectral content in the DNS, it was demonstrated that the flow is linearly stable, and therefore the instability leading to EIT in this region of parameter space is subcritical in nature. Resolvent analysis showed that amplification of disturbances grows considerably with increasing elasticity. A distinct peak in the amplification was observed at a wavespeed corresponding to that of the least stable eigenmode, the viscoelastic extension of the TS mode.

A detailed comparison of the structure of the TS mode and the most amplified resolvent mode confirmed the two are nearly identical and therefore provides strong evidence that the highly localized stress fluctuations observed in EIT are TS-like in nature. Furthermore, the localization was found to occur at the critical layer, which locally resembles the classical Kelvin's cat's eyes pattern. Situated between the cat's eyes are hyperbolic stagnation points, which coincide with the maxima of the conformation tensor fluctuations, thereby supporting the idea that they are the origin of the sheet-like structures observed in EIT.

The observations made about the linear TS mode were seen hold for nonlinear self-

sustaining TS waves computed for $Re = 3000$ and $Wi = 3$. However, in that case, the largest polymer stretching occurs between the stagnation points and the walls. This discrepancy was explained by computation of the TS mode at $Re = 3000$ for a range of Wi . For $Wi \lesssim 3$, the maximum of \hat{r}_{xx} modes is at the wall. For higher Wi , this maximum gradually shifts away from the wall and toward the critical layer location. Accompanying this is a change in the scaling of the ratio of the peak amplitudes of \hat{r}_{xx} and \hat{v} from $\sim Wi^2$, corresponding to that of simple shear flows, to a critical layer scaling, which does not appear to obey a power law, at least for the range of Wi considered here. This is possibly an effect of the finite extensibility in the FENE-P model, but further analysis is needed to determine if the Oldroyd-B model yields a simple scaling behavior.

Finally, we note that it was recently shown that viscoelastic pipe flow of Oldroyd-B fluids can be linearly unstable to center-localized modes with wavespeed $c_r \approx 1$ (Garg et al., 2018), and a similar instability exists in channel flow. However, we estimate that for the present parameter values, this mode only becomes relevant for Wi more than an order of magnitude larger than what was considered here. Furthermore, center-localized structures are not observed in the DNS of EIT, so we do not believe them to be relevant here. Nonetheless, it illustrates that there may be different pathways to EIT in different regions of parameter space.

Chapter 4

INTERACTION OF FORCED ORR-SOMMERFELD AND
SQUIRE MODES IN A LOW-ORDER REPRESENTATION OF
TURBULENT CHANNEL FLOW

The contents of this chapter have been previously published in¹:

McMullen, R. M., Rosenberg, K., and McKeon, B. J. (2020). “Interaction of forced Orr-Sommerfeld and Squire modes in a low-order representation of turbulent channel flow”. arXiv: 2001.02785 [physics.flu-dyn].

While the utility of decomposing the resolvent operator into Orr-Sommerfeld and Squire modes for highly simplified flows like ECS has been established (Rosenberg and McKeon, 2019b), an open question is whether or not it remains relevant for high Reynolds number turbulence. In this chapter, it is shown that the second-order statistics of turbulent channel flow can be accurately represented using a low-order approximation based on this framework. It is additionally shown that the vorticity produced by the Orr-Sommerfeld and Squire modes act to oppose each other, and this observation reveals information about how the resolvent weights for the two families scale relative to each other with Reynolds number. Altogether, these insights point to a mechanism in turbulent channel flow that is important for low-order modeling efforts.

4.1 Formulation

Resolvent analysis of turbulent channel flow

Resolvent analysis was introduced for a generic dynamical system in Section 2.1. Here, we provide the details of the formulation relevant to incompressible flow of a Newtonian fluid in a channel, the starting point of which is the incompressible NSE:

$$\partial_t \tilde{\mathbf{u}} + (\tilde{\mathbf{u}} \cdot \nabla) \tilde{\mathbf{u}} = -\nabla \tilde{p} + Re_\tau^{-1} \nabla^2 \tilde{\mathbf{u}}, \quad (4.1a)$$

$$\nabla \cdot \tilde{\mathbf{u}} = 0, \quad (4.1b)$$

¹We acknowledge Kevin Rosenberg for numerous discussions and feedback that helped guide the contents of this chapter, as well as for providing the DNS data used in Figure 4.6.

which are nondimensionalized using the friction velocity u_τ and channel half-height h ; $Re_\tau = u_\tau h/\nu$ is the friction Reynolds number. The velocity field is first Reynolds decomposed as $\tilde{\mathbf{u}} = \mathbf{U} + \mathbf{u}$, where $\mathbf{U} = (U(y) \ 0 \ 0)^T$ is the turbulent mean velocity profile and \mathbf{u} are the fluctuations about the mean, and then Fourier transformed in the homogeneous wall-parallel and temporal directions x , z , and t , resulting in equations for the Fourier coefficients, denoted by $(\hat{\cdot})$. For each wavenumber-frequency triplet $(k_x \ k_z \ \omega)^T \neq \mathbf{0}$, we have

$$-i\omega \hat{\mathbf{u}} + (\mathbf{U} \cdot \nabla) \hat{\mathbf{u}} + (\hat{\mathbf{u}} \cdot \nabla) \mathbf{U} + \nabla \hat{p} - Re_\tau^{-1} \nabla^2 \hat{\mathbf{u}} = \hat{\mathbf{f}} \quad (4.2a)$$

$$\nabla \cdot \hat{\mathbf{u}} = 0, \quad (4.2b)$$

where $\mathbf{f} = -(\mathbf{u} \cdot \nabla) \mathbf{u} + \langle (\mathbf{u} \cdot \nabla) \mathbf{u} \rangle$ and $\langle \cdot \rangle$ denotes an averaged quantity, is interpreted as a forcing that drives the dynamics linear in $\hat{\mathbf{u}}$. The pressure can be projected out of Equation (4.2) using the standard mapping to wall-normal velocity \hat{v} and wall-normal vorticity $\hat{\eta} = ik_z \hat{u} - ik_x \hat{w}$. The equations are then concisely written as

$$\begin{pmatrix} \hat{v} \\ \hat{\eta} \end{pmatrix} = \mathcal{H}(k_x, k_z, \omega) \hat{\mathbf{g}}, \quad (4.3)$$

where

$$\mathcal{H} = \begin{pmatrix} -i\omega - \Delta^{-1} \mathcal{L}^{\text{OS}} & 0 \\ -ik_z U' & -i\omega - \mathcal{L}^{\text{SQ}} \end{pmatrix}^{-1} \quad (4.4)$$

is the resolvent operator, $\Delta = \mathcal{D}^2 - k^2$, $\mathcal{D} = d/dy$, $k^2 = k_x^2 + k_z^2$, and $U' = \mathcal{D}U$. Additionally,

$$\mathcal{L}^{\text{OS}} = ik_x(U'' - U\Delta) + Re_\tau^{-1} \Delta^2, \quad (4.5a)$$

$$\mathcal{L}^{\text{SQ}} = -ik_x U + Re_\tau^{-1} \Delta \quad (4.5b)$$

are the Orr-Sommerfeld (OS) and Squire (SQ) operators, respectively. The forcing term $\hat{\mathbf{g}} = (\hat{g}_v \ \hat{g}_\eta)^T$ in Equation (4.3) is related to $\hat{\mathbf{f}}$ via

$$\hat{\mathbf{g}} = \underbrace{\begin{pmatrix} -ik_x \Delta^{-1} \mathcal{D} & -k^2 \Delta^{-1} & -ik_z \Delta^{-1} \mathcal{D} \\ ik_z & 0 & -ik_x \end{pmatrix}}_{\mathcal{B}} \hat{\mathbf{f}}. \quad (4.6)$$

As pointed out by Rosenberg and McKeon (2019b), only the solenoidal part of $\hat{\mathbf{f}}$ contributes to $\hat{\mathbf{g}}$ since the irrotational component lies in the null space of \mathcal{B} .

Following Equation (2.7), we compute the SVD of \mathcal{H} . On both the input and output spaces we adopt the standard kinetic energy inner product (Schmid and Henningson,

2001):

$$(\mathbf{x}_1, \mathbf{x}_2) = \int_{-1}^1 \mathbf{x}_2^* \mathbf{Q} \mathbf{x}_1 dy, \quad (4.7)$$

where $(\cdot)^*$ denotes the conjugate transpose and

$$\mathbf{Q} = \frac{1}{k^2} \begin{pmatrix} -\Delta & 0 \\ 0 & 1 \end{pmatrix}. \quad (4.8)$$

The rank- N approximation of Equation (4.3) is obtained from Equation (2.11). It has been shown that \mathcal{H} is low-rank for a large portion of spectral space that is energetically significant (Moarref et al., 2013a), and this low-rank behavior has previously been exploited to model salient features in wall-bounded turbulence (McKeon and Sharma, 2010; Sharma and McKeon, 2013; Moarref et al., 2013a).

Finally, in order to compute the second-order velocity statistics, the velocity $\hat{\mathbf{u}}$ is recovered from the response via

$$\hat{\mathbf{u}} = \frac{1}{k^2} \begin{pmatrix} ik_x \mathcal{D} & -ik_z \\ k^2 & 0 \\ ik_z \mathcal{D} & ik_x \end{pmatrix} \begin{pmatrix} \hat{v} \\ \hat{\eta} \end{pmatrix}. \quad (4.9)$$

Orr-Sommerfeld and Squire decomposition of the resolvent

As discussed in Section 2.1, the decomposition of \mathcal{H} given in Equation (2.7), hereafter referred to as the standard resolvent decomposition, is optimal in the kinetic energy norm induced by the inner product in Equation (4.7). However, in wall-bounded turbulence the kinetic energy is often dominated by the streamwise velocity, which means that all three velocity components may not be approximated uniformly well (Moarref et al., 2014a; Sharma et al., 2016). In such situations, an alternative decomposition that more faithfully represents the underlying dynamics may be desirable. This idea has been explored previously by Juttijudata et al. (2005), who transformed near-wall data from turbulent channel flow into Squire's coordinate system and then performed POD on modes associated with the streamwise streaks and rolls separately. While the resulting basis functions are energetically suboptimal compared to those from standard POD, they demonstrate that the reconstruction of wall-normal, spanwise, and Reynolds shear stress statistics improves substantially.

In a similar spirit, Rosenberg and McKeon (2019b) proposed the following alternative decomposition of \mathcal{H} . Note that Equation (4.3) can be rewritten as

$$\begin{pmatrix} \hat{v} \\ \hat{\eta} \end{pmatrix} = \begin{pmatrix} \mathcal{H}_{vv} & 0 \\ \mathcal{H}_{\eta v} & \mathcal{H}_{\eta\eta} \end{pmatrix} \begin{pmatrix} \hat{g}_v \\ \hat{g}_\eta \end{pmatrix}, \quad (4.10)$$

where

$$\mathcal{H}_{vv} = \left(-i\omega - \Delta^{-1} \mathcal{L}^{\text{OS}} \right)^{-1}, \quad (4.11a)$$

$$\mathcal{H}_{\eta\eta} = \left(-i\omega - \mathcal{L}^{\text{SQ}} \right)^{-1}, \quad (4.11b)$$

$$\mathcal{H}_{\eta v} = -ik_z \mathcal{H}_{\eta\eta} U' \mathcal{H}_{vv}. \quad (4.11c)$$

Apparently, \mathcal{H}_{vv} and $\mathcal{H}_{\eta v}$ are forced by \hat{g}_v only, while $\mathcal{H}_{\eta\eta}$ is forced by \hat{g}_η only. This motivates the separation of the response $(\hat{v} \ \hat{\eta})^T$ into two distinct families:

$$\begin{pmatrix} \hat{v} \\ \hat{\eta}^{\text{OS}} \end{pmatrix} = \begin{pmatrix} \mathcal{H}_{vv} \\ \mathcal{H}_{\eta v} \end{pmatrix} \hat{g}_v, \quad (4.12a)$$

$$\hat{\eta}^{\text{SQ}} = \mathcal{H}_{\eta\eta} \hat{g}_\eta. \quad (4.12b)$$

In the following, we refer to the family of modes in Equation (4.12a) as Orr-Sommerfeld (OS) modes and the family in Equation (4.12b) as Squire (SQ) modes. The separation of $\hat{\eta}$ into two distinct families is common practice in linear stability analysis, where the SQ and OS modes are, respectively, the homogeneous and particular solutions of the Squire equation: $(-i\omega - \mathcal{L}^{\text{SQ}})\hat{\eta} = -ik_z U' \hat{v}$ (Schmid and Henningson, 2001). That is, the OS modes can be interpreted as a response to the wall-normal velocity. This interpretation still holds in the nonlinear setting, since the second component of Equation (4.12a) can be written as $\hat{\eta}^{\text{OS}} = -ik_z \mathcal{H}_{\eta\eta} U' \hat{v}$. However, the SQ modes are no longer the homogeneous solutions, but are now interpreted as the response to forcing by \hat{g}_η .

Note that only the OS modes contain a \hat{v} response, such that the SQ modes contribute only to the $\hat{\eta}$ response, i.e., to the wall-parallel velocity components. There is thus the potential for interaction between the OS and SQ vorticity in ways that are not admitted by the standard resolvent decomposition. This fact is of central importance for the OS-SQ resolvent decomposition, and it will be demonstrated in Section 4.2 that this drastically improves the accuracy of a low-order resolvent-based representation of the second-order statistics for turbulent channel flow.

An SVD of each operator in Equation (4.12) is performed separately, and the resulting decomposition is referred to as the OS-SQ decomposition of the resolvent. The approximation of the response becomes

$$\begin{pmatrix} \hat{v} \\ \hat{\eta} \end{pmatrix} \approx \sum_{j=1}^{N^{\text{OS}}} \boldsymbol{\psi}_j^{\text{OS}} \sigma_j^{\text{OS}} \chi_j^{\text{OS}} + \sum_{k=1}^{N^{\text{SQ}}} \boldsymbol{\psi}_k^{\text{SQ}} \sigma_k^{\text{SQ}} \chi_k^{\text{SQ}}. \quad (4.13)$$

Note that Equation (4.13) is now a sum of $N^{\text{OS}} + N^{\text{SQ}}$ terms. Furthermore, while the left and right singular vectors of each family still comprise orthonormal sets with respect to the inner product given in Equation (4.7), it is not guaranteed that modes belonging to different families are orthonormal, e.g., $(\psi_j^{\text{OS}}, \psi_k^{\text{SQ}}) \neq \delta_{jk}$ in general.

Empirical determination of the resolvent weights via convex optimization

The singular values and vectors are computed directly from the resolvent operator, which depends only on the (assumed known) mean velocity profile U , whereas computation of the weights requires solution of a nonlinear programming problem (McKeon et al., 2013). This can be done exactly in special cases, such as for exact coherent states (ECS) (Rosenberg, 2018). However, it rapidly becomes intractable with an increasing number of degrees of freedom, and, to our knowledge, fully turbulent flows remain out of reach.

Consequently, several attempts have been made to determine the weights empirically (Moarref et al., 2014a; Gómez et al., 2016; Beneddine et al., 2016; Zare et al., 2017; Towne et al., 2018). In particular, Moarref et al. (2014a) used convex optimization to compute the weights that minimize the deviation between a resolvent-based representation of the energy spectra and DNS data. We take the same approach here and largely adopt their formulation, with the major exception that we employ the OS-SQ decomposition discussed in Section 4.1. That is, for given N^{OS} and N^{SQ} , we attempt to approximate the DNS statistics using the approximation given in Equation (4.13).

As introduced by Moarref et al. (2014a), the resolvent three-dimensional streamwise energy spectra are

$$E_r(y, k_x, k_z, c) = \text{Re}\{\text{tr}(\mathbf{A}_r \mathbf{X})\}, \quad (4.14)$$

with $r \in \{uu, vv, ww, uv\}$, and where $\text{Re}\{\cdot\}$ is the real part of a complex number and $\text{tr}(\cdot)$ is the matrix trace. Note that we have chosen to parameterize the spectra in terms of the wavespeed $c = \omega/k_x$ since resolvent modes tend to be localized about the critical layers y_c , where $U(y_c) = c$ (McKeon and Sharma, 2010), and it has been observed experimentally that the range of energetic wavespeeds is relatively compact, with the most energetic motions typically being confined to the range $8 \lesssim c \lesssim U_{cl}$ (LeHew et al., 2011), where U_{cl} is the mean centerline velocity. In Equation (4.14), the matrix \mathbf{A}_{uu} , for example, with entries

$$A_{uu,ij} = \sigma_i \sigma_j \hat{u}_i \hat{u}_j^*, \quad (4.15)$$

represents the contributions of the singular values and response modes and can be determined *a priori* from the SVD of the resolvent. The matrix \mathbf{X} , with entries

$$\mathbf{X}_{ij} = \chi_i^* \chi_j, \quad (4.16)$$

is the weights matrix. Apparent from this definition is that $\mathbf{X}^T = \mathbf{X} \mathbf{X}^* \geq \mathbf{0}$, where χ is the vector of weights and \geq denotes the Löwner order, i.e., \mathbf{X} is a rank-1 positive-semidefinite matrix. The OS-SQ decomposition is incorporated into this framework simply by partitioning the \mathbf{A}_r and \mathbf{X} matrices as

$$\mathbf{A}_r = \begin{pmatrix} \mathbf{A}_r^{\text{OS/OS}} & \mathbf{A}_r^{\text{OS/SQ}} \\ \mathbf{A}_r^{\text{SQ/OS}} & \mathbf{A}_r^{\text{SQ/SQ}} \end{pmatrix}, \quad \mathbf{X} = \begin{pmatrix} \mathbf{X}^{\text{OS/OS}} & \mathbf{X}^{\text{OS/SQ}} \\ \mathbf{X}^{\text{OS/SQ}*} & \mathbf{X}^{\text{SQ/SQ}} \end{pmatrix}, \quad (4.17)$$

where the superscript X/Y denotes the family of the i th and j th mode, respectively, in Equations (4.15) and (4.16).

The goal is to compute the weights matrix such that the deviation between the wavespeed-integrated resolvent spectra in Equation (4.14) and time-averaged DNS spectra is minimized. After discretization of the wavespeed range $c \in [0, U_{cl}]$, this can be formally cast as the following optimization problem: For fixed k_x and k_z ,

$$\begin{aligned} & \underset{\{\mathbf{X}_l\}_{l=1,2,\dots,N_c}, e}{\text{minimize}} && e \\ & \text{subject to} && \frac{\|E_r^{\text{DNS}} - \sum_{l=1}^{N_c} k_x \text{dc Re}\{\text{tr}(\mathbf{A}_{r,l} \mathbf{X}_l)\}\|^2}{\|E_r^{\text{DNS}}\|^2} \leq e \\ & && \mathbf{X}_l \geq \mathbf{0}, \quad l = 1, 2, \dots, N_c, \end{aligned} \quad (4.18)$$

where the subscript l denotes a quantity evaluated at $c = c_l$. Note that the norm $\|\cdot\|$ is not the one induced by Equation (4.7). It is defined as

$$\|f\|^2 = \int_{y_{\min}^+}^{y_{\max}^+} |f(\log y^+)|^2 \text{d log } y^+ \quad (4.19)$$

and is designed to penalize deviations across the channel equally (Moarref et al., 2014a). Thus deviations from the DNS spectra are penalized for $5 \leq y_{\min}^+ \leq y^+ \leq y_{\max}^+ < Re\tau$.

Equation (4.18) is a semidefinite program for the weights matrices \mathbf{X}_l and can therefore be solved efficiently using a convex optimization software package. Note that imposing the rank-1 constraint on the \mathbf{X}_l would make Equation (4.18) non-convex. Moarref et al. (2014a) employed an iterative rank-reduction procedure to recover rank-1 matrices from the full-rank solution (Huang and Palomar, 2010).

However, we do not employ this algorithm here and instead choose to work with the full-rank weights matrices. In this case, the \mathbf{X}_l can be interpreted as the covariance matrices of the weights, similar to Towne et al. (2018). Finally, since the optimization is performed for second-order statistics, the present approach does not provide phase information about modes with different wavenumbers. This means that the computed weights do not yield a closed, self-consistent system, as such information is necessary to recover the mean velocity profile as well as the fluctuations. Extension of the method to incorporate phase is a direction for future work.

Numerical details

The resolvent operators are discretized in MATLAB using a Chebyshev pseudospectral method (Weideman and Reddy, 2000); all results presented here use 203 Chebyshev polynomials. The SVDs of the discretized operators are performed with a random matrix algorithm, which is faster than MATLAB's built-in `svd()` (Halko et al., 2011). The time-averaged two-dimensional DNS spectra for $Re_\tau = 934$ and $Re_\tau = 2003$ are obtained from Hoyas and Jiménez (2006), and for $Re_\tau = 4219$ from Lozano-Durán and Jiménez (2014)². Additionally, spectra were generated for $Re_\tau = 185$ using Channelflow (Gibson, 2014). The resolutions of all the DNS considered are given in Table 4.1. Also shown in Table 4.1 is the number of planes N_{sp} for which spectra are available for each simulation.

For the results presented in Section 4.2, which focus on $Re_\tau = 2003$, the DNS spectra are interpolated onto a grid of $N_{k_x} = 30$ by $N_{k_z} = 31$ logarithmically spaced wavenumbers, which is sufficient to reproduce the general shape of the spectra. Furthermore, it has recently been shown that statistics such as the uv Reynolds stress can be accurately reproduced even when retaining only about 2% of the wavenumbers from DNS (Toedtli et al., 2019). Both the spectra and resolvent modes are interpolated onto a common grid of $N_y = 60$ logarithmically spaced points in the wall-normal direction, and the wavespeed range $c \in [0, U_{cl}]$ is discretized into $N_c = 100$ linearly spaced wavespeeds. The optimization problem Equation (4.18) is then solved with CVX (Grant and Boyd, 2014). The results are insensitive to further increases in N_y and N_c (Moarref et al., 2014a). Though sensitivity to increases in N_{sp} could not be tested with the available data, the fact that the shapes of the spectra and intensities are faithfully reproduced in Figures 4.1 and 4.2, respectively, suggests that changes in the results would be insignificant.

²The authors appreciate Javier Jiménez making the spectra for the $Re_\tau = 934$ and $Re_\tau = 2003$ simulations publicly available, as well as Adrián Lozano-Durán sharing the spectra for $Re_\tau = 4219$.

Table 4.1: Resolutions of the DNS from which spectra were obtained for the optimization. N_{sp} is the number of planes for which spectra are available.

Re_τ		N_x	N_y	N_z	N_{sp}
185	(Channelflow, present work)	384	129	128	65
934	(Hoyas and Jiménez, 2006)	1024	385	768	18
2003	(Hoyas and Jiménez, 2006)	2048	635	1536	20
4219	(Lozano-Durán and Jiménez, 2014)	1024	1081	1024	22

4.2 Analysis of the optimized spectra

Reconstruction of time-averaged statistics

The accuracy of the optimized spectra is evaluated by comparing them to the time-averaged statistics from the DNS for $Re_\tau = 2003$. The premultiplied 1D k_x spectra,

$$k_x E_r(y, k_x) = \int_{k_{z,\min}}^{k_{z,\max}} \int_0^{U_{cl}} k_x^2 E_r(y, k_x, k_z, c) dc dk_z, \quad (4.20)$$

using $N^{\text{OS}} = N^{\text{SQ}} = 3$ modes, i.e., six modes per wavenumber-frequency triplet, are compared to the DNS in the right column of Figure 4.1, which is plotted in terms of $\lambda_x^+ = 2\pi/k_x^+$. Clearly, $N^{\text{OS}} = N^{\text{SQ}} = 3$ modes is sufficient to accurately reproduce the spectra since the overall agreement between the resolvent and DNS spectra is very good, and in particular, the peaks are captured almost exactly. The only significant discrepancies are in $k_x E_{uu}$ at large λ_x^+ and $y^+ \lesssim 100$ and $-k_x E_{uv}$ at large λ_x^+ and $y^+ \lesssim 50$. Further discussion of these discrepancies, as well as the accuracy of the optimized spectra using different numbers of modes is given in Section 4.2. Also shown in the left column are the spectra obtained using the standard decomposition with the same total number of modes. The performance is significantly worse, with $k_x E_{uu}$ and $k_x E_{ww}$ being greatly over-predicted, and $k_x E_{vv}$ and $-k_x E_{uv}$ being under-predicted. In fact, the standard resolvent decomposition fails to capture the 90% energy level (darkest blue contours) for $-k_x E_{uv}$. Subsequent integration over k_x gives the intensities, which are shown in figure Figure 4.2. The deviation errors are 4.3%, 0.95%, 0.66%, and 3.8% for $\langle u^2 \rangle$, $\langle v^2 \rangle$, $\langle w^2 \rangle$, and $\langle -uv \rangle$, respectively. These should be compared with errors of 30%, 14%, 12%, and 31% using the standard resolvent decomposition, shown in the dashed curves.

As the goal of the optimized spectra is to obtain a *low-order* representation of the spectra, it is worth comparing the number of degrees of freedom of the resolvent spectra to the original DNS. For a given k_x, k_z , the $Re_\tau = 2003$ DNS spectra were computed using $N_y = 665$ wall-normal grid points and $N_t = 7730$ snapshots

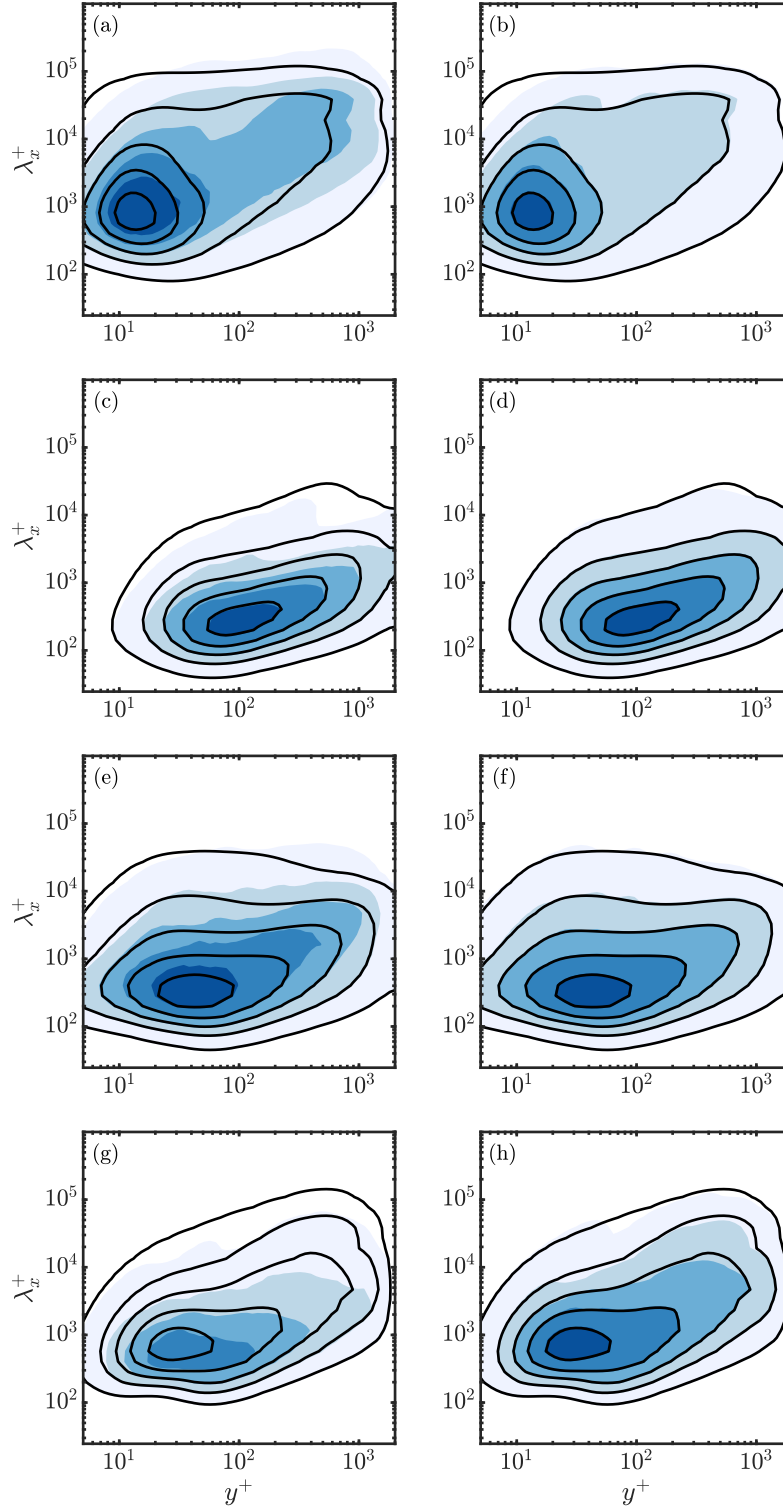


Figure 4.1: Premultiplied one-dimensional spectra from the resolvent (filled contours) and DNS (black contours) for $Re_\tau = 2003$. (a,c,e,g) Standard resolvent decomposition using $N = 6$ modes per wavenumber-frequency triplet; (b,d,f,h) OS-SQ resolvent decomposition using $N^{\text{OS}} = N^{\text{SQ}} = 3$ modes per wavenumber-frequency triplet. (a,b) $k_x E_{uu}$, (c,d) $k_x E_{vv}$, (e,f) $k_x E_{ww}$, (g,h) $-k_x E_{uv}$. Contour levels are from 10% to 90% of the DNS maximum in 20% increments.

(Hoyas and Jiménez, 2006). For the results shown in Figures 4.1 and 4.2, the resolvent representation was computed using $N = 6$ resolvent modes and $N_c = 100$ wavespeeds, about 0.01% of the degrees of freedom in the DNS.

Behavior at large λ_x

As discussed above, the most significant discrepancies between the DNS and OS-SQ representation of 1D the spectra shown in Figure 4.1 occur in $k_x E_{uu}$ at large λ_x^+ and $y^+ \lesssim 100$ and $-k_x E_{uv}$ at large λ_x^+ and $y^+ \gtrsim 30$. Furthermore, these errors do not improve considerably with an increasing number of modes, as demonstrated in Figure 4.3, which shows a slow decrease in the error for $N^{\text{OS}} = N^{\text{SQ}} = N > 4$.

The reason for the persisting error is that for large λ_x^+ , there is significant energetic content below the peaks of the lowest wavespeed modes, which typically sit around $y^+ \approx 40 - 50$ for $Re_\tau = 2003$ (Moarref et al., 2013b). Thus, trying to match near the wall results in overcompensation at larger y^+ . This is illustrated for the representative wavenumbers $(\lambda_x^+, \lambda_z^+) \approx (3.83 \times 10^4, 2.78 \times 10^3)$ in Figure 4.4. To confirm that this is indeed the cause, Figure 4.4 also shows the result of the optimization with $y_{\min}^+ = 50$, in which case the large oscillations disappear.

The near-wall errors eventually diminish as the number of modes tends to infinity. However, the fact that the spectra for these wavenumbers are not well-represented by a low-rank approximation suggests that the response modes may not be the most efficient basis. Indeed, Rosenberg et al. (2019) outline conditions under which the flowfields around a cylinder and for channel ECS are more compactly represented by the response to the forcing generated by the leading response at a different wavenumber triplet; it is possible that the present case is a similar situation, but the number of triadic interactions that would have to be accounted for in fully turbulent flow significantly complicates matters. It has also recently been shown that augmentation of Equation (4.4) with an eddy viscosity improves the representation of large-scale structures (Hwang, 2016; Illingworth et al., 2018; Madhusudanan et al., 2019). Both approaches attempt to constrain the forcing, the former by using triadic interactions to identify which scales are most important, and the latter by choosing to only directly model the large-scale coherent motions. However, as pointed out in ??, such nonlinear interactions are incompatible with the turbulent mean velocity profile when an eddy viscosity is included.

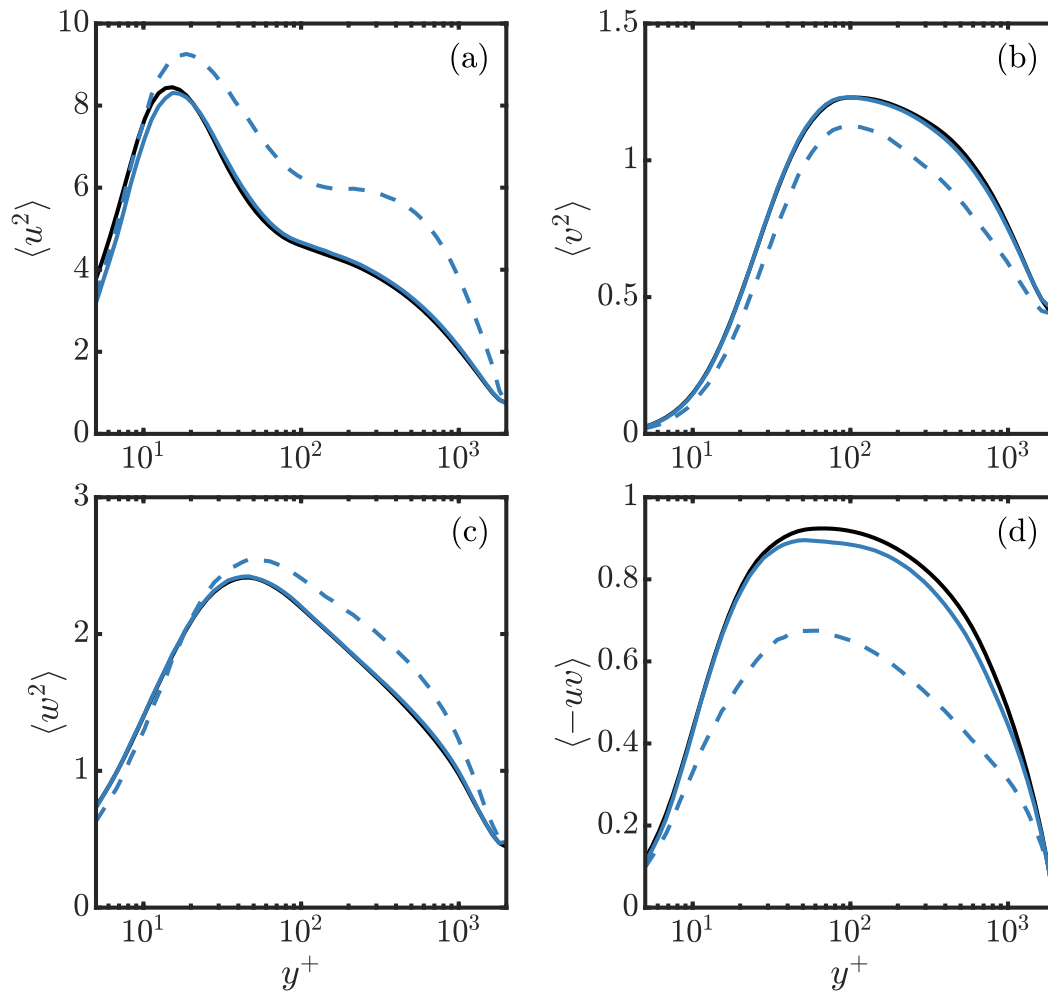


Figure 4.2: Intensities from the resolvent with $N^{\text{OS}} = N^{\text{SQ}} = 3$ modes per wavenumber-frequency triplet (blue) and DNS (black) for $Re_\tau = 2003$. Also shown in dashed lines are the intensities obtained from the standard resolvent decomposition approach using the same total number of modes.

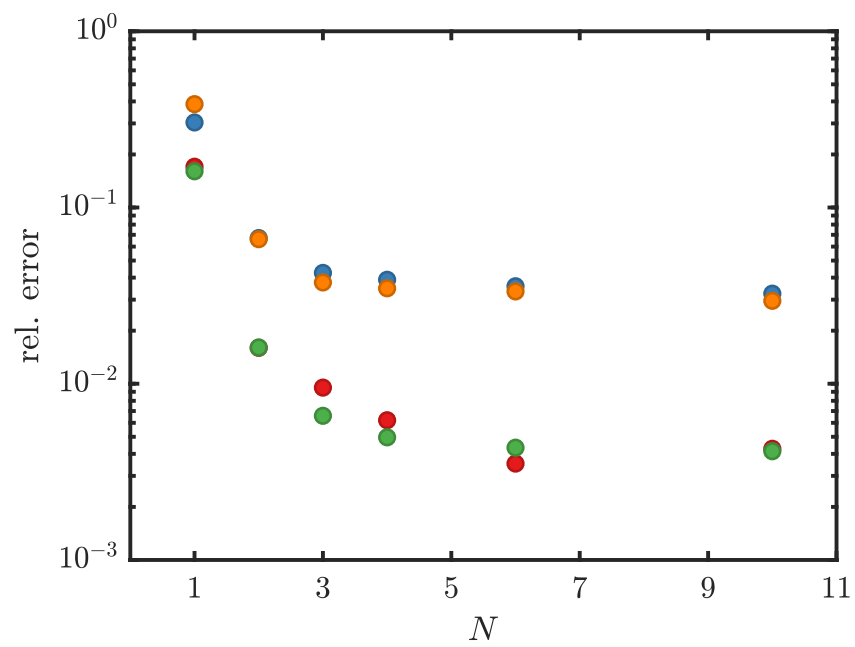


Figure 4.3: Relative errors in $\langle u^2 \rangle$ (blue), $\langle v^2 \rangle$ (red), $\langle w^2 \rangle$ (green), and $\langle -uv \rangle$ (orange), as a function of $N^{\text{OS}} = N^{\text{SQ}} = N$.

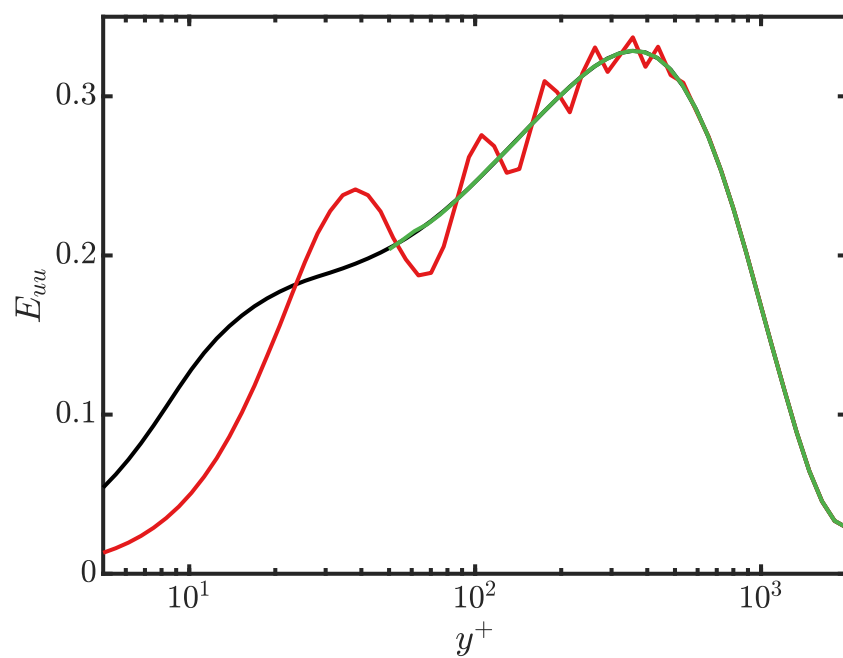


Figure 4.4: Comparison of DNS (black) and the optimization results with $y_{\min}^+ = 5$ (red) and $y_{\min}^+ = 50$ (green) using $N^{\text{OS}} = N^{\text{SQ}} = 6$ modes for $(\lambda_x^+, \lambda_z^+) \approx (3.83 \times 10^4, 2.78 \times 10^3)$.

Prediction of additional statistics

Since the optimization only attempts to match time-averaged spectra, the distribution of energetic content in c is not directly constrained. To assess this, the power spectra computed from the resolvent representation using the optimized weights with $N^{\text{OS}} = N^{\text{SQ}} = 3$ are compared to those computed from DNS for $Re_\tau = 185$ using Welch's method with 8491 snapshots divided into 10 segments having 50% overlap. Figure 4.5(a) and Figure 4.5(b) show the 2D premultiplied streamwise power spectra in the $k_x - \omega$ and $k_z - \omega$ planes, respectively, at $y^+ \approx 15$.

The distribution in the $k_x - \omega$ plane is fairly good, with most of the energetic content of the resolvent spectrum falling within the 10% DNS contour. As discussed above, the distribution in c is not directly constrained. However, the localization of the leading resolvent modes at the critical layer implies that the energetic content at a given wall-normal location is largely contributed by modes with a wavespeed matching the local mean velocity. This is evident in Figure 4.5, where both the DNS and resolvent spectra are concentrated around the dashed line representing the constant wavespeed equal to the mean velocity at $y^+ = 15$, i.e., $c = U(y^+ = 15)$. There is no such localization mechanism in the $k_z - \omega$ plane. Nonetheless, the resolvent representation still reproduces the general shape of the DNS spectrum quite well. Note that to produce Figure 4.5(b), the resolvent spectrum was interpolated onto a common ω grid prior to integration over k_x .

The optimized weights can also be used to compute an approximation of the forcing spectra in a manner that is directly analogous to the velocity spectra in Equation (4.14):

$$E_{g_v g_v}(y, k_x, k_z, c) = \text{Re} \left\{ \text{tr} \left(\mathbf{B}_{vv} \mathbf{X}^{\text{OS/OS}} \right) \right\}, \quad (4.21a)$$

$$E_{g_\eta g_\eta}(y, k_x, k_z, c) = \text{Re} \left\{ \text{tr} \left(\mathbf{B}_{\eta\eta} \mathbf{X}^{\text{SQ/SQ}} \right) \right\}, \quad (4.21b)$$

where $B_{vv,ij} = \phi_{v,i} \phi_{v,j}^*$, and $B_{\eta\eta,ij} = \phi_{\eta,i} \phi_{\eta,j}^*$. The estimates of the 2D forcing spectra with $N^{\text{OS}} = N^{\text{SQ}} = 3$ in the $k_x - k_z$ plane at $y^+ \approx 15$ for $Re_\tau = 185$ are compared to the full forcing spectra computed from DNS (Rosenberg, 2018) in Figure 4.6. The resolvent estimate reasonably predicts the general shape of the full spectra with only a few modes; this is consistent with results indicating that the OS-SQ decomposition yields not only an efficient response basis, but also a forcing basis that is more efficient than the one obtained from the standard resolvent approach (Rosenberg and McKeon, 2019b). Furthermore, this estimate was obtained using only information about the velocity statistics, an interesting implication of which is

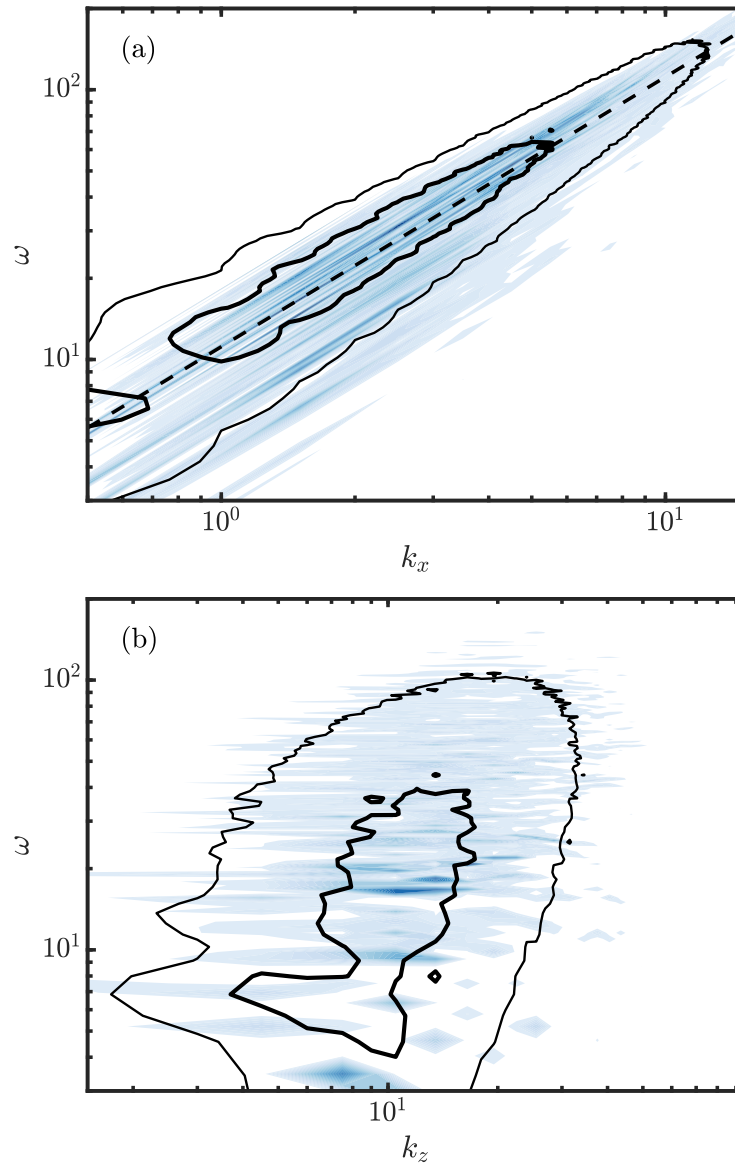


Figure 4.5: 2D premultiplied streamwise velocity power spectra at $y^+ \approx 15$ for $Re_\tau = 185$. (a) $\omega k_x E_{uu}$, (b) $\omega k_z E_{uu}$. Filled contours: Optimized weights with $N^{\text{OS}} = N^{\text{SQ}} = 3$. Line contours: DNS; levels are 10% (thin) and 50% (thick) of the maximum value. The slope of the dashed line indicates the the local mean velocity $U(y^+ = 15)$.

that potentially much can be learned about the nonlinear forcing directly from commonly-computed flow quantities. We note that similar observations have been made by Towne et al. (2020), who use a limited set of flow statistics to infer forcing statistics, which are in turn used to estimate the unknown flow statistics.

To give additional insight into how energetic modes are distributed across spectral space, the magnitudes of the total mode coefficients, i.e., the weight multiplied by the singular value, are plotted for the leading OS and SQ modes in Figure 4.7(a) and Figure 4.7(b), respectively, for $Re_\tau = 2003$; for ease of visualization, only coefficients larger than 1% of the maximum value over all spectral space are plotted. Interestingly, they are largely concentrated at large λ_x and c close to U_{cl} . In addition, there are large coefficients for very low c and large λ_x^+ , which are likely related to near-wall over-compensation, discussed in Section 4.2. This observed clustering may have implications for further model reduction by highlighting important regions of spectral space. Finally, with the exception of some SQ coefficients at small λ_x^+ and $c \approx U_{cl}$, the large OS and SQ coefficients occupy the essentially the same regions of spectral space which is a reflection of the interactions between the two families of modes; this is discussed in detail in the next section.

Finally, while Figure 4.7 appears to suggest that the longest modes should dominate the spectra, we remark that since modes with very large λ_x typically span the entire channel, the orthonormality constraint requires that their peak amplitudes be relatively low compared to other modes having more compact wall-normal support. Thus their contribution to the spectra at a given wall-normal location may be comparable to modes having smaller coefficients.

Interpretation of the OS-SQ decomposition: a competition mechanism

It has been demonstrated that the performance of the optimization is greatly improved by employing the OS-SQ decomposition of the resolvent. Previous work reported similar results for channel ECS (Rosenberg, 2018; Rosenberg and McKeon, 2019b). In that case, the relatively poor performance of the traditional resolvent method was attributed to the fact that the η response dominates under the kinetic energy norm. Thus, matching the statistics for u (or w) results in under-prediction of the v statistics, as observed in Figures 4.1 and 4.2. However, in the OS-SQ decomposition, isolating the v response in only the OS modes allows v and η , to be “tuned” somewhat independently, with the role of the SQ modes then being to saturate the OS vorticity. The improved matching of all components in Figure 4.2 indicates that this is also

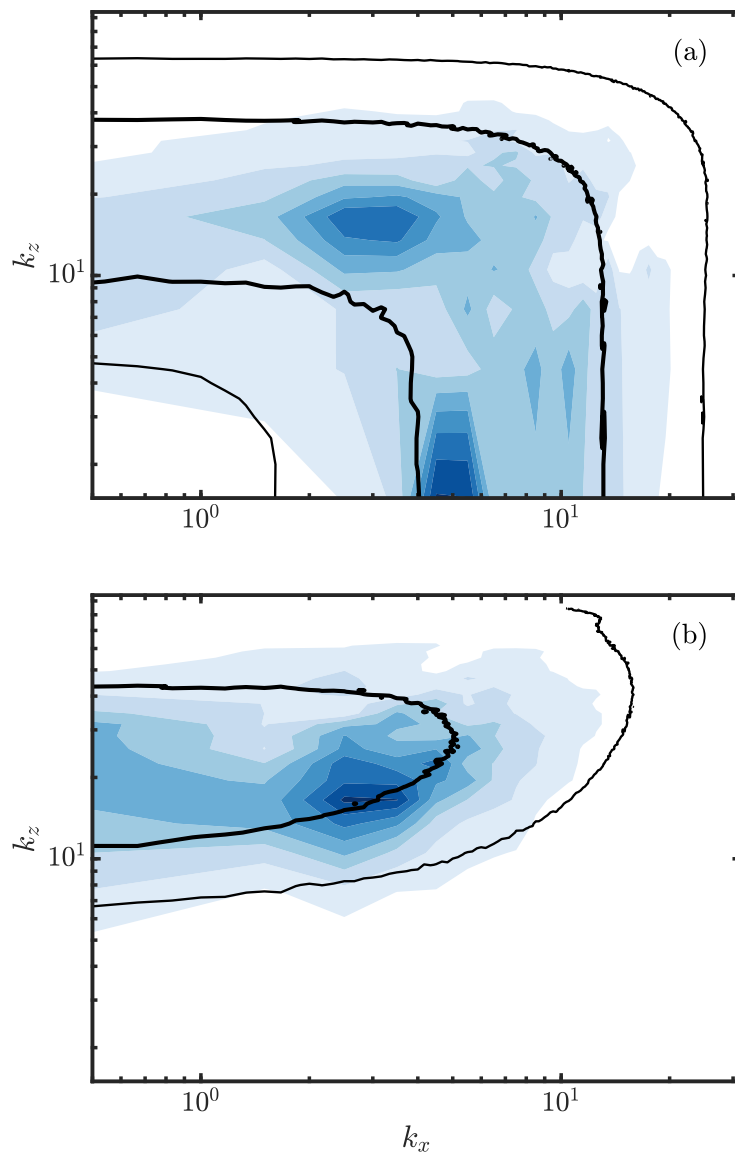


Figure 4.6: 2D forcing spectra at $y^+ \approx 15$ for $Re_\tau = 185$. (a) $E_{g_v g_v}$, (b) $E_{g_\eta g_\eta}$. Filled contours: Optimized weights with $N^{\text{OS}} = N^{\text{SQ}} = 3$. Line contours, reproduced from Rosenberg (2018): DNS; levels are 10% (thin) and 50% (thick) of the maximum value.

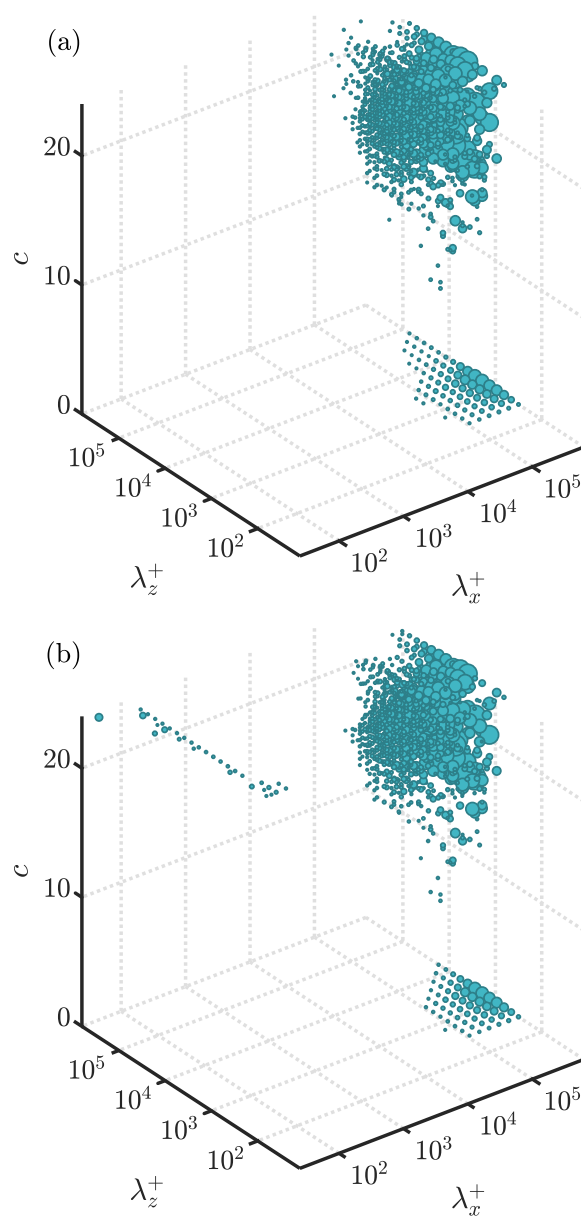


Figure 4.7: Magnitudes of the total leading mode coefficients (a) $\sigma_1^{\text{OS}} \sqrt{X_{11}^{\text{OS/OS}}}$, (b) $\sigma_1^{\text{SQ}} \sqrt{X_{11}^{\text{SQ/SQ}}}$ larger than 1% of the maximum value over all of spectral space for $Re_\tau = 2003$. Marker sizes are proportional to the magnitude and are normalized by the maximum. The axes show the full range of wave parameters included in the optimization.

the case for fully-turbulent channel flow, where the dynamics are significantly more complex than for the aforementioned equilibria.

To understand why the OS and SQ modes comprise a much more efficient basis, note that in certain cases the response modes of the standard resolvent, Equation (4.10), coincide with those of the OS resolvent, Equation (4.12a). A detailed description of the regions of parameter space where this holds is beyond the present scope, but we note that since $\mathcal{H}_{\eta v}$ contains the coupling term $-ik_z U'$, it is expected to hold whenever the lift-up mechanism is dominant, one such example being for highly streamwise-elongated modes. Further discussion can be found in Dawson and McKeon (2019). Here, we simply illustrate by example for a particular wavenumber-frequency triplet in Figure 4.8, which compares the singular values and magnitudes of the $\hat{\eta}$ response for the standard, OS, and SQ resolvents. Due to the symmetry of the channel geometry about $y = 0$, the resolvent yields symmetric-antisymmetric pairs of modes. If the modes are localized away from the centerline, then their singular values are equal; if, however, the modes have non-zero support at the centerline, then the singular values are not equal but are close in magnitude. The singular values of the OS and standard resolvents are almost equal, with the separation between them growing slowly with increasing mode index. Looking now at the $\hat{\eta}$ response modes, those from OS and standard resolvents are almost indistinguishable. Though not shown, the same is true for the \hat{v} responses.

The SQ singular values are significantly smaller than those for the standard or OS resolvent – by more than an order of magnitude for the first pair. Interestingly, the SQ singular values do not demonstrate clear pairing beyond this. The SQ $\hat{\eta}$ modes are distinct from the other two, in particular having slightly narrower wall-normal support. However, the shapes are still largely similar. Importantly, there is still a significant region of overlap with the OS modes in the wall-normal direction, which is a necessary condition for the SQ modes to interact with the OS modes.

It is also instructive to look at the corresponding forcing modes, which are shown in the top row of Figure 4.9. As with the response modes, ϕ_v for the OS and standard resolvents are virtually identical. This is at first surprising since the standard resolvent has ϕ_η with comparable amplitude to ϕ_v . However, its contribution to the norm is $\lesssim 1\%$. The bottom row of Figure 4.9 shows ϕ_η for the SQ and standard resolvents normalized by their maximum amplitude for ease of comparison. Despite some differences that become more pronounced for the higher-order modes, their shapes are overall quite similar. Therefore, though there may be traces of the SQ

modes in the leading standard resolvent modes, they are clearly dominated by the OS ones. This implies that using the standard resolvent operator to generate a low-order representation is effectively equivalent to using only the OS family of modes, and the linear mechanisms encoded in the SQ operator are thus not accounted for.

To further examine the relationship between the OS and SQ modes, we decompose the intensities shown in Figure 4.2 into contributions from OS modes only, SQ modes only, and a cross term (C) that represents the interaction of OS and SQ modes, e.g., $\langle u^2 \rangle$ becomes

$$\langle u^2 \rangle = \underbrace{\left\langle \left(u^{\text{OS}} \right)^2 \right\rangle}_{\text{OS}} + \underbrace{\left\langle \left(u^{\text{SQ}} \right)^2 \right\rangle}_{\text{SQ}} + \underbrace{2 \langle u^{\text{OS}} u^{\text{SQ}} \rangle}_{\text{C}}. \quad (4.22)$$

The individual terms with $N = 3$ for $\langle u^2 \rangle$, $\langle w^2 \rangle$, and $\langle -uv \rangle$ are shown in Figure 4.10, along with the totals (black curves). Note that the total $\langle u^2 \rangle$ profile appearing to be zero in Figure 4.10(a) is merely a result of the scale; it is identical to that plotted in Figure 4.2(a). The decomposition for $\langle v^2 \rangle$ is not shown since, as seen from Equation (4.12b), the SQ modes have no v response, and hence $\langle v^2 \rangle = \langle (v^{\text{OS}})^2 \rangle$. Similarly, there is no SQ-only contribution to $\langle -uv \rangle$. For $\langle u^2 \rangle$ and $\langle w^2 \rangle$, the OS and SQ terms are similar, with the OS term having slightly larger magnitude. However, for all three components, the C term is negative, which supports the claim that the SQ vorticity acts to saturate the OS vorticity. In fact, information about the phase relationship between the OS and SQ modes can be deduced from this observation. Note that the third term in Equation (4.22) is simply twice the covariance of u^{OS} and u^{SQ} . For simplicity, express each as a Fourier sine series in one variable:

$$u^{\text{OS}} = \sum_{i=1}^{\infty} A_i^{\text{OS}} \sin(k_i x + \theta_i^{\text{OS}}), \quad (4.23a)$$

$$u^{\text{SQ}} = \sum_{i=1}^{\infty} A_i^{\text{SQ}} \sin(k_i x + \theta_i^{\text{SQ}}), \quad (4.23b)$$

where A_i^{X} and θ_i^{X} are the amplitude and phase of the i th mode, respectively, and

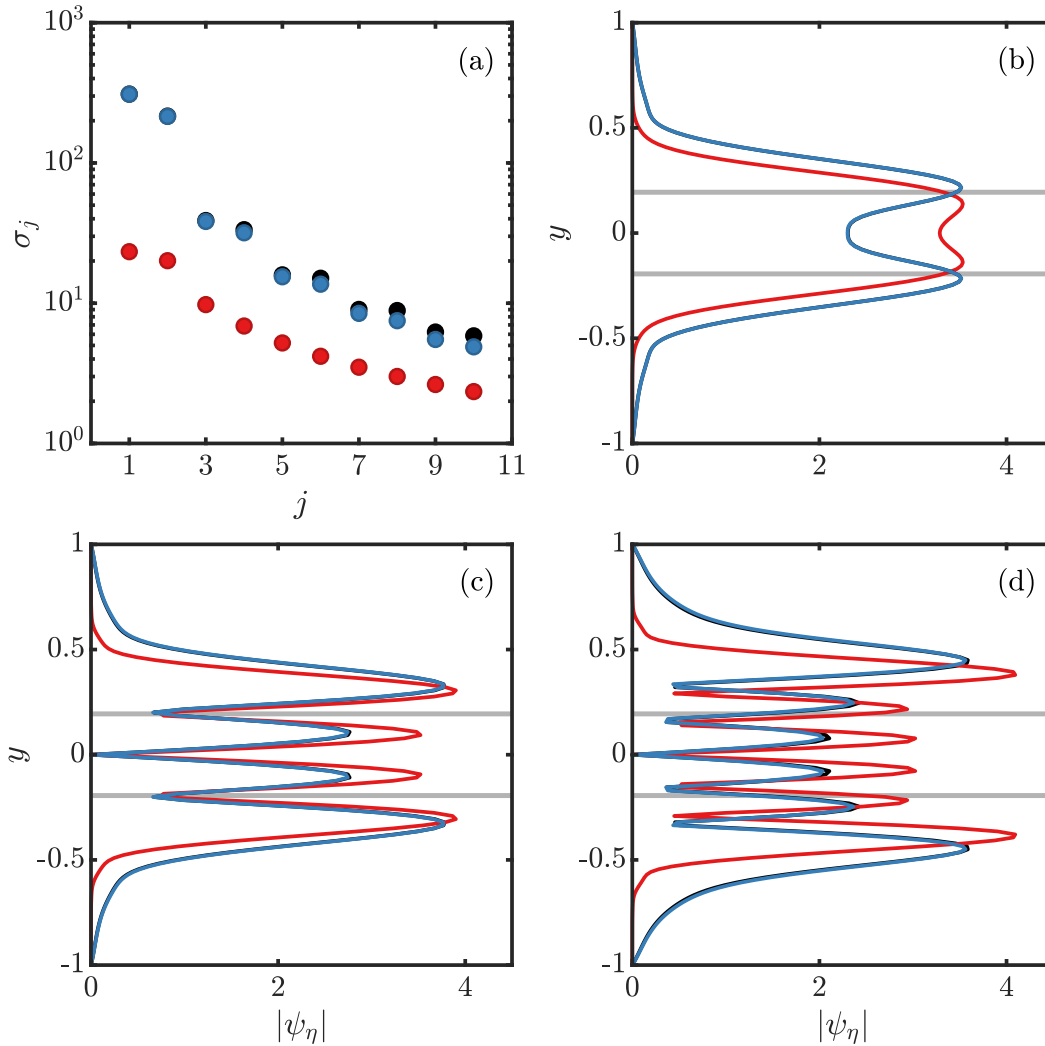


Figure 4.8: (a) First ten singular values of the OS (blue), SQ (red), and standard (black) resolvent operators for $(k_x, k_z, c) = (0.25, 2.5, 24)$ and $Re_\tau = 2003$. (b)-(d) Magnitudes of the vorticity responses from the first, second, and third mode pairs (same color scheme as in (a)); modes having the same wall-normal symmetry have been selected from each pair. The standard resolvent (black) and OS (blue) modes are visually indistinguishable. The gray lines in (b)-(d) are the locations of the critical layers, $y_c = \pm 0.194$.

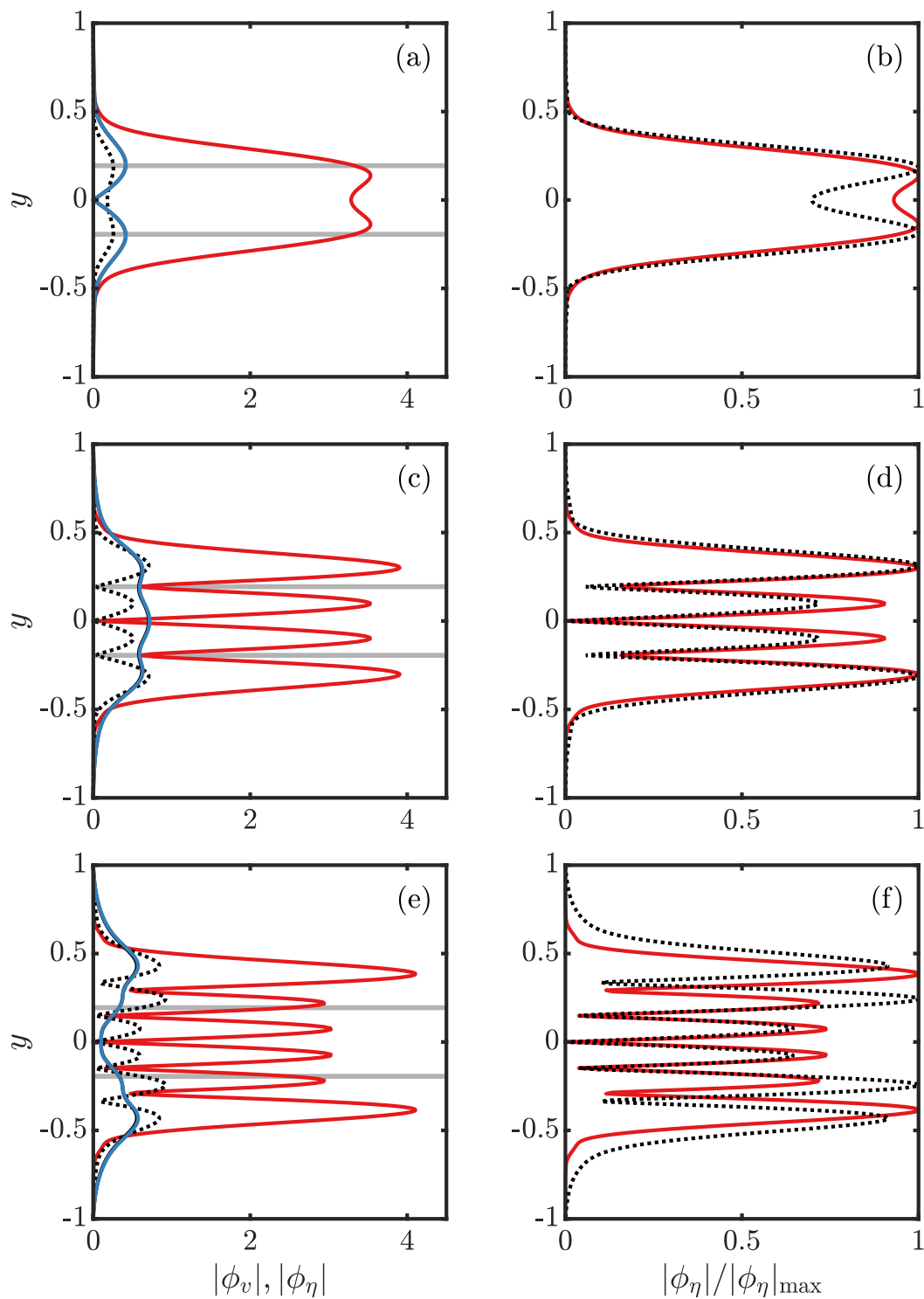


Figure 4.9: (a),(c),(e) Magnitudes of the forcing modes corresponding to the response modes shown in Figure 4.8, using the same color scheme. ϕ_v for the standard resolvent (solid black) is indistinguishable from OS (blue). Dotted lines are the standard resolvent ϕ_η . Gray lines are the locations of the critical layers, $y_c = \pm 0.194$. (b),(d),(f) SQ and standard resolvent ϕ_η normalized by their maximum values.

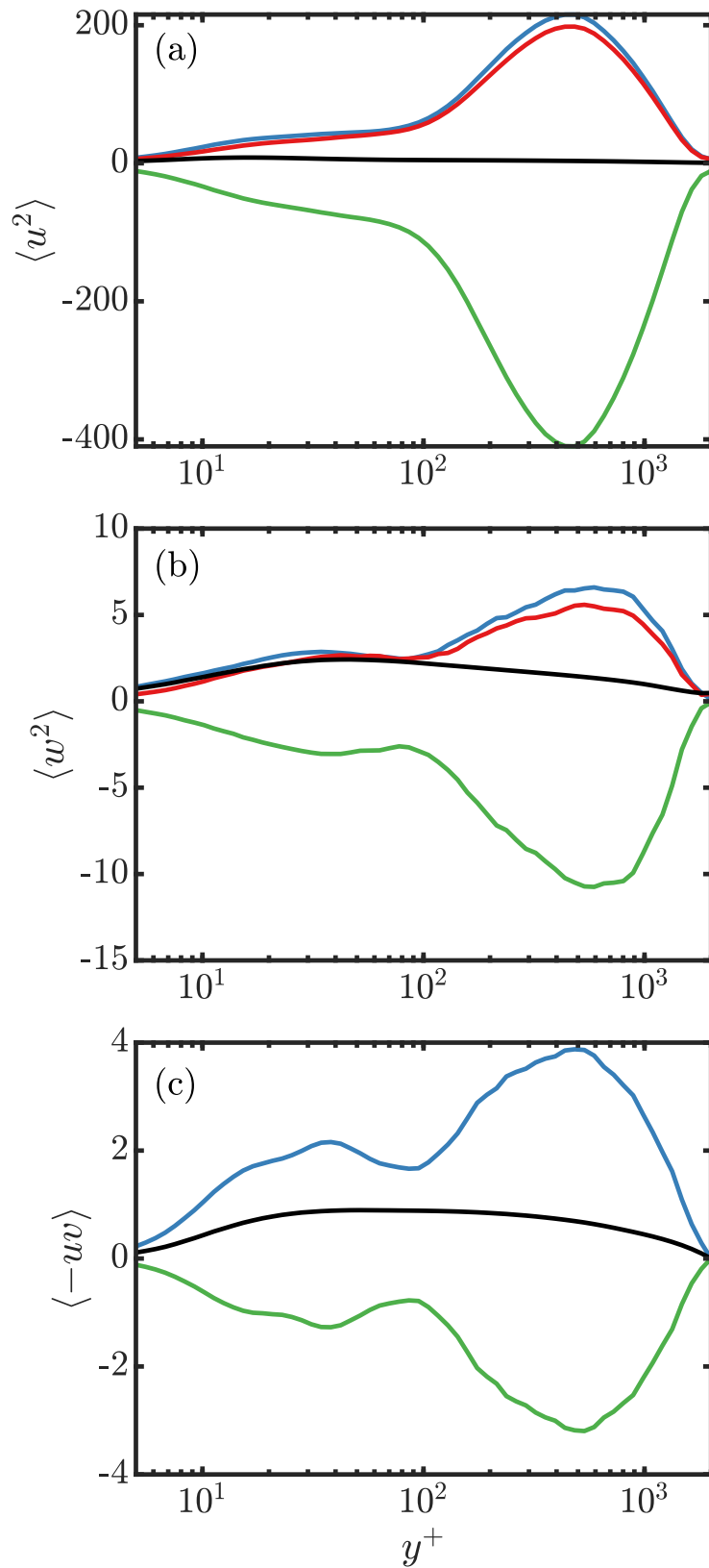


Figure 4.10: (a) $\langle u^2 \rangle$, (b) $\langle w^2 \rangle$, (c) $\langle -uv \rangle$ decomposed into OS (blue), SQ (red), and C (green) terms for $N = 3$. The totals are plotted in black.

$0 < k_1 < k_2 < \dots$. Then,

$$\begin{aligned}
2 \langle u^{\text{OS}} u^{\text{SQ}} \rangle &= 2 \sum_i \sum_j A_i^{\text{OS}} A_j^{\text{SQ}} \left\langle \sin(k_i x + \theta_i^{\text{OS}}) \sin(k_j x + \theta_j^{\text{SQ}}) \right\rangle \\
&= \sum_i \sum_j A_i^{\text{OS}} A_j^{\text{SQ}} \left(\left\langle \cos \left[(k_i - k_j)x + \theta_i^{\text{OS}} - \theta_j^{\text{SQ}} \right] \right\rangle \right. \\
&\quad \left. - \left\langle \cos \left[(k_i + k_j)x + \theta_i^{\text{OS}} + \theta_j^{\text{SQ}} \right] \right\rangle \right) \\
&= \sum_i A_i^{\text{OS}} A_i^{\text{SQ}} \cos(\Delta\theta_i),
\end{aligned} \tag{4.24}$$

where $\Delta\theta_i = \theta_i^{\text{OS}} - \theta_i^{\text{SQ}}$. The term labeled C in Equation (4.22) can thus be interpreted as a weighted (by the amplitudes) sum of the cosines of the phase difference between the OS and SQ modes. Therefore, $\langle u^{\text{OS}} u^{\text{SQ}} \rangle < 0$ implies $\pi/2 < |\Delta\theta_i| < 3\pi/2$ on average. Furthermore, the relative magnitudes of the three terms suggests that for the majority of modes the phase difference is relatively close to π , i.e., the OS and SQ modes are close to being exactly out of phase. Finally, we note that while the individual terms in Equation (4.22) depend on N , the trends discussed above, namely the similarity of the OS and SQ terms and the C term being negative, do not. Furthermore, performing the decomposition in Equation (4.22) for $\langle \eta^2 \rangle$ from $Re_\tau = 185$ DNS data reveals the same features (Rosenberg, 2018). This provides strong evidence that they are not merely consequences of the particular optimization procedure, but are in fact robust features of turbulent channel flow.

Since the SQ modes are exclusively wall-parallel motions, there is a passing resemblance to the notion of the “inactive” motions proposed by Townsend (1961). It is supposed that, at first order, the inactive motions do not interact with the “active” shear stress-carrying motions. However, Figure 4.10(c) shows that the interaction of the SQ vorticity with v produced by the OS modes, the C term, contributes significantly to the overall Reynolds shear stress profile, suggesting that there is not an exact correspondence between the SQ modes and inactive motions.

In this section, it was shown that the OS-SQ decomposition of the resolvent provides an improved basis for efficiently representing the statistics of turbulent channel flow, and that this provides insight into the complex physics at play, namely a competition mechanism, interpreted as a phase difference, between OS and SQ modes that results in saturation of the wall-normal vorticity. In the next section, we use this insight to derive simple scalings for the relative magnitudes of the OS and SQ weights of modes belonging to several special classes.

4.3 Weights scaling for the universal classes of resolvent modes

Moarref et al. (2013a) leveraged universal scaling regimes of the mean velocity profile to derive the Re_τ scaling for several universal classes of resolvent modes. Here, we extend this to the OS-SQ resolvent decomposition and show that for the outer and geometrically self-similar classes, each family of modes has a distinct scaling for the singular values. From this, the scalings of each submatrix of the energy density matrices \mathbf{A}_r given in Equation (4.17) can be determined. Combining these scalings with the hypothesis that competition of the OS and SQ modes remains relevant at different Reynolds numbers and in different regions of the flow enables the relative scaling of the OS and SQ weights belonging to the universal classes to be deduced.

The universal classes investigated here are the inner, outer, and geometrically self-similar classes. These consist of resolvent modes that are localized within the near-wall, wake, and logarithmic regions of the flow, respectively, and rely on universality of the mean velocity profile under the appropriate scaling in these regions. Figure 4.11(a) demonstrates the universality of U for $y^+ \lesssim 100$, and Figure 4.11(b) shows that the velocity defect $U_{cl} - U$ is universal for $y \gtrsim 0.1$; these approximate boundaries are indicated by the vertical dashed lines in Figure 4.11. Between these regions, there exists an intermediate region of the mean velocity profile in which both scalings hold. In this overlap region, it is widely accepted that the mean varies logarithmically with distance from the wall. Classical estimates put the beginning of the logarithmic region at $y^+ = O(100)$. However, there is recent evidence that this lower boundary moves outward as $Re_\tau^{1/2}$ (Klewicki et al., 2009; Marusic et al., 2013). In the logarithmic region, the resolvent operator admits self-similar modes localized about their critical layers (Moarref et al., 2013a). Furthermore, the scaling of these modes reduces to the inner and outer scalings when y^+ or y , respectively, is held fixed, reflecting their mutual validity in the logarithmic region.

In each of the next subsections, we briefly summarize the scaling of the wave parameters for each of the three aforementioned universal classes derived by Moarref et al. (2013a), as well as the distinct scalings for the OS and SQ singular values. Finally, the relative scaling of the OS and SQ weights are presented and tested against the computed optimal weights.

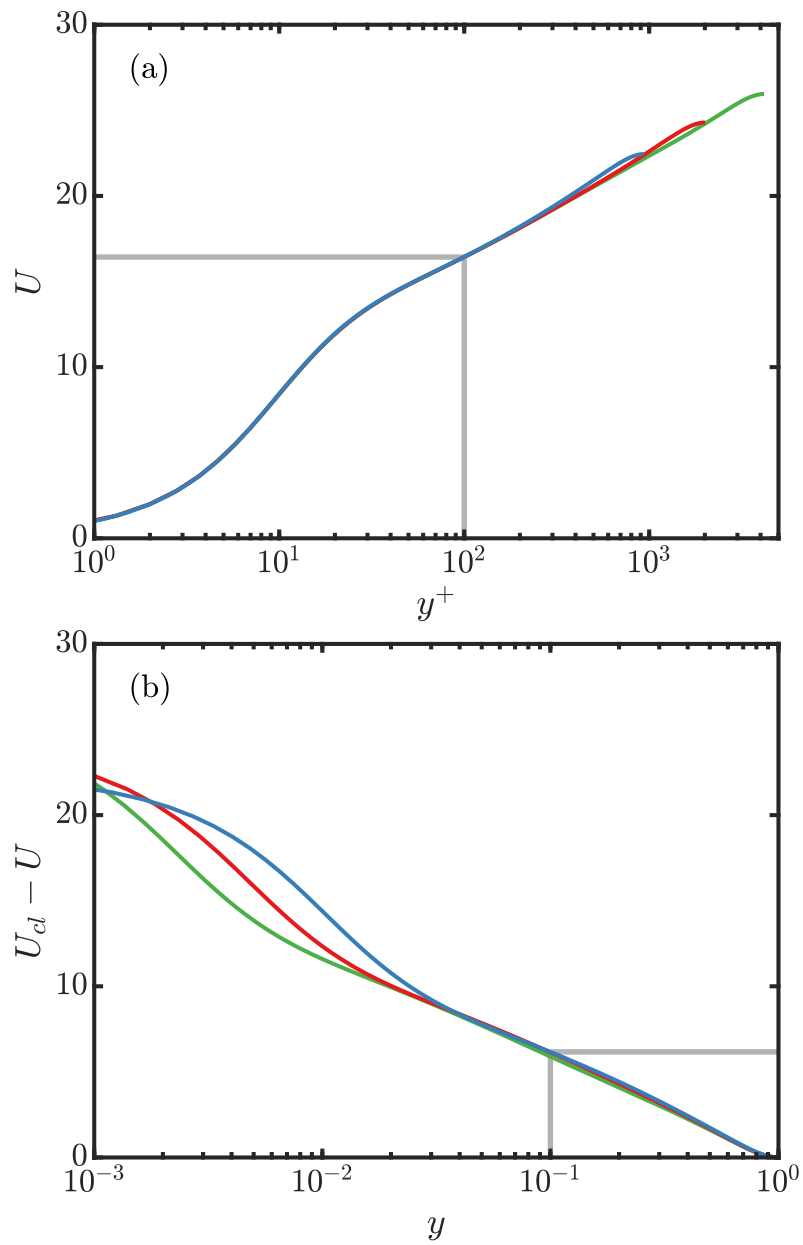


Figure 4.11: (a) Mean velocity profile $U(y^+)$ and (b) velocity defect $U_{cl} - U(y)$ for $Re_\tau = 934$ (blue), $Re_\tau = 2003$ (red), and $Re_\tau = 4219$ (green). The gray boxes indicate the regions where the profiles are Re_τ -invariant in the respective coordinates.

Inner class

Following Moarref et al. (2013a), the relevant length scale for the inner class is the viscous unit ν/u_τ , so that the corresponding inner-scaled parameters are

$$k_x^+ = Re_\tau^{-1} k_x, \quad k_z^+ = Re_\tau^{-1} k_z, \quad y^+ = Re_\tau y, \quad (4.25)$$

and the inner class wave parameters are

$$\mathcal{S}_i : \quad 0 \leq c \lesssim 16.4. \quad (4.26)$$

The upper wavespeed limit is obtained from the critical layer at the top of the inner region, i.e., $U(y^+ = 100) = 16.4$; this is indicated by the horizontal dashed line in Figure 4.11(a). Note that this bound is slightly different from the one given in Moarref et al. (2013a) since the mean velocity profiles they used were obtained from an eddy viscosity model, whereas the ones used here are taken directly from the DNS that the spectra are obtained from. Using Equation (4.25) and continuity, it follows that all three velocity components scale in the same way. Furthermore, the orthonormality constraint on the resolvent modes imposes

$$\hat{\mathbf{u}} = Re_\tau^{1/2} \hat{\mathbf{u}}^+, \quad (4.27)$$

where a superscript $(\cdot)^+$ indicates a quantity that is Re_τ -invariant for modes belonging to the inner class. Equation (4.25) can be used to obtain the inner-scaled versions of the weighted resolvent operators:

$$\begin{pmatrix} \mathcal{F}_v \mathcal{H}_{vv} \mathcal{F}_v^{-1} \\ \mathcal{F}_\eta \mathcal{H}_{\eta v} \mathcal{F}_v^{-1} \end{pmatrix} = Re_\tau^{-1} \begin{pmatrix} \mathcal{F}_v^+ \mathcal{H}_{vv}^+ \mathcal{F}_v^{+ -1} \\ \mathcal{F}_\eta^+ \mathcal{H}_{\eta v}^+ \mathcal{F}_v^{+ -1} \end{pmatrix} \quad (4.28a)$$

$$\mathcal{F}_\eta \mathcal{H}_{\eta\eta} \mathcal{F}_\eta^{-1} = Re_\tau^{-1} \mathcal{F}_\eta^+ \mathcal{H}_{\eta\eta}^+ \mathcal{F}_\eta^{+ -1}, \quad (4.28b)$$

where $\mathcal{F} = \text{diag}(\mathcal{F}_v, \mathcal{F}_\eta)$ is the square root of the positive-definite operator \mathcal{Q} defined in Equation (4.8), i.e., $\mathcal{Q} = \mathcal{F}^\dagger \mathcal{F}$, and the superscript $(\cdot)^\dagger$ denotes the adjoint with respect to the inner product Equation (4.7). Computing the SVDs of Equations (4.28a) and (4.28b), it is clear that both the OS and SQ singular values have the same scaling:

$$\sigma_j^{\text{OS}} = Re_\tau^{-1} \sigma_j^{\text{OS}+}, \quad \sigma_j^{\text{SQ}} = Re_\tau^{-1} \sigma_j^{\text{SQ}+}. \quad (4.29)$$

For a particular k_x^+ , k_z^+ , and $c \in \mathcal{S}_i$, the magnitudes of the leading vorticity response modes of the OS and SQ resolvent operators and their corresponding forcing modes for the three Re_τ in Figure 4.11 are shown in Figure 4.12(a) and Figure 4.12(b),

respectively, using the scalings derived in Equations (4.27)–(4.29). For comparison, the leading response and forcing mode for the standard resolvent operator are also shown; as discussed in Section 4.2, ψ_η and ϕ_v are indistinguishable from the OS modes.

Substituting Equations (4.27) and (4.29) into Equation (4.15), we obtain the inner-scaled energy density matrices:

$$\mathbf{A}_{r,ij}^{\text{OS/OS}} = Re_\tau^{-1} \mathbf{A}_{r,ij}^{\text{OS/OS}^+}, \quad \mathbf{A}_{r,ij}^{\text{OS/SQ}} = Re_\tau^{-1} \mathbf{A}_{r,ij}^{\text{OS/SQ}^+}, \quad \mathbf{A}_{r,ij}^{\text{SQ/SQ}} = Re_\tau^{-1} \mathbf{A}_{r,ij}^{\text{SQ/SQ}^+}. \quad (4.30)$$

With this, the decomposed version of the three-dimensional streamwise energy spectrum becomes

$$E_{uu} = Re_\tau^{-1} \text{Re} \left\{ \text{tr} \left(\mathbf{A}_{uu}^{\text{OS/OS}^+} \mathbf{X}^{\text{OS/OS}} \right) \right\} + 2Re_\tau^{-1} \text{Re} \left\{ \text{tr} \left(\mathbf{A}_{uu}^{\text{SQ/OS}^+} \mathbf{X}^{\text{OS/SQ}} \right) \right\} + Re_\tau^{-1} \text{Re} \left\{ \text{tr} \left(\mathbf{A}_{uu}^{\text{SQ/SQ}^+} \mathbf{X}^{\text{SQ/SQ}} \right) \right\}, \quad (4.31)$$

where the Reynolds number dependence of the right-hand side is made explicit, save for the unscaled weights matrices $\mathbf{X}^{\text{X/Y}}$. Equation (4.30) can be used to write similar expressions for the other components of the spectra.

Since the overall scaling of E_{uu} for the inner class is not known, the absolute scaling of the weights cannot be determined directly from Equation (4.31). However, in Section 4.2, it was shown that the vorticity generated by OS and SQ modes compete. That is, the vorticity generated by the SQ modes acts to “saturate” the OS vorticity. We hypothesize that this mechanism is not specific to $Re_\tau = 2003$ for which the optimization results were presented, but instead holds for arbitrary Re_τ . This is only possible if all three terms remain of the same order in Equation (4.31), which is satisfied if the inner class OS and SQ weights have the same scaling, i.e., if the ratio

$$\left| \frac{\chi_j^{\text{SQ}}}{\chi_j^{\text{OS}}} \right| \neq \text{fn}(Re_\tau) \quad (4.32)$$

for modes belonging to the universal inner class.

This scaling is tested by computing the weights matrices for the three Reynolds numbers depicted in Figure 4.11 for fixed inner-scaled wavenumber combinations (k_x^+ , k_z^+). As discussed in Section 4.1, the individual weights are not recovered from the full-rank solutions. However, $\mathbf{X}_{jj}^{\text{OS/OS}} \sim |\chi_j^{\text{OS}}|^2$ and $\mathbf{X}_{jj}^{\text{SQ/SQ}} \sim |\chi_j^{\text{SQ}}|^2$, so that $|\chi_j^{\text{SQ}}/\chi_j^{\text{OS}}| \sim \sqrt{\mathbf{X}_{jj}^{\text{SQ/SQ}}/\mathbf{X}_{jj}^{\text{OS/OS}}}$. This ratio with $j = 1$ is computed for the three Reynolds numbers, and the results for several wavenumber combinations spanning

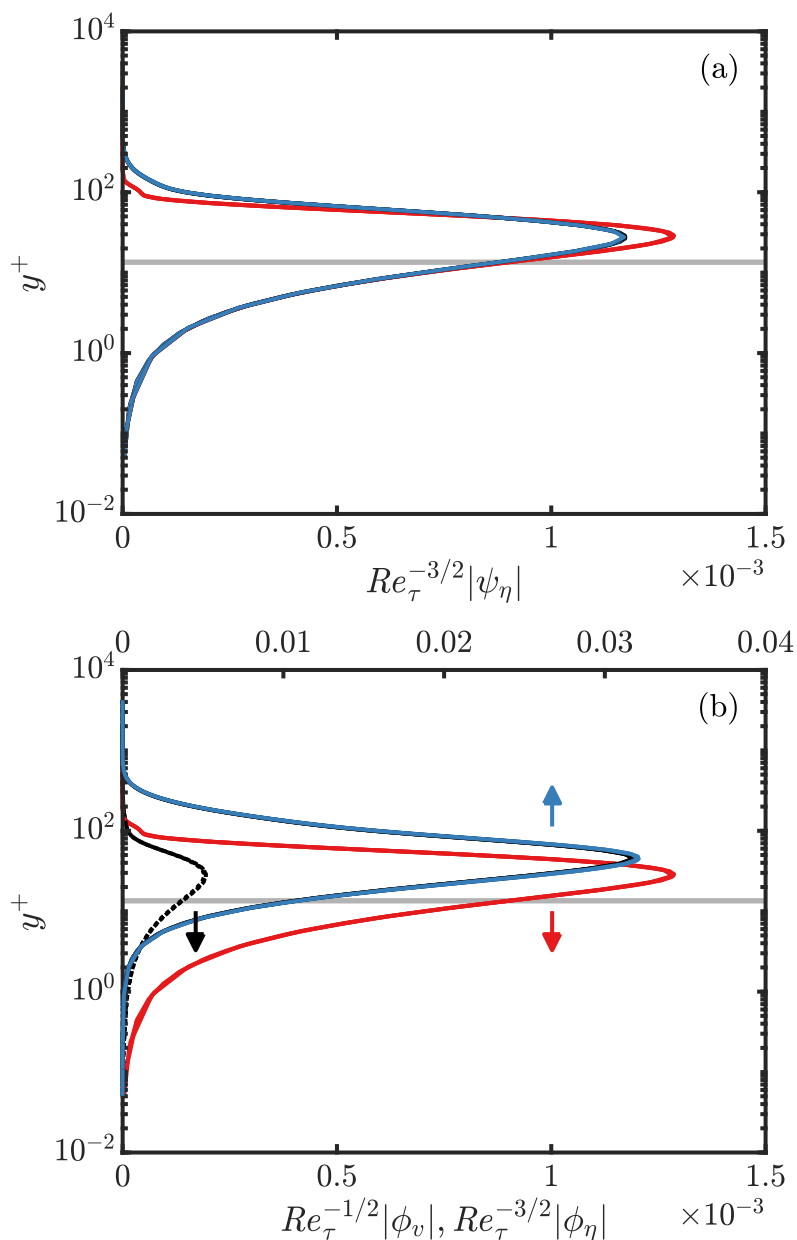


Figure 4.12: (a) Magnitudes of the scaled OS, SQ, and standard resolvent (color scheme as in Figure 4.8) inner-class leading vorticity response modes for the three Re_τ shown in Figure 4.11, with $k_x^+ = 1/934$, $k_z^+ = 10k_x^+$, and $c = 10$. (b) Corresponding scaled leading forcing mode magnitudes, with the relevant axes indicated by the arrows. ψ_η and ϕ_v for the standard resolvent are indistinguishable from the OS modes. The gray line indicates the location of the critical layer.

a large range of scales are shown in Figure 4.13. Overall, the agreement is quite good, showing a reasonable collapse despite some scatter. The main exception is for $(k_x^+, k_z^+) = (2\pi/10^3, 2\pi/10^2)$ in Figure 4.13(b), where there is clearly some dependence on Re_τ for $c \lesssim 10$. This trend is consistent for modes of relatively small scale ($k_x^+ \gtrsim O(2\pi/10^3)$) and large aspect ratio ($k_z^+/k_x^+ \gtrsim O(10)$). The reason for the failure of the scaling for these modes is unclear. However, it is observed that in such cases, the profiles of the time-averaged energy spectra are localized very near the wall. Additionally, the upper limit on the wavespeed range for inner class modes given in Equation (4.26), $c = 16.4$ is shown in each panel of Figure 4.13 as the vertical gray line. The fact that the scaling given by Equation (4.32) holds reasonably well for $c > 16.4$ is a reflection of the fact that the inner scaling remains valid in the logarithmic region, as seen in Fig. 4.11(a).

Outer class

The outer class length scales are

$$\tilde{k}_x = Re_\tau k_x, \quad \tilde{k}_z = k_z, \quad \tilde{y} = y, \quad (4.33)$$

and the outer class wave parameters are

$$\mathcal{S}_o : \begin{cases} 0 \leq U_{cl} - c \lesssim 6.17 \\ k_z/k_x \gtrsim \gamma Re_\tau / Re_{\tau, \min} \end{cases}, \quad (4.34)$$

where the upper bound on the wavespeed defect $U_{cl} - c = 6.17$ is obtained from the setting the minimum critical layer location at the bottom of the outer region, i.e., $U_{cl} - U(y = 0.1) = 6.17$; this is indicated by the horizontal dashed line in Figure 4.11(b). Again, this value is slightly different from the one given in Moarref et al. (2013a) due to the different source for the mean profiles. As Equation (4.34) indicates, the outer class modes must satisfy an aspect ratio constraint for all Re_τ considered, where the minimum aspect ratio is γ when $Re_\tau = Re_{\tau, \min}$ (Moarref et al., 2013a). Here, $Re_{\tau, \min} = 934$. From Equation (4.33) and continuity, it follows that

$$\hat{\mathbf{u}} = \begin{pmatrix} \tilde{u} \\ Re_\tau^{-1} \tilde{v} \\ Re_\tau^{-1} \tilde{w} \end{pmatrix}. \quad (4.35)$$

where $(\tilde{\cdot})$ indicates a quantity that is approximately Re_τ -invariant for modes belonging to the outer class. See also Sharma et al. (2017) and Moarref et al. (2014b) for the scaling of each velocity component, as well as for the components of the forcing modes.

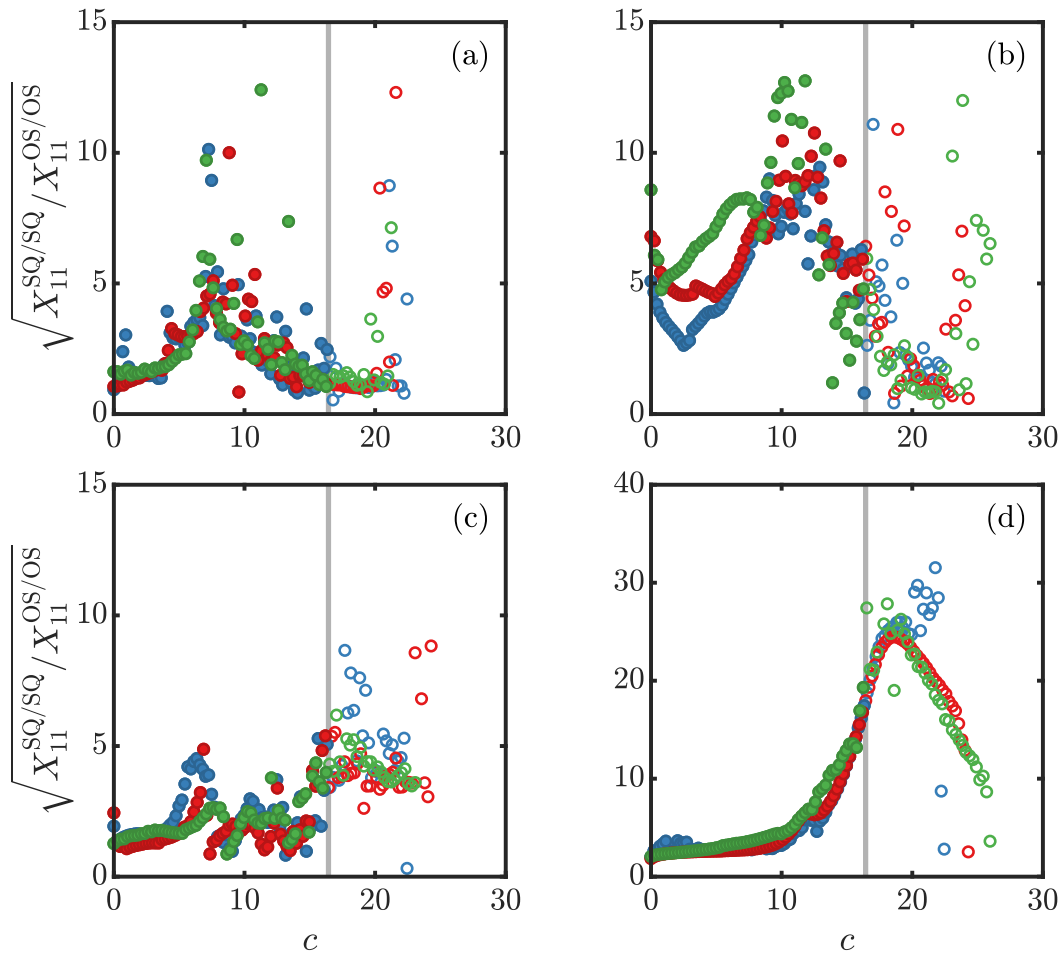


Figure 4.13: Leading weights ratio for $Re_\tau = 934$ (blue), $Re_\tau = 2003$ (red), and $Re_\tau = 4219$ (green) with $N = 3$ for several different wavelengths: (a) $(k_x^+, k_z^+) = (2\pi/10^2, 2\pi/10^2)$; (b) $(k_x^+, k_z^+) = (2\pi/10^3, 2\pi/10^2)$; (c) $(k_x^+, k_z^+) = (2\pi/10^3, 2\pi/10^3)$; (d) $(k_x^+, k_z^+) = (2\pi/10^4, 2\pi/10^3)$. Filled circles denote modes belonging to the universal inner class, and the highest inner class wavespeed, $c = 16.4$, is indicated by the gray line.

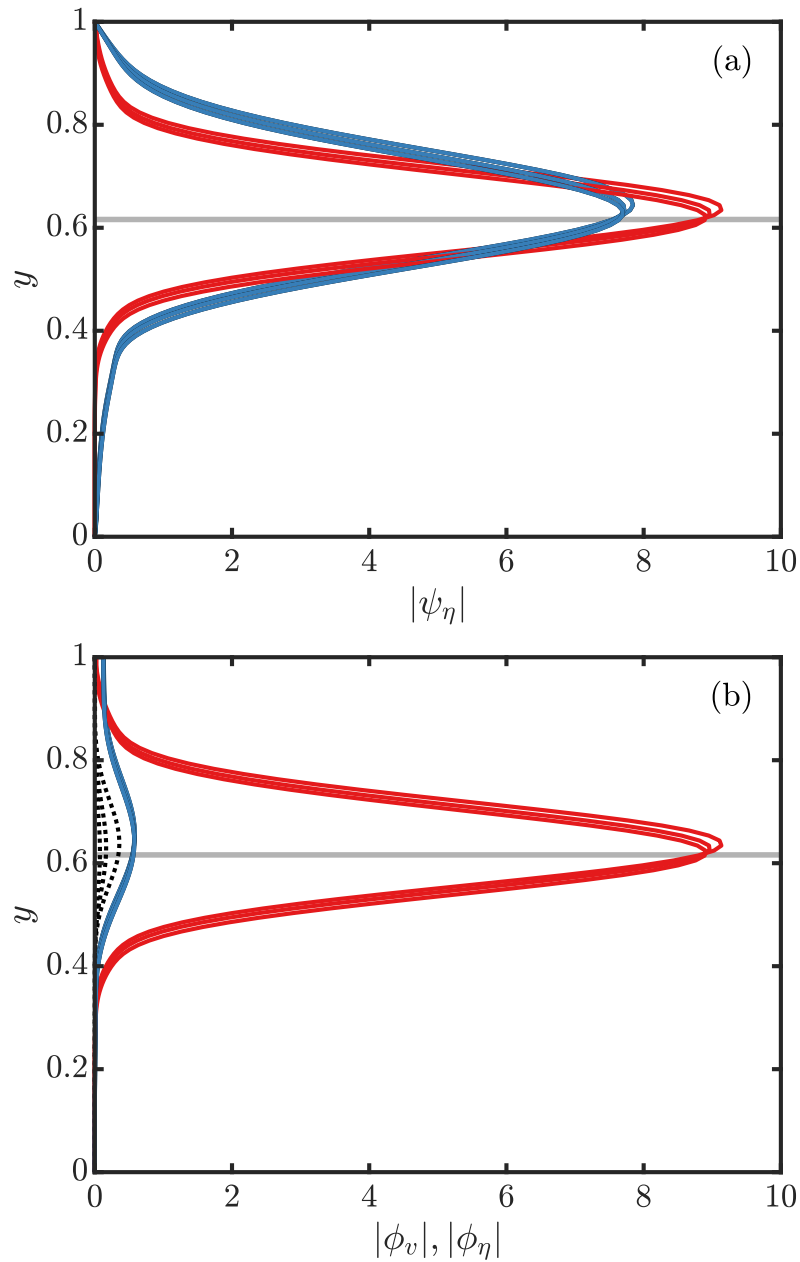


Figure 4.14: (a) Magnitudes of the scaled OS, SQ, and standard resolvent (color scheme as in Figure 4.8) outer-class leading vorticity response modes for the three Re_τ shown in Figure 4.11, with $\tilde{k}_x = 934$, $\tilde{k}_z = \gamma = 1.5\sqrt{10}$, and $U_{cl} - c = 1$. (b) Corresponding scaled leading forcing mode magnitudes. ψ_η and ϕ_v for the standard resolvent are indistinguishable from the OS modes. The gray line indicates the location of the critical layer.

The outer-scaled versions of the weighted resolvent operators are

$$\begin{pmatrix} \mathcal{F}_v \mathcal{H}_{vv} \mathcal{F}_v^{-1} \\ \mathcal{F}_\eta \mathcal{H}_{\eta v} \mathcal{F}_v^{-1} \end{pmatrix} = \begin{pmatrix} Re_\tau \tilde{\mathcal{F}}_v \tilde{\mathcal{H}}_{vv} \tilde{\mathcal{F}}_v^{-1} \\ Re_\tau^2 \tilde{\mathcal{F}}_\eta \tilde{\mathcal{H}}_{\eta v} \tilde{\mathcal{F}}_v^{-1} \end{pmatrix} \quad (4.36a)$$

$$\mathcal{F}_\eta \mathcal{H}_{\eta\eta} \mathcal{F}_\eta^{-1} = Re_\tau \tilde{\mathcal{F}}_\eta \tilde{\mathcal{H}}_{\eta\eta} \tilde{\mathcal{F}}_\eta^{-1}. \quad (4.36b)$$

Computing the SVDs of Equations (4.36a) and (4.36b), we have for the leading singular values,

$$\sigma_j^{\text{OS}} = Re_\tau^2 \tilde{\sigma}_j^{\text{OS}}, \quad \sigma_j^{\text{SQ}} = Re_\tau \tilde{\sigma}_j^{\text{SQ}}. \quad (4.37)$$

Note that because the components of Equation (4.36a) do not scale uniformly for outer-class modes, the scaling of the OS singular values is only expected to hold for the first several modes. However, since good agreement between the resolvent and DNS spectra is achieved using only a small number of modes, it is reasonable to adopt the scalings in what follows.

For a particular $(k_x, k_z, c) \in \mathcal{S}_o$, the magnitudes of the leading vorticity response modes of the OS and SQ resolvent operators and their corresponding forcing modes for the three Re_τ in Figure 4.11 are shown in Figure 4.14(a) and Figure 4.14(b), respectively, using the scalings derived in Equations (4.35)–(4.37). For comparison, the leading response and forcing mode for the standard resolvent operator are also shown; again, ψ_η and ϕ_v are indistinguishable from the OS modes. Apparent from Figure 4.14 is that the scaling of the outer class modes is only approximate. Recalling that the derivation of such universal classes relies on universal behavior of the mean profile, this is not surprising, since it is clear from Figure 4.11(b) that the mean profiles for the three Re_τ do not collapse perfectly for $y > 0.1$. Additionally, ϕ_η for the standard resolvent (black dotted line in Figure 4.14(b)) does not obey the same scaling as ϕ_η^{SQ} . Indeed, using the scaling of the standard resolvent in primitive variables presented in Sharma et al. (2017), it can be shown that $\phi_\eta = O(Re_\tau^{-1})$.

Substituting Equations (4.35) and (4.37) into Equation (4.15), we obtain the outer-scaled energy density matrices:

$$A_{uu,ij}^{\text{OS/OS}} = Re_\tau^4 \tilde{A}_{uu,ij}^{\text{OS/OS}}, \quad A_{uu,ij}^{\text{OS/SQ}} = Re_\tau^3 \tilde{A}_{uu,ij}^{\text{OS/SQ}}, \quad A_{uu,ij}^{\text{SQ/SQ}} = Re_\tau^2 \tilde{A}_{uu,ij}^{\text{SQ/SQ}}, \quad (4.38a)$$

$$A_{vv,ij}^{\text{OS/OS}} = Re_\tau^2 \tilde{A}_{vv,ij}^{\text{OS/OS}}, \quad (4.38b)$$

$$A_{ww,ij}^{\text{OS/OS}} = Re_\tau^2 \tilde{A}_{ww,ij}^{\text{OS/OS}}, \quad A_{ww,ij}^{\text{OS/SQ}} = Re_\tau \tilde{A}_{ww,ij}^{\text{OS/SQ}}, \quad A_{ww,ij}^{\text{SQ/SQ}} = \tilde{A}_{ww,ij}^{\text{SQ/SQ}}, \quad (4.38c)$$

$$A_{uv,ij}^{\text{OS/OS}} = Re_\tau^3 \tilde{A}_{uv,ij}^{\text{OS/OS}}, \quad A_{uv,ij}^{\text{OS/SQ}} = Re_\tau^2 \tilde{A}_{uv,ij}^{\text{OS/SQ}}. \quad (4.38d)$$

The streamwise energy spectrum is thus

$$E_{uu} = Re_\tau^4 \operatorname{Re} \left\{ \operatorname{tr} \left(\tilde{\mathbf{A}}_{uu}^{\text{OS/OS}} \mathbf{X}^{\text{OS/OS}} \right) \right\} + 2Re_\tau^3 \operatorname{Re} \left\{ \operatorname{tr} \left(\tilde{\mathbf{A}}_{uu}^{\text{SQ/OS}} \mathbf{X}^{\text{OS/SQ}} \right) \right\} + Re_\tau^2 \operatorname{Re} \left\{ \operatorname{tr} \left(\tilde{\mathbf{A}}_{uu}^{\text{SQ/SQ}} \mathbf{X}^{\text{SQ/SQ}} \right) \right\}, \quad (4.39)$$

where again the Reynolds number dependence of the right-hand side is explicit, save for the unscaled weights matrices $\mathbf{X}^{\text{X/Y}}$, and Equation (4.38) can be used to write similar expressions for the other energy spectra.

As for the inner class modes, competition between the OS and SQ modes requires that all three terms are of the same order for arbitrary Re_τ , which is satisfied if

$$\left| \frac{\chi_j^{\text{SQ}}}{\chi_j^{\text{OS}}} \right| \sim Re_\tau \quad (4.40)$$

for modes belonging to the universal outer class.

The weights ratio $\sqrt{\chi_{11}^{\text{SQ/SQ}}/\chi_{11}^{\text{OS/OS}}}$ for the three Reynolds numbers is shown in the top row of Figure 4.15 for several values of the outer-scaled wavenumber combinations $(\tilde{k}_x, \tilde{k}_x)$ and a minimum aspect ratio $\gamma = \sqrt{10}$. In agreement with Equation (4.40), the data from all three Reynolds numbers show reasonable collapse onto a single curve for $U_{cl} - c \lesssim 6.17$ when scaled by Re_τ^{-1} , as seen in the bottom row of Figure 4.15.

Geometrically self-similar class

The self-similar resolvent modes in the logarithmic region of the mean velocity profile belong to hierarchies parameterized by the critical layer location y_c (Moarref et al., 2013a). The corresponding length scales along a hierarchy are

$$\check{k}_x = y_c^+ y_c k_x, \quad \check{k}_z = y_c k_z, \quad \check{y} = y/y_c, \quad (4.41)$$

and the self-similar class wave parameters are

$$\mathcal{S}_h : \begin{cases} 16.4 \lesssim c \lesssim U_{cl} - 6.17 \\ c = U(y_c^+) = \kappa^{-1} \log y_c^+ + B \\ k_z/k_x \gtrsim \gamma \end{cases}, \quad (4.42)$$

where κ is the Kármán constant. Note that the lower wavespeed bound for the self-similar class, $c = 16.4$, is the same as the upper limit for the inner class modes, i.e., the beginning of the logarithmic region is taken to be $y^+ = 100$. As discussed above, recent evidence suggests that this lower limit is Re_τ -dependent

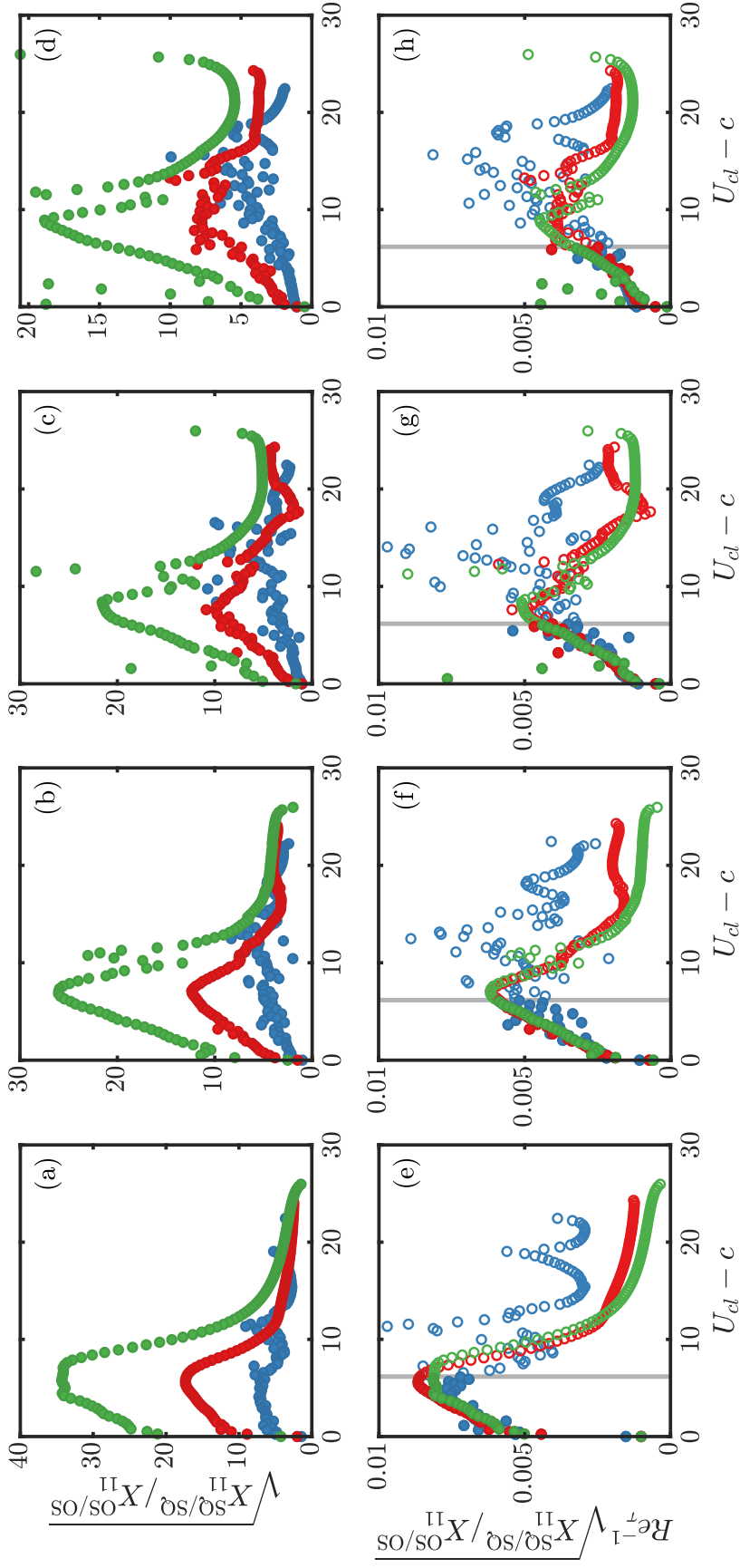


Figure 4.15: (a)-(d) Leading weights for $Re_\tau = 934$ (blue), $Re_\tau = 2003$ (red), and $Re_\tau = 4219$ (green) with $N = 2$. (e)-(h) Weights ratio scaled according to Equation (4.40). Each column represents a different scaled streamwise wavenumber \tilde{k}_x : (a),(e) $\tilde{k}_x = 4219$; (b),(f) $\tilde{k}_x = 8438$; (c),(g) $\tilde{k}_x = 12657$; (d),(h) $\tilde{k}_x = 16876$. In all cases the spanwise wavenumber is $k_z = \gamma \tilde{k}_x / Re_{\tau, \min}$, with $\gamma = \sqrt{10}$. Filled circles denote modes belonging to the universal outer class, and the largest outer class wavenumber defect, $U_{cl} - c = 6.17$, is indicated by the gray line.

(Klewicki et al., 2009; Marusic et al., 2013). However, Moarref et al. (2013a) demonstrated successful scaling of the self-similar modes using the fixed lower limit in Equation (4.42), so we continue to use it here. For reference, the beginning of the logarithmic region according to the balance of terms in the mean momentum equation, $y^+ \approx 2.6Re_\tau^{1/2}$ (Klewicki et al., 2009), is indicated by the gray dashed line in Figure 4.17. The self-similar modes must also satisfy an aspect ratio constraint. Since the aspect ratio increases like y_c^+ along a given hierarchy, it is sufficient that the lowest member on the hierarchy with critical layer $y_{c,l}$ and wavenumbers $k_{x,l}, k_{z,l}$ satisfies $k_{z,l}/k_{x,l} \gtrsim \gamma$, where a conservative lower bound is $\gamma \approx \sqrt{10}$ (Moarref et al., 2013a).

Using Equation (4.41) and continuity, as well as the orthonormality constraint on the resolvent modes, it follows that

$$\hat{\mathbf{u}} = y_c^{-1/2} \begin{pmatrix} \check{u} \\ y_c^{+1} \check{v} \\ y_c^{+1} \check{w} \end{pmatrix}. \quad (4.43)$$

where $(\check{\cdot})$ indicates a quantity that is approximately y_c - and Re_τ -invariant for modes belonging to the self-similar class. The y_c -scaled versions of the weighted resolvent operators are

$$\begin{pmatrix} \mathcal{F}_v \mathcal{H}_{vv} \mathcal{F}_v^{-1} \\ \mathcal{F}_\eta \mathcal{H}_{\eta v} \mathcal{F}_v^{-1} \end{pmatrix} = \begin{pmatrix} y_c y_c^+ \check{\mathcal{F}}_v \check{\mathcal{H}}_{vv} \check{\mathcal{F}}_v^{-1} \\ y_c y_c^+ \check{\mathcal{F}}_\eta \check{\mathcal{H}}_{\eta v} \check{\mathcal{F}}_v^{-1} \end{pmatrix} \quad (4.44a)$$

$$\mathcal{F}_\eta \mathcal{H}_{\eta\eta} \mathcal{F}_\eta^{-1} = y_c y_c^+ \check{\mathcal{F}}_\eta \check{\mathcal{H}}_{\eta\eta} \check{\mathcal{F}}_\eta^{-1}, \quad (4.44b)$$

so that their leading singular values scale as

$$\sigma_j^{\text{OS}} = y_c y_c^+ \check{\sigma}_j^{\text{OS}}, \quad \sigma_j^{\text{SQ}} = y_c y_c^+ \check{\sigma}_j^{\text{SQ}}. \quad (4.45)$$

As with the outer class modes, the scaling of the OS singular values are only expected to hold for the first several modes.

The magnitudes of the leading vorticity response modes of the OS and SQ resolvent operators and their corresponding forcing modes for five members of a particular hierarchy at $Re_\tau = 2003$ are shown in Figure 4.16(a) and Figure 4.16(b), respectively, using the scalings derived in Equations (4.43)–(4.45). For comparison, the leading response and forcing mode for the standard resolvent operator are also shown; again, ψ_η and ϕ_v are indistinguishable from the OS modes. Here again, ϕ_η for the standard

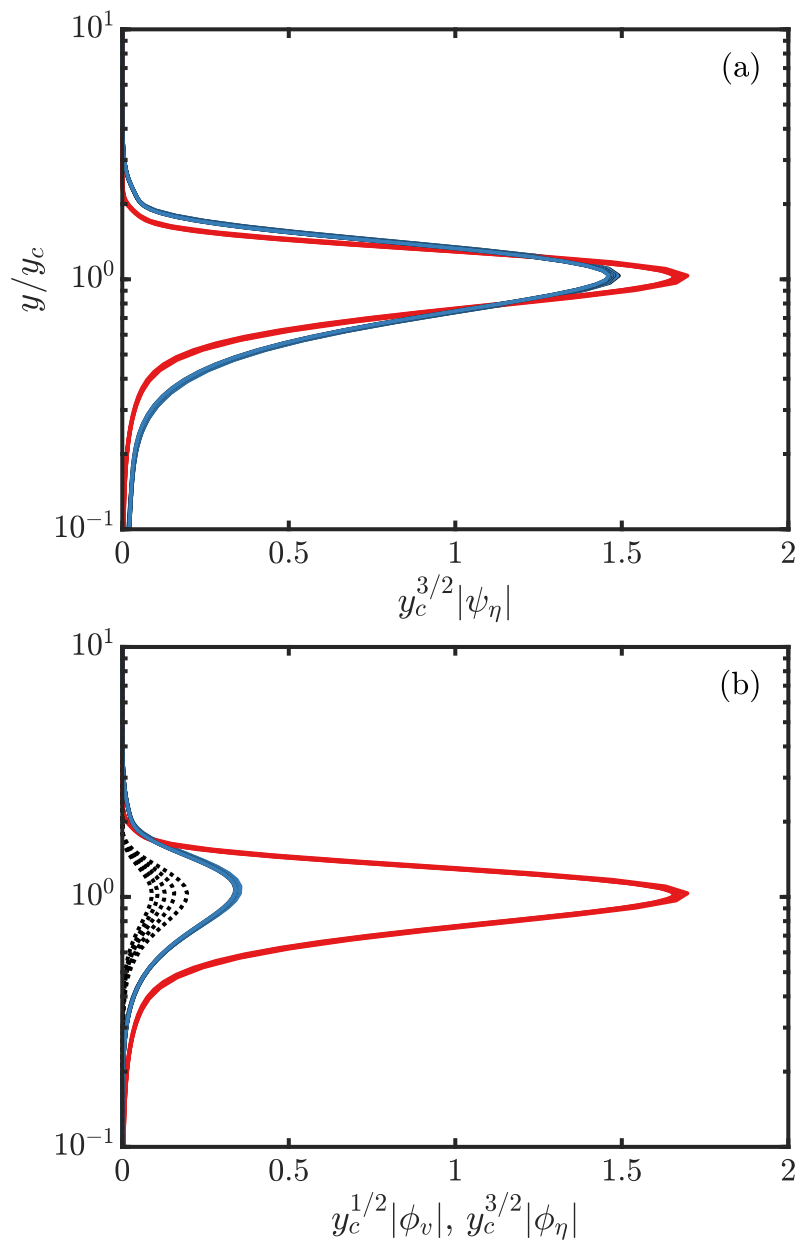


Figure 4.16: (a) Magnitudes of the scaled OS, SQ, and standard resolvent (color scheme as in Figure 4.8) self-similar leading vorticity response modes for five members of a hierarchy at $Re_\tau = 2003$, with $k_{x,l} = 10$ and $k_{z,l} = 10^{3/2}$. (b) Corresponding scaled leading forcing mode magnitudes. ψ_η and ϕ_v for the standard resolvent (black) are indistinguishable from the OS modes (blue).

resolvent (black dotted line in Figure 4.16(b)) and ϕ_η^{SQ} exhibit different scalings, with the standard resolvent $\phi_\eta = O(y_c^{-3/2} y_c^+^{-1})$.

Substituting Equations (4.43) and (4.45) into Equation (4.15), we obtain the scaled energy density matrices:

$$\mathbf{A}_{uu,ij}^{\text{OS/OS}} = y_c y_c^+{}^4 \check{\mathbf{A}}_{uu,ij}^{\text{OS/OS}}, \quad \mathbf{A}_{uu,ij}^{\text{OS/SQ}} = y_c y_c^+{}^3 \check{\mathbf{A}}_{uu,ij}^{\text{OS/SQ}}, \quad \mathbf{A}_{uu,ij}^{\text{SQ/SQ}} = y_c y_c^+{}^2 \check{\mathbf{A}}_{uu,ij}^{\text{SQ/SQ}}, \quad (4.46a)$$

$$\mathbf{A}_{vv,ij}^{\text{OS/OS}} = y_c y_c^+{}^2 \check{\mathbf{A}}_{vv,ij}^{\text{OS/OS}}, \quad (4.46b)$$

$$\mathbf{A}_{ww,ij}^{\text{OS/OS}} = y_c y_c^+{}^2 \check{\mathbf{A}}_{ww,ij}^{\text{OS/OS}}, \quad \mathbf{A}_{ww,ij}^{\text{OS/SQ}} = y_c y_c^+ \check{\mathbf{A}}_{ww,ij}^{\text{OS/SQ}}, \quad \mathbf{A}_{ww,ij}^{\text{SQ/SQ}} = y_c \check{\mathbf{A}}_{ww,ij}^{\text{SQ/SQ}}, \quad (4.46c)$$

$$\mathbf{A}_{uv,ij}^{\text{OS/OS}} = y_c y_c^+{}^3 \check{\mathbf{A}}_{uv,ij}^{\text{OS/OS}}, \quad \mathbf{A}_{uv,ij}^{\text{OS/SQ}} = y_c y_c^+{}^2 \check{\mathbf{A}}_{uv,ij}^{\text{OS/SQ}}, \quad (4.46d)$$

and the streamwise energy spectrum is

$$E_{uu} = y_c y_c^+{}^4 \text{Re} \left\{ \text{tr} \left(\check{\mathbf{A}}_{uu}^{\text{OS/OS}} \mathbf{X}^{\text{OS/OS}} \right) \right\} + 2 y_c y_c^+{}^3 \text{Re} \left\{ \text{tr} \left(\check{\mathbf{A}}_{uu}^{\text{SQ/OS}} \mathbf{X}^{\text{OS/SQ}} \right) \right\} + y_c y_c^+{}^2 \text{Re} \left\{ \text{tr} \left(\check{\mathbf{A}}_{uu}^{\text{SQ/SQ}} \mathbf{X}^{\text{SQ/SQ}} \right) \right\}, \quad (4.47)$$

where the y_c dependence of the right-hand side is explicit, except for the unscaled weights matrices $\mathbf{X}^{\text{X/Y}}$. Balancing all three terms requires

$$\left| \frac{\chi_j^{\text{SQ}}}{\chi_j^{\text{OS}}} \right| \sim y_c^+. \quad (4.48)$$

The ratio $\sqrt{\chi_{11}^{\text{SQ/SQ}} / \chi_{11}^{\text{OS/OS}}}$ is plotted along several hierarchies with different $k_{x,l}, k_{z,l}$ for $Re_\tau = 2003$ in Figure 4.17. In this case, to have a sufficient number of wavespeeds belonging to \mathcal{S}_h while keeping the size of the optimization problem manageable, the matching of the DNS spectra is only enforced for $y_{\min}^+ = 100 \leq y^+ \leq 0.1 Re_\tau = y_{\max}^+$, with $N_c = 25$. The scaling given by Equation (4.48) is clearly demonstrated, as the data in all cases exhibit a linear dependence on y_c^+ to within a good approximation. In all cases shown, the aspect ratio at the bottom of the hierarchies is $\gamma = 5$. Similar results are obtained using different aspect ratios, provided that $\gamma \gtrsim \sqrt{10}$ (Moarref et al., 2013a). The slopes of the lines are observed to decrease with increasing $k_{x,l}$. Although not shown here, the slopes tend to increase with increasing γ .

4.4 Discussion

A low-order representation of the time-averaged energy spectra of turbulent channel flow based on the resolvent analysis framework was presented. The resolvent

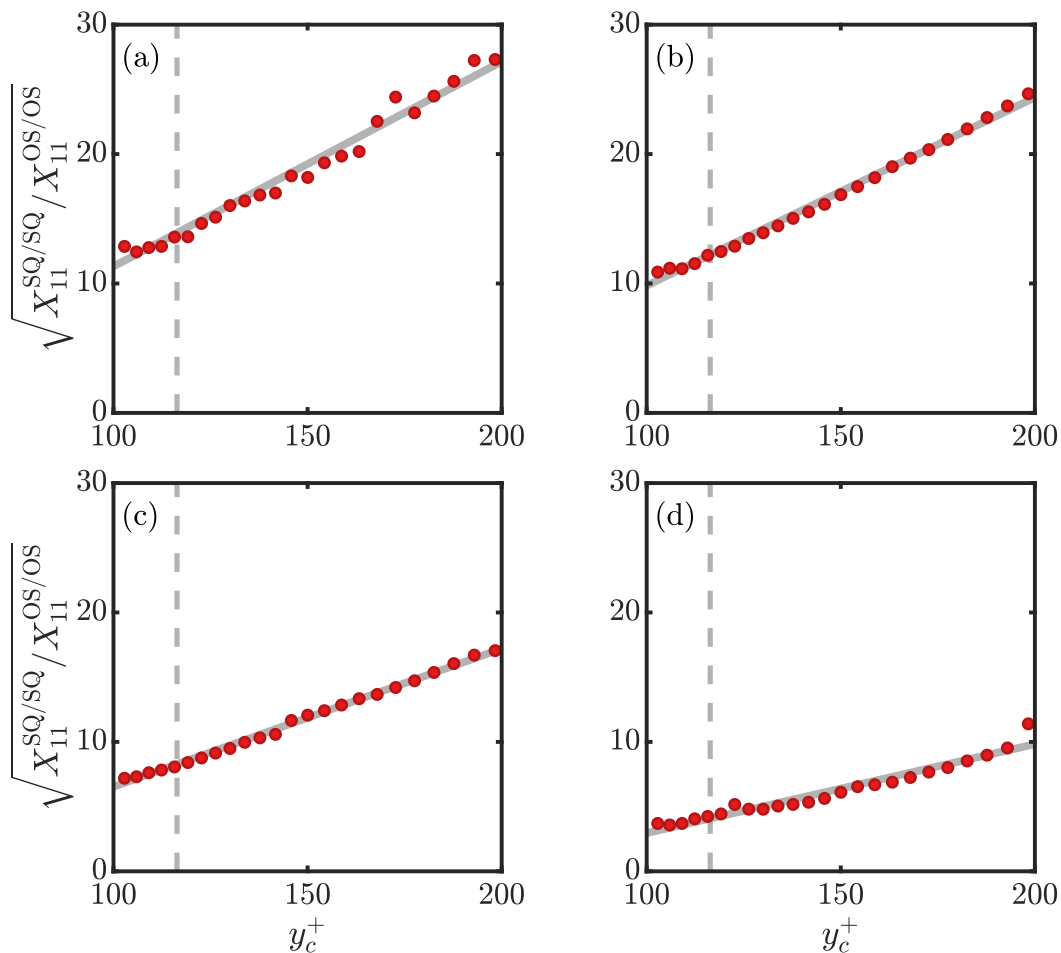


Figure 4.17: Leading weights ratio along hierarchies for $Re_\tau = 2003$ with $N = 2$. Each panel is a different hierarchy, represented by the streamwise wavenumber at the bottom of the hierarchy: (a) $k_{x,l} = 1$; (b) $k_{x,l} = 5$; (c) $k_{x,l} = 10$; (d) $k_{x,l} = 20$. In all cases, the spanwise wavenumber at the bottom of the hierarchy is $k_{z,l} = \gamma k_{x,l}$, with $\gamma = 5$. The solid gray lines are the least-squares linear fits, with slopes (a) 0.158, (b) 0.145, (c) 0.107, and (d) 0.069. The dashed gray lines are $y^+ = 2.6Re_\tau^{1/2} \approx 116$.

mode weights, which encode information about the nonlinear interactions in the flow, were determined empirically by computing the weights that minimize the deviation between the resolvent spectra and spectra obtained from DNS using a convex optimization scheme. The present approach is a modification of previous work (Moarref et al., 2014a), with the major difference being the incorporation of a recently-proposed alternative decomposition of the resolvent operator into two distinct families of modes, referred to as the Orr-Sommerfeld and Squire families (Rosenberg and McKeon, 2019b).

It was demonstrated that the alternative OS-SQ decomposition results in a dramatic improvement in the performance of the representation. This improvement is attributed to the isolation of the ν response in the OS family, which enables the η response of the SQ family to compete with the large η response generated by the OS modes. Furthermore, for certain values of the wave parameters, the leading modes of the standard resolvent operator are almost identical to the leading modes of the OS resolvent, so that the mechanisms encoded in the SQ operator are essentially neglected; this helps explain the relatively poor performance of the representation obtained using the standard resolvent. A decomposition of the statistics into contributions from the OS modes, SQ modes, and an interaction between the two families supports this claim and is in agreement with results from DNS at $Re_\tau = 185$ (Rosenberg, 2018). It was further shown that the competition between the OS and SQ modes can be interpreted as a phase difference, and that this phase difference is speculated to be close to π over large portions of spectral space.

Next, the scaling of the leading singular values for the OS and SQ families were derived for the inner, outer, and geometrically self-similar universal classes of resolvent modes (Moarref et al., 2013a). For the inner class, both sets of singular values scale as Re_τ^{-1} . For the outer and self-similar classes, the OS singular values are larger than the SQ ones by a factor of Re_τ and y_c^+ , respectively. Interestingly, this large difference in amplification suggests that modes in these classes are likely to be among those for which the OS and standard resolvent modes are nearly identical. Indeed, the scaling of the leading OS singular values is the same as that for the leading singular values of the standard resolvent for the outer and self-similar classes. For the inner class, the scaling for both the OS and SQ singular values matches the standard resolvent. These scalings, combined with the hypothesis that the competition between SQ and OS modes discussed above remains relevant for arbitrary Re_τ and throughout the flow domain, were used to derive the relative

scalings of the OS and SQ weights in each of the universal classes. The scaling predictions were tested against the optimized weights, and, with the exception of high aspect ratio modes of the inner class localized very near the wall, good agreement with the computed optimal weights was found for each of the universal classes.

The results presented herein have several important implications for equation-driven modeling of turbulent channel flow. The first is that partitioning the resolvent operator into Orr-Sommerfeld and Squire subsystems, originally presented in the context of ECS (Rosenberg and McKeon, 2019b), is also advantageous in terms of its ability to develop compact representations of fully turbulent channel flow at high Reynolds number. Furthermore, it provides valuable insight into the complex dynamics by identifying the competition mechanism between the OS and SQ modes, which has ramifications for modeling nonlinear interactions. Specifically, considering that for large Re_τ , the OS singular values in the logarithmic and outer regions of the flow are much larger than the SQ ones, it may be tempting from a modeling perspective to neglect the SQ family of modes. However, doing so does not take into account the relative scaling of the forcing terms \hat{g}_v and \hat{g}_η in Equation (4.10) – it implicitly assumes they remain of the same order. The present results indicate that this is not the case. In fact, the scaling results of the weights for all of the classes can be summarized as $|\chi_j^{\text{SQ}}/\chi_j^{\text{OS}}| \sim \sigma_j^{\text{OS}}/\sigma_j^{\text{SQ}}$.

Though the absolute scalings of the weights were not determined, the present work can be considered a starting point to guide further modeling efforts toward quantifying nonlinear interactions in turbulent channel flow. For instance, it is particularly intriguing that, as discussed in Section 4.2, the v statistics depend only on the OS modes. Consequently, if the scaling of the OS weights can be determined from these, empirically or otherwise, then the results given in Section 4.3 can be used to determine the scaling of the SQ weights, effectively reducing the number of unknowns by half. Then a single computation at a relatively low Reynolds number could be combined with the scalings to make predictions of the spectra at Reynolds numbers that are currently unattainable by DNS.

Taken together, the results point to the competition between the OS and SQ modes being an important mechanism in turbulent channel flow that should be respected in order to accurately model the statistics. We hypothesize that if this mechanism could be interrupted, the dynamics, and consequently the statistics, of the system would be significantly different. This line of inquiry is the subject of ongoing work.

Chapter 5

A DATA-DRIVEN APPROACH FOR GENERATING INITIAL GUESSES OF EXACT COHERENT STATES

5.1 Chapter overview

As discussed in Section 1.4, upper-branch (UB) equilibria are typically harder to compute than their lower-branch (LB) counterparts. Consequently, methods to generate good initial guesses of a UB solution for a Newton search are valuable. The standard method for obtaining UB solutions is using branch continuation, in which a known solution for a particular Re is used as an initial guess for solutions at higher or lower Re . While continuation is an extremely useful technique, providing a wealth of information by tracing out a particular solution in parameter space, it can be computationally costly. Thus, if one is interested in the behavior of the UB at a particular Re , it would be desirable to have the option to “jump” from a known LB solution to the corresponding UB¹. Furthermore, this ability would complement the work of Rosenberg and McKeon (2019a), who used a resolvent-based iterative method to compute LB solutions directly from the laminar state. Rosenberg (2018) additionally proposed a simple extension of the method to generate UB solution guesses by using an “over-amplified” version of the LB mean forcing; however, *a priori* knowledge of the UB mean profile informed the value of the amplification factor used.

The basic idea of “branch jumping” is illustrated schematically in Figure 5.1, which shows a typical bifurcation diagram for a hypothetical equilibrium solution family. In this diagram, the closed circle represents an initial known LB solution, which can be continued up and down in Re (horizontal arrows) to trace out the blue curve. The open circle represents the desired UB solution, and the vertical arrow illustrates the jump from between the two. The dashed portion of the UB curve indicates the region beyond which continuation has been performed.

The general problem statement then amounts to finding a mapping \mathcal{F} such that $\mathbf{u}_{UB} = \mathcal{F}(\mathbf{u}_{LB})$, where \mathbf{u}_{LB} and \mathbf{u}_{UB} denote LB and UB solutions, respectively. Ideally, such a mapping could be deduced through analytical and physical insight. However, due

¹The contents of this chapter were conceived during a visit with the Graham group at UW-Madison. We are extremely grateful to Michael D. Graham for making this possible, and to Alec Linot for numerous illuminating discussions.

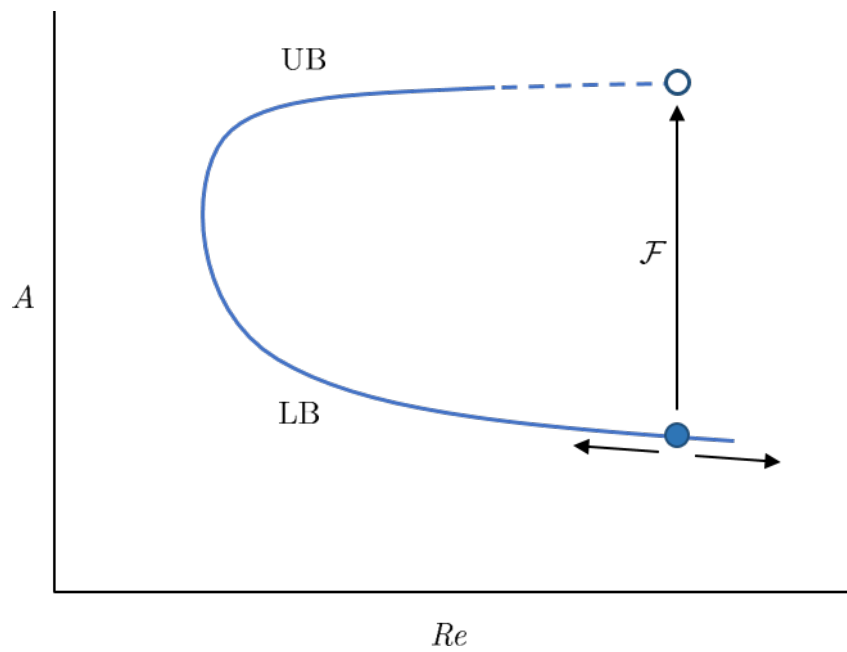


Figure 5.1: Schematic of “branch jumping”. “UB” and “LB” denote upper- and lower-branch solutions, respectively, and A is some measure of amplitude used to construct the bifurcation diagram. The closed circle represents a known LB solution, the open circle represents the desired UB solution, and \mathcal{F} is the proposed mapping between the two.



Figure 5.2: Schematic of the neural network “workflow”.

to its almost assuredly nonlinear nature, this is a potentially prohibitively difficult task. In light of this, resorting to a data-driven approach may be more fruitful. In particular, neural networks are particularly well-suited for this task, which is essentially nonlinear regression. By training a network to “learn” \mathcal{F} , one could then use it to generate an initial guess of UB solutions without having to perform a continuation. Moreover, the learned mapping could in principle be used to generate initial guesses for uncovering new solutions.

The primary goal of this chapter is a proof-of-concept demonstrating the utility of neural networks as a data-driven tool to generate initial guesses of UB solutions that can then be used in a Newton search. The demonstration will be performed using known equilibria families in Couette flow. First, the details of the training protocol and network architecture will be presented. Then, the performance of the network will be assessed, and the successfully converged solutions will be discussed. The consequences of symmetry breaking by the network will receive particular attention. Finally, outlook for further application of the approach will be given.

5.2 Methods

In this section, we present the method through which a neural network is used to generate predictions of UB equilibria. At a high level, an LB solution at a particular Re is provided as an input to the (trained) network, which generates a prediction of a UB solution at the same Re , which we denote UB_{NN} . UB_{NN} is then used as an initial guess for a Newton search, which hopefully converges to a true UB equilibrium. This basic “workflow” is summarized in the schematic shown in Figure 5.2, and the various sub-blocks are described in further detail in the following subsections.

Training data

Before discussing the neural network itself, we first describe the dataset used to train it. The training data comprise LB and UB pairs of Couette flow equilibria over a range of Re . The equilibria families considered are EQ1-2 and EQ3-4, where, following the naming convention of Ahmed and Sharma (2020), the first number designates the LB solution, and the second number designates the corresponding

UB solution. EQ1-2 are the original Nagata equilibria (Nagata, 1990), which appear in a saddle-node bifurcation at $Re \approx 218$. EQ4 was first discovered by Gibson et al. (2008), and EQ3 was obtained by continuing it downwards in Re (Gibson et al., 2009); the saddle-node bifurcation for this pair occurs at $Re \approx 364$. A bifurcation diagram for both families is shown in Figure 5.3. The solutions are plotted in terms of the fluctuation energy

$$E := \frac{1}{2L_x L_z} \int_{\Omega} \mathbf{u} \cdot \mathbf{u} \, d\Omega, \quad (5.1)$$

where $\Omega = [0, L_x] \times [-1, 1] \times [0, L_z]$ is the spatial domain, and $\mathbf{u} = \tilde{\mathbf{u}} - y\mathbf{e}_y$ are the fluctuations about the laminar solution. For both equilibrium families, $L_x = 2\pi/1.14$ and $L_z = 4\pi/5$. From Equation (5.1), it is apparent that the UB solutions correspond to the branch with larger E . The bifurcation curves for both families exhibit the simple LB-UB structure illustrated in Figure 5.1. Evidently, EQ3-4 are weaker, i.e., are closer to laminar, than EQ1-2.

To illustrate the structure typical of these solutions, the streamwise-averaged fluctuation fields of EQ1-2 and EQ3-4 at $Re \approx 500$ are shown in Figures 5.4 and 5.5, respectively. In both cases, the basic flow features are a low- and high-speed streak concentrated primarily in the upper and lower halves of the channel, respectively, and two counter-rotating streamwise “rolls” centered near the channel midplane.

Data for the EQ1-2 and EQ3-4 families were obtained from Ahmed and Sharma (2020). The resolution for all solutions is $(N_x, N_y, N_z) = (32, 35, 32)$, which is consistent with previous studies (e.g., Gibson et al., 2008). The Re range of the training data is $402 \lesssim Re \lesssim 1000$ for EQ1-2 and for $420 \lesssim Re \lesssim 1000$ for EQ3-4. The lower Re limit was chosen to exclude the vicinity of the bifurcation point, in which the LB and UB solutions are not well distinguished. Altogether, this results in 39 LB-UB pairs. This is a much smaller data set than is typically used for training neural networks, as a small training dataset increases the likelihood of overtraining. However, we are not aware of a significantly larger library from which to draw more data, and we note that this is potentially a limitation of the present approach.

Data preprocessing

Due to the continuous symmetry of plane Couette flow in the streamwise and spanwise directions, any given solution has infinitely many “copies” corresponding to streamwise and spanwise shifts. Such ambiguity has the potential to obscure the relationship between LB and UB solutions that the neural network is attempting to

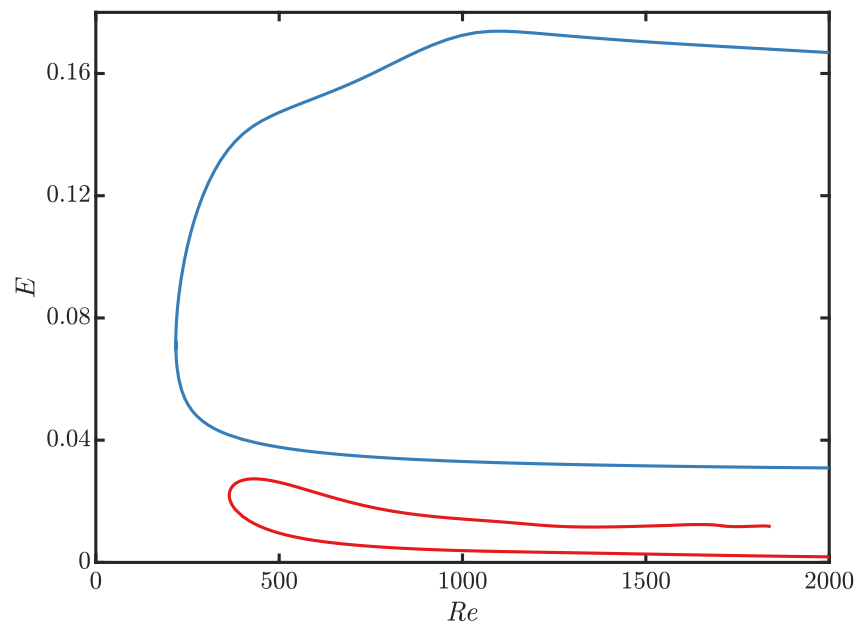


Figure 5.3: Bifurcation diagram for EQ1-2 (blue) and EQ3-4 (red).

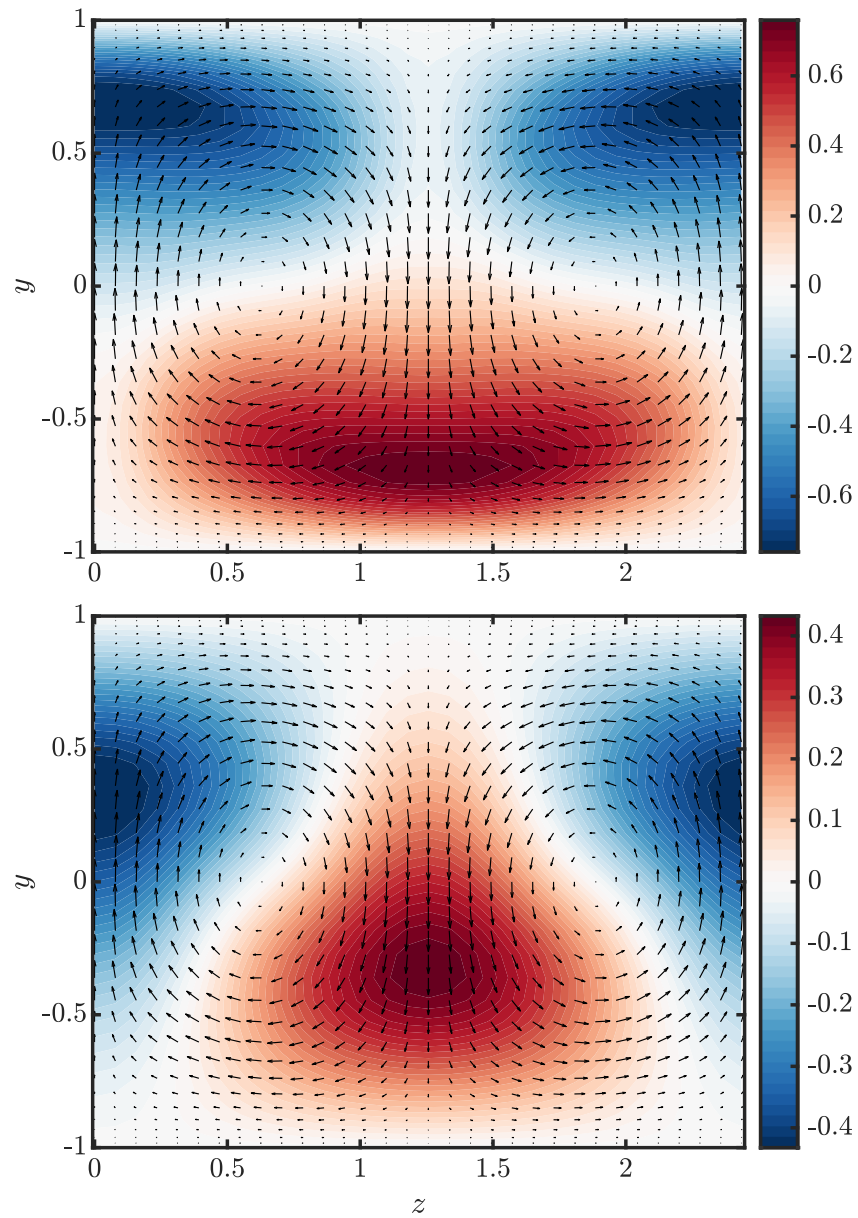


Figure 5.4: Streamwise-averaged velocity fields of EQ2 (top) and EQ1 (bottom) for $Re \approx 500$. Contours: u , vectors: v, w .

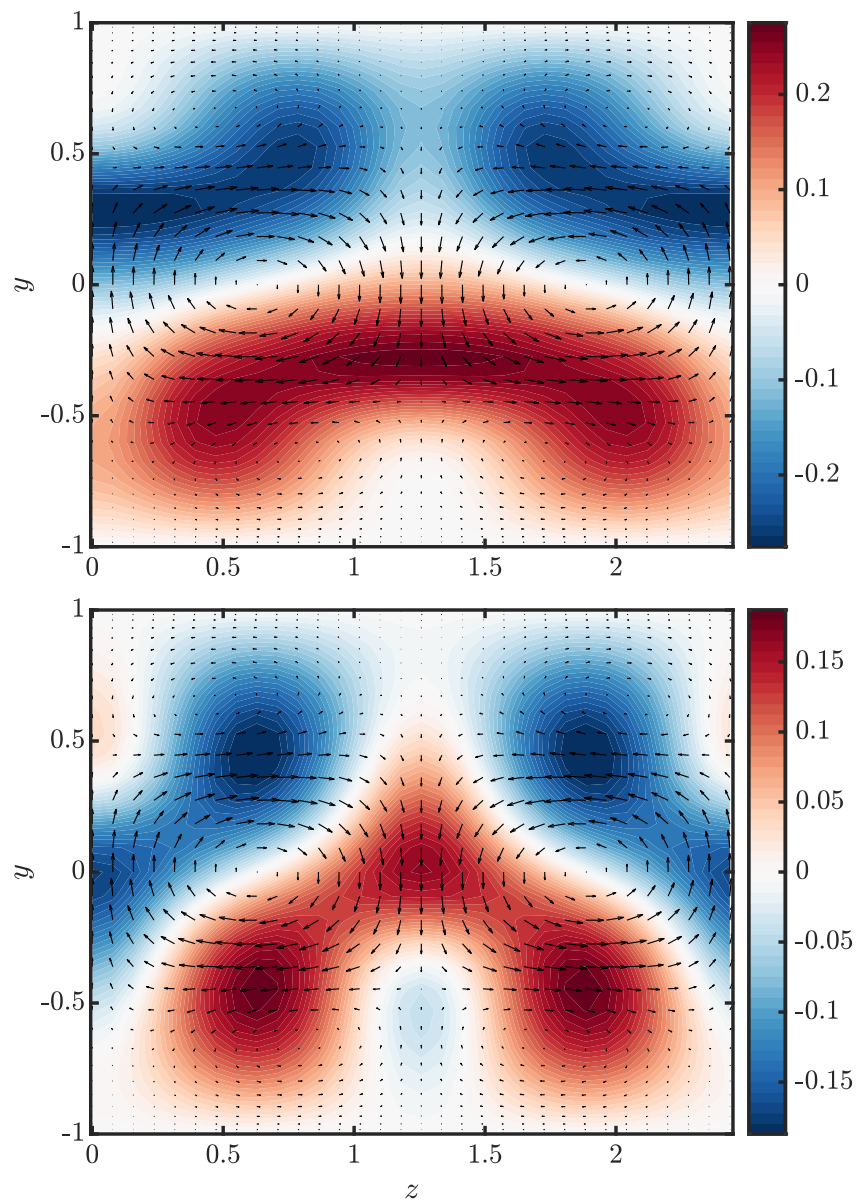


Figure 5.5: Streamwise-averaged velocity fields of EQ4 (top) and EQ3 (bottom) for $Re \approx 500$. Contours: u , vectors: v, w .

learn by forcing it to also learn arbitrary shifts. We instead choose to eliminate this possibility by phase-shifting the training solutions such that the fundamental x and z Fourier modes of w at a particular wall-normal height y_s are real; that is, $\arg \hat{w}(k_x = 2\pi/L_x, y_s, 0) = \arg \hat{w}(0, y_s, k_z = 2\pi/L_z) = 0$.

Additionally, since the training data set rarely have both an LB and UB solution at a given Re , the LB solutions are linearly interpolated to match the Re for each UB solution. Since the steps in Re for the LB solutions are relatively small, typically ≈ 40 , it is not anticipated that this workaround significantly affects the performance of the network.

Neural network description

The neural network is implemented in Python using TensorFlow (Abadi et al., 2015) and Keras (Chollet et al., 2015). The network is a simple sequential network with densely-connected layers. Network input data, i.e., the LB solution arrays, are flattened into a vector, so that the dimension of the input layer is $D_i = N_x N_y N_z = 35840$. Since the UB solutions have the same resolution as the LB ones, the output layer dimension is $D_o = D_i$. The number of hidden layers was varied from one to four, and negligible difference was observed when using two or more. Several values of the hidden layer dimension D_h were tested. $D_h = 1024$ results in predictions of poor accuracy, while $D_h \gtrsim 3000$ requires more computing power than available on the workstation used. However, larger D_h was not pursued since $D_h = 2048$ produced results that were deemed sufficiently accurate for the present purposes. The activation function for all of the hidden layers is the rectified linear unit (ReLU), and the output layer activation is linear. The details of the network architecture are summarized in Table 5.1.

Table 5.1: Details of the neural network architecture.

Layer	Input	Hidden	Output
Dimension	35840	2048	35840
Activation		ReLU	linear

The loss function J to be minimized is a modification of the standard mean-square error (MSE) designed to penalize deviations in all three velocity components evenly:

$$J := \frac{1}{N} \sum_{k=1}^N \left(\frac{\|u'_k - u_k\|_2^2}{\|u_k\|_2^2} + \frac{\|v'_k - v_k\|_2^2}{\|v_k\|_2^2} + \frac{\|w'_k - w_k\|_2^2}{\|w_k\|_2^2} \right), \quad (5.2)$$

where N is the size of the training data set, and $(\cdot)'$ denotes the neural network prediction. The network was trained for 100-300 epochs using the Adam optimizer (Kingma and Ba, 2015). The number of epochs was selected to achieve a balance between obtaining a low training error and reducing possibility of overtraining. Training of the network was repeated several times to verify that the results presented here do not vary significantly between particular training outcomes.

Newton search details

The predictions from the neural network are used as an initial guess for a Newton search, implemented using Channelflow's built-in `findsoln` function (Gibson, 2014). Specifically, this function uses a Newton-Krylov-hookstep (NKH) algorithm (Viswanath, 2007a) to minimize the residual

$$\mathbf{G}(\tilde{\mathbf{u}}, T, \sigma) := \sigma \mathbf{F}^T(\tilde{\mathbf{u}}) - \tilde{\mathbf{u}}, \quad (5.3)$$

where \mathbf{F}^T is the forward map of the NSE by time T , and σ is a symmetry operation. The convergence criterion is $\|\mathbf{G}\| < \varepsilon$. Here, we use the default value $\varepsilon = 10^{-13}$. Other parameters to be specified for the search are the time integration horizon T and the number of Newton iterations N_N performed before aborting the search if the convergence criterion is not met. The default value of $T = 20$ is used, and N_N was increased from 20 to 40 since some of the searches converged rather slowly. A set of symmetry operations σ can also be specified to restrict the search to the corresponding the symmetry-invariant subspace. However, this was not done for the searches initiated from the neural network predictions, as they generally do not satisfy any of the symmetries of the training solutions. The implications of this will be discussed in the proceeding section.

5.3 Results

Convergence range

Examples of the neural network predictions are compared to the true UB solutions for EQ2 and EQ4 in Figures 5.6 and 5.7, respectively. Overall, the predictions do a good job capturing the main features of the solution. However, there are notable discrepancies, including a tendency to slightly under-predict u , as well as to over-predict v and w . Additionally, the v and w fields often appear slightly noisy; this is most apparent in the v component for EQ4, shown in Figure 5.7. Finally, we note that the predicted fields generally do not satisfy the no-slip boundary conditions or continuity. While no attempt was made to address the continuity issue, no-slip is enforced by directly zeroing the values at the walls prior to the Newton search. To

quantify the prediction error, we report the L^2 distance (c.f. Equation (5.1)) between the predictions and true equilibria. For the examples shown in Figures 5.6 and 5.7, they are 0.0175 and 0.0279, respectively. In both cases, Newton searches initiated from these guesses converged.

As described in Section 5.1, the primary objective is to use the trained neural network to generate guesses for UB solutions at higher Re . Success is determined by whether or not such a UB guess results in a converged equilibrium from a Newton search. To determine the range of convergence, searches were performed at progressively higher Re until a solution could not be obtained within 40 Newton iterations. For EQ2, this occurred at $Re \approx 1188$, and at $Re \approx 1249$ for EQ4. It was observed that searches for EQ4 generally converged more quickly than those for EQ2, which, as previously discussed in reference to Figure 5.3, is likely a consequence of the fact that the EQ4 solutions are weaker. Thus, the neural network predictions enable an extension in Re by roughly 200. However, we note that this is also the range in which the highest Re member of the UB training data can be successfully used as an initial guess. As mentioned in Section 5.2, this suggests limited generalizability of the network, likely resulting from overtraining on the limited data set. Nonetheless, the results may be considered an encouraging proof of concept.

Symmetries of the solutions

Almost all of the known ECS in plane Couette flow are highly symmetric (Ahmed and Sharma, 2020). We do not detail the symmetries admitted in Couette flow here, as they have been cataloged elsewhere in the literature (e.g., Gibson et al., 2008). For the present purposes, it is sufficient to note that EQ1-2 and EQ3-4 each satisfy three discrete symmetries in addition to the identity operation. Namely, they are the “shift-reflect” and “shift-rotate” symmetries, as well as their composition (Gibson et al., 2009). However, as mentioned in Section 5.2, none of these symmetries are imposed when performing the Newton searches. That is, we set σ to be the identity in Equation (5.3). This is because the neural network predictions do not satisfy them², and doing so results in failure to converge.

Figures 5.8 and 5.9 compare the streamwise-averaged fields for the known EQ2 and EQ4 solutions (left column), respectively, with the converged results using the neural network prediction at the same Re (center column). They are visually

²The symmetries of a solution are numerically checked by applying a set of symmetry operations to it and then computing the distance from the original field. If the distance is $< 10^{-6}$ (the default in Channelflow), then the solution is said to satisfy that symmetry.

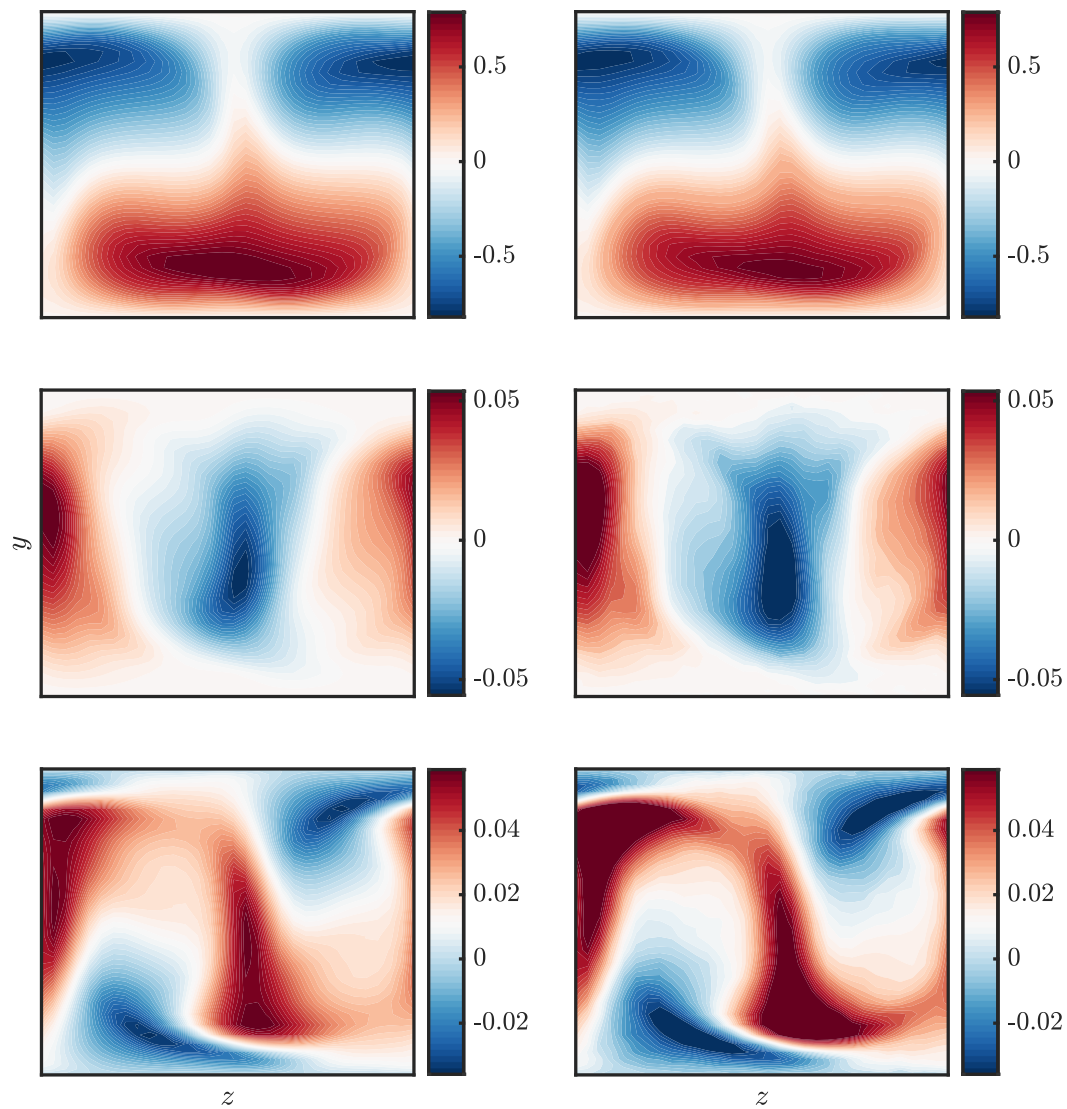


Figure 5.6: Comparison of EQ2 (left) and the neural network prediction (right) in the plane $x = 0$ for $Re = 1148$. u : top, v : middle, w : bottom.

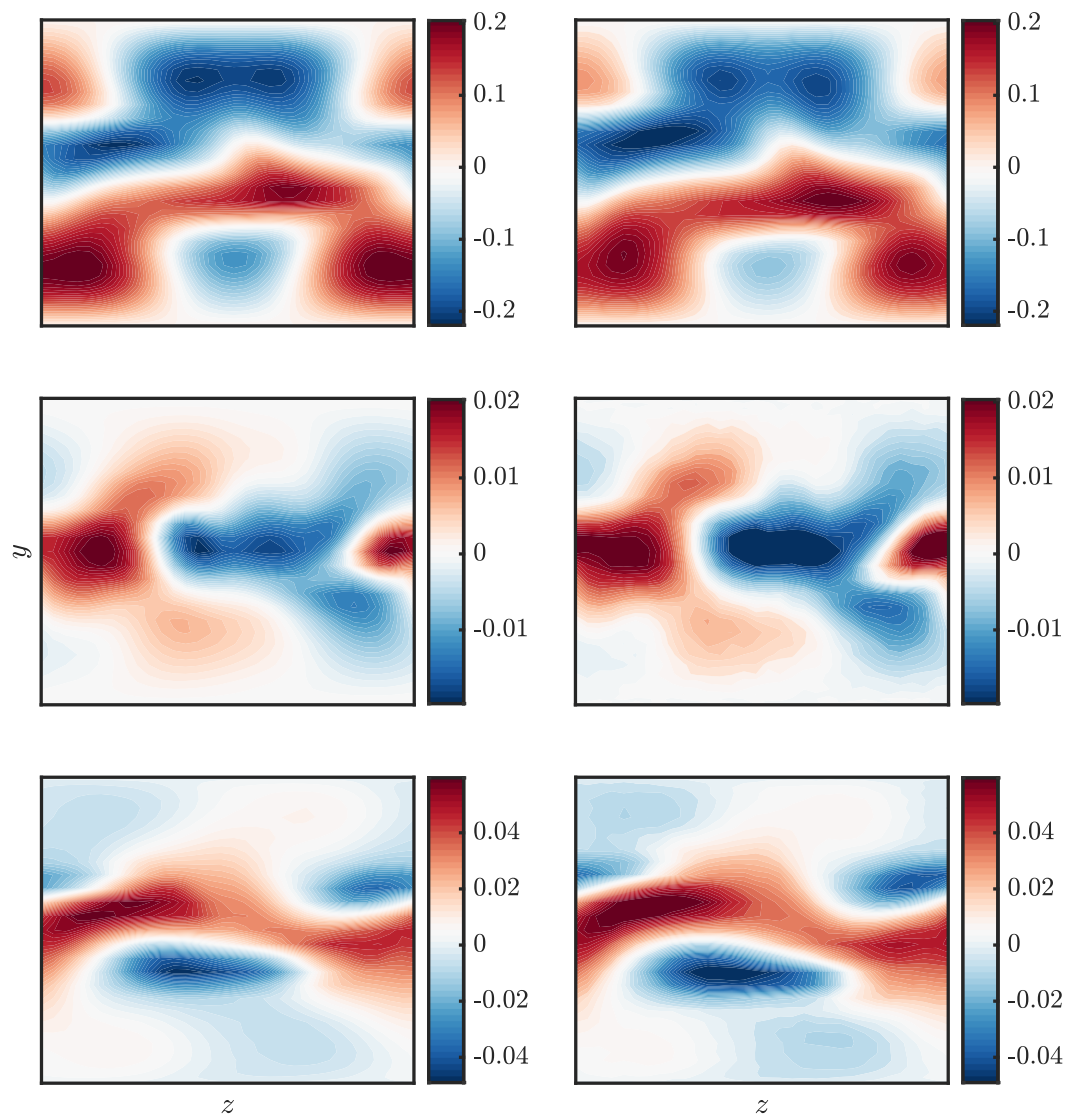


Figure 5.7: Comparison of EQ4 (left) and the neural network prediction (right) in the plane $x = 0$ for $Re = 1209$. u : top, v : middle, w : bottom.

indistinguishable. Furthermore, their bulk quantities, such as norm and dissipation rate, agree to at least seven significant figures. Finally, after applying the same phase shifting procedure used for the training data, the L^2 distance between the two is at most $O(10^{-8})$, suggesting the Newton searches converge to the desired solutions.

Interestingly, however, the converged equilibria from the neural network predictions also do not share any symmetries with EQ2 or EQ4. This is surprising, given the strong qualitative and quantitative similarity between them. Also shown in the right column of Figures 5.8 and 5.9 is the difference between the known equilibria and the asymmetric states. While the magnitudes of the difference fields are extremely small, consistent with the L^2 distance, they exhibit clear structure, which implies that the symmetry breaking is not merely the result of numerical error.

Beyond satisfactory convergence in the Newton search, several additional checks were performed to confirm that the asymmetric solutions are in fact equilibria. First, they were integrated forward in time for $T = 100$, five times the value of the horizon used for the Newton searches, and then compared to the initial state. The distance between them is typically $O(10^{-10})$ or smaller. Additionally, several solutions were also interpolated onto a finer grid, with $(N_x, N_y, N_z) = (48, 51, 48)$, and a another Newton search was initiated. The converged result was compared to the initial guess, and the distance between them was typically $O(10^{-5})$. This distance is of the same order as that computed when this process was repeated for the known EQ2 solution, indicating the asymmetric solution is sufficiently resolved.

5.4 Discussion

In this chapter, we have, as a proof of concept, demonstrated that a very simple implementation of a neural network trained on lower- and upper-branch equilibrium pairs can generate initial guesses for Newton searches that successfully yield converged UB solutions at higher Re . Although the Re range of successful convergence is not significantly better than what can be achieved using training data as an initial guess, this does not rule out the possibility that a larger training dataset combined with optimization of the network architecture can result in substantially better performance. Moreover, since the neural network predictions do not share any the discrete symmetries with the solutions used for training data, they could potentially lead to successful convergence in the vicinity of a bifurcation point, which is often associated with symmetry breaking. Finally, the small size of the hidden layers relative to the full solution dimension hints at the possibility of significant compression,

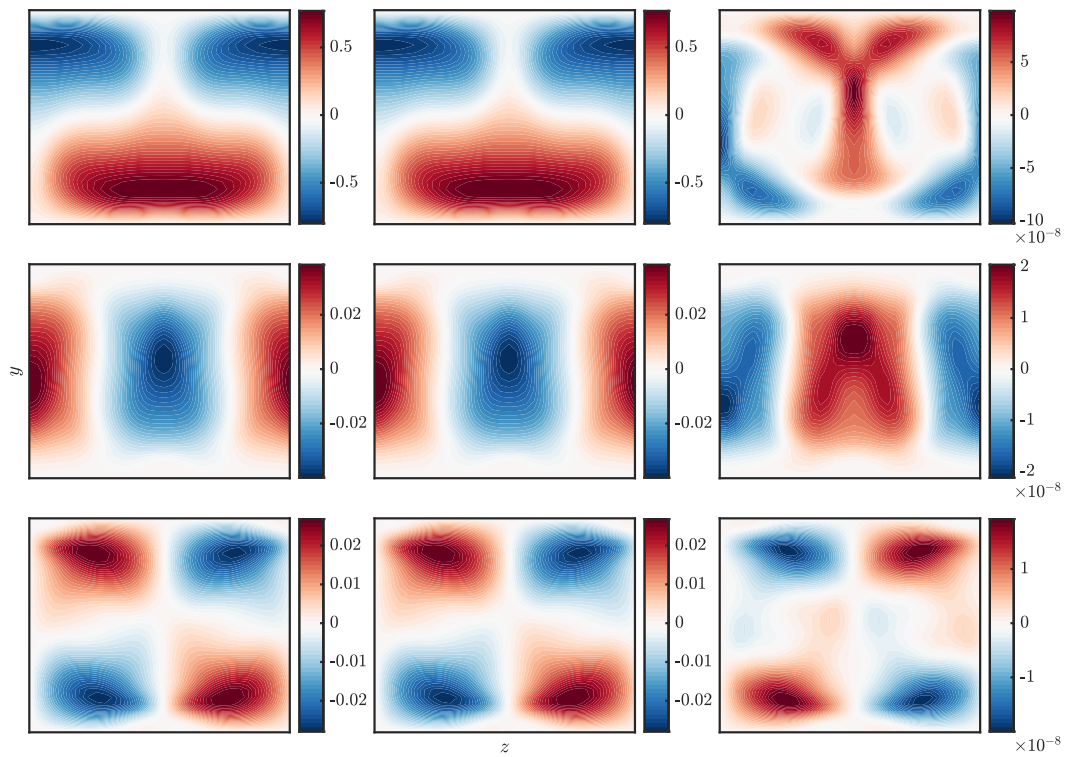


Figure 5.8: Comparison of streamwise averages for EQ2 (left) and the converged state using the neural network initial guess (center), as well as their difference (right) for $Re = 1148$. u : top, v : middle, w : bottom.

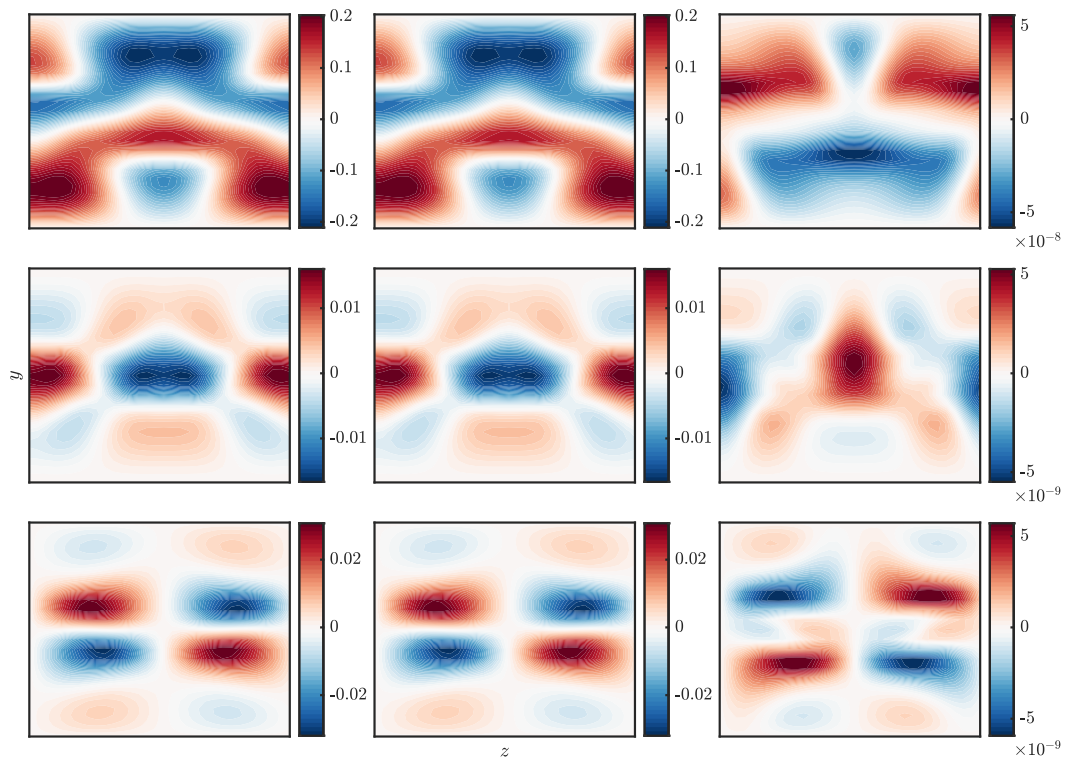


Figure 5.9: Comparison of streamwise averages for EQ4 (left) and the converged state using the neural network initial guess (center), as well as their difference (right) for $Re = 1209$. u : top, v : middle, w : bottom.

and a potential direction for future work is an investigation of network “modes” that could be used in low-order representations.

The most notable feature of the converged equilibria obtained from the neural network predictions is that they also do not satisfy the symmetries of the EQ1-2 or EQ3-4 families. While the differences leading to the symmetry breaking are small, they cannot easily be discounted as merely numerical error. This has several interesting implications. For instance, one possible interpretation is that the regions of state space surrounding many of the known, highly symmetric solutions are populated by similar but asymmetric solutions. Significantly, this would then suggest that a turbulent trajectory that makes a close “visit” to an equilibrium need not satisfy its symmetries. Another intriguing question is how the small asymmetric deviations alter the self-sustaining mechanisms of an equilibrium. This question in particular is well-suited to be addressed via projection onto resolvent modes (Sharma et al., 2016; Rosenberg and McKeon, 2019b), as the resolvent framework provides a natural setting to analyze triadic interactions.

In terms of broader outlook, it seems unlikely that any particular learned mapping \mathcal{F} will apply to all families of equilibria. However, it would still be interesting to see what features do generalize. Particularly, since some LB and UB solutions sit on opposite sides of the laminar-turbulent state space boundary (Gibson et al., 2008), this may provide additional insight into what features separate an initial condition that ultimately decays to laminar from one that leads to turbulence. Finally, we believe that the present approach is not restricted to equilibria and, provided that they have a similar LB-UB structure, could likely be extended to other special solutions like traveling waves or periodic orbits, though slight modifications to generate guesses of the wavespeed or orbit period may be required.

CONCLUSIONS AND FUTURE WORK

This thesis described the application of reduced-order modeling techniques to three problems in wall-bounded turbulence. Here, we summarize the major findings for each of them and offer some perspective on how the results could be built upon in future work.

First, the mechanisms underlying the characteristic structures of elastoinertial turbulence (EIT) at low Re were elucidated. This was accomplished using a combination of resolvent and modal stability analyses. The dependence on Wi of linear mechanisms was studied in the context of componentwise worst-case amplification. Two cases, $Wi = 7$, representative of low levels of drag reduction, and $Wi = 20$, which corresponds to EIT at $Re = 1500$, were chosen. It was found that the low drag reduction case is largely dominated by streamwise-oriented modes, which is consistent with observations from DNS. In EIT, however, there is a shift to large amplification for spanwise-oriented modes, and the streamwise wavenumber k_x of these agrees very closely with the wavenumber of the most energetic structures from DNS. Furthermore, it was shown that the structure of the most-amplified spanwise mode bears strong resemblance to DNS snapshots. In particular, it captures the wall-normal location and extreme localization of the highly-inclined sheet-like stress fluctuations, and the localization was shown to occur at the critical layer of the most-amplified mode. Since $Wi = 20$ corresponds to a state just beyond transition to EIT at $Re = 1500$, combined modal and nonmodal stability analyses of the laminar state were performed in order to better understand the origin of such structures. The modal analysis revealed that the most-amplified mode is closely linked to the viscoelastic extension of the classical Tollmien-Schlichting (TS) mode. A focus on the critical layer, which locally resembles the Kelvin's cat's eye structure, suggests that a likely mechanism for the strong polymer stretching is the presence of the hyperbolic stagnation points situated between the cat's eyes. Finally, it was shown that the critical-layer localization is Wi -dependent: For $Wi \lesssim 3$, the relative amplitude of conformation tensor fluctuations to wall-normal velocity fluctuations exhibits simple-shear scaling $\sim Wi^2$, consistent with the fact that the conformation tensor fluctuations peak at the wall where the flow locally resembles simple shear. However, at $Wi \approx 3$, the scaling undergoes an abrupt change, after which it does not

obey a simple power-law. This transition coincides with the conformation tensor fluctuation peak moving away from the wall and shifting toward the critical layer. Importantly, these observations also hold for nonlinear TS waves, as was demonstrated by qualitative and quantitative agreement with both saturated viscoelastic TS waves and the recently-discovered viscoelastic nonlinear TS attractor (Shekar et al., 2020). Taken together, the results of this chapter point to the importance of critical-layer mechanisms in EIT, as well as a close link to TS-like dynamics. Thus, an important open question is how exactly the two are connected in parameter space, as well as how they related to different instabilities unique to viscoelastic shear flows (Garg et al., 2018; Chaudhary et al., 2019).

Next, an alternate decomposition of the resolvent operator was used to obtain an accurate low-order representation of second-order statistics in turbulent channel flow at moderate Re_τ . The decomposition first partitions the resolvent into two separate operators that are closely related to the Orr-Sommerfeld (OS) and Squire (SQ) operators from classical linear stability theory (Rosenberg and McKeon, 2019b); performing a singular value decomposition of each operator yields two families of resolvent modes. Compared to a low-order representation using the full resolvent operator, the OS-SQ decomposition results in a dramatic improvement in the accuracy with which the time-averaged statistics can be reproduced. Moreover, it produces reasonable estimates of the shapes of both the temporal power spectrum and the nonlinear forcing spectrum. This is particularly significant since no explicit information about the flow's frequency content or nonlinear terms is required to produce the estimates. The markedly better performance was understood to result from the competitive interaction between the OS and SQ vorticity. Decomposing the statistics into contributions from OS modes, SQ modes, and a cross term clearly supports this idea and, furthermore, admits a simple interpretation in terms of a phase difference between the OS and SQ modes. Additionally, it was shown that, in some cases, the leading response modes of the full resolvent operator coincide with the OS modes, thereby explaining why the low-order representation using the full operator performs relatively poorly. The OS-SQ vorticity competition mechanism was then leveraged to derive scaling behavior for the weights of resolvent modes belonging to three special universal classes. The scaling predictions were tested against the optimal weights computed for several Re_τ , and good agreement was observed for all three classes. This implies that the competition mechanism is important for any Re_τ sufficiently large to exhibit universal scaling of the mean profile. While only a first step, these results may prove useful for further analyses of nonlinear interactions in

wall-bounded turbulence. We note that the present formulation does not provide any formal guarantees of convergence as more modes are included, and it was shown that the errors persist for large streamwise wavelengths, where there is significant energetic content below the peaks of the lowest wavespeed resolvent modes. Further work is required to improve the representation in these cases. Additionally, because only second-order statistics were considered, the method does not provide access to phase relationships between modes with different wavenumbers. An extension incorporating this would be extremely valuable, as it could potentially provide dynamical information and, ideally, eliminate the need for *a priori* knowledge of the mean profile, as was assumed herein. Rosenberg and McKeon (2019a) developed an iterative resolvent-based approach that successfully circumvents reliance on a known mean for several traveling wave ECS for which the mean is essentially sustained by the self-interaction of a single mode. Obviously, achieving a similar result for fully-developed turbulence, which involves interactions between many spatiotemporal scales, will be considerably more challenging. Nonetheless, their approach demonstrates that such a goal may be attainable. Finally, though the present work concerns a statistical analysis of the OS-SQ competition, an intriguing direction for future work would be to see how this mechanism plays out in the dynamics, as well as how the turbulence is altered if it were to be interrupted.

Last, the focus shifted slightly from resolvent analysis to exact coherent states (ECS), where the main goal was to develop a data-driven method capable of generating good initial guesses of upper-branch equilibria in Couette flow. To this end, a neural network was trained on multiple equilibrium families in order to produce guesses at higher Re . The simple implementation of a neural network demonstrated initially encouraging results for the feasibility of this approach by generating predictions that successfully lead to converged equilibria over a limited range of Re . It is hoped that access to a larger training dataset and a more sophisticated network could further improve the performance. An investigation of the successfully converged solutions was performed, revealing that, despite being very close (in state space) to the known equilibria, they did not share any of their symmetries. While the asymmetric deviations were small, they do not appear to be the result of numerical error. An interesting possibility this raises is that a given symmetric equilibrium may be surrounded in state space by other similar asymmetric solutions. Finally, this also leads to more general questions about how the self-sustaining mechanisms of ECS are altered when symmetries are broken.

While each of the three problems presented in this thesis may initially seem somewhat unrelated, we now argue that they in fact pertain to the key facets of reduced-order modeling for wall-bounded turbulence. First, as has become clear over the past roughly fifteen years, linear mechanisms play a fundamental role in wall-bounded turbulence. In the present investigation of EIT, a rank-1 approximation within the resolvent analysis framework highlighted the roll played by critical layers in generating dominant flow structures. Also of central importance are nonlinear interactions, which any reduced-order model must account for in order to be quantitatively accurate, and which were a major theme of the following chapter, again interpreted through the lens of resolvent analysis. Though resolvent weights leading to a closed, self-sustaining representation of the system were not computed, a statistical analysis using estimated weights still yielded valuable insight about mode interactions. The third facet, addressed here using a neural network, is data-driven techniques. We believe that resorting to them is not a call to abandon theoretical pursuits. Rather, we take the pragmatic perspective that data-driven methods can be useful or even enabling for applications, and, when used judiciously, have the potential complement theory. In summary, though they were treated separately here, it is our view that the most successful reduced-order turbulence models will employ all three of these facets in some fashion. Therefore, further work developing both the individual areas, as well as a framework to combine them is highly valuable.

BIBLIOGRAPHY

- Abadi, M., Agarwal, A., Barham, P., Brevdo, E., Chen, Z., Citro, C., Corrado, G. S., Davis, A., Dean, J., Devin, M., Ghemawat, S., Goodfellow, I., Harp, A., Irving, G., Isard, M., Jia, Y., Jozefowicz, R., Kaiser, L., Kudlur, M., Levenberg, J., Mané, D., Monga, R., Moore, S., Murray, D., Olah, C., Schuster, M., Shlens, J., Steiner, B., Sutskever, I., Talwar, K., Tucker, P., Vanhoucke, V., Vasudevan, V., Viégas, F., Vinyals, O., Warden, P., Wattenberg, M., Wicke, M., Yu, Y., and Zheng, X. (2015). *TensorFlow: Large-Scale Machine Learning on Heterogeneous Systems*. Software available from tensorflow.org.
- Adrian, R. J. (2007). “Hairpin vortex organization in wall turbulence”. *Physics of Fluids* 19.4, p. 041301.
- Ahmed, M. A. and Sharma, A. S. (2020). “Basis for finding exact coherent states”. *Physical Review E* 101 (1), p. 012213.
- Balci, N., Thomases, B., Renardy, M., and Doering, C. R. (2011). “Symmetric factorization of the conformation tensor in viscoelastic fluid models”. *Journal of Non-Newtonian Fluid Mechanics* 166.11, pp. 546–553.
- Beneddine, S., Sipp, D., Arnault, A., Dandois, J., and Lesshafft, L. (2016). “Conditions for validity of mean flow stability analysis”. *Journal of Fluid Mechanics* 798, pp. 485–504.
- Beris, A. N. and Edwards, B. J. (1994). *Thermodynamics of Flowing Systems with Internal Microstructure*. Oxford University Press.
- Bird, R. B., Armstrong, R. C., and Hassager, O. (1987). *Dynamics of polymeric liquids. Vol. 1: Fluid mechanics*. 2nd ed. Vol. 1. John Wiley and Sons Inc., New York, NY.
- Bistagnino, A., Boffetta, G., Celani, A., Mazzino, A., Puliafito, A., and Vergassola, M. (2007). “Nonlinear dynamics of the viscoelastic Kolmogorov flow”. *Journal of Fluid Mechanics* 590, pp. 61–80.
- Burger, E. D., Chorn, L. G., and Perkins, T. K. (1980). “Studies of drag reduction conducted over a broad range of pipeline conditions when flowing Prudhoe Bay crude oil”. *Journal of Rheology (1978-present)* 24.5, pp. 603–626.
- Burger, E. D., Munk, W. R., and Wahl, H. A. (1982). “Flow increase in the Trans-Alaska Pipeline through use of a polymeric drag-reducing additive”. *Journal of Petroleum Technology* 34.02, pp. 377–386.
- Chaudhary, I., Garg, P., Shankar, V., and Subramanian, G. (2019). “Elasto-inertial wall mode instabilities in viscoelastic plane Poiseuille flow”. *Journal of Fluid Mechanics* 881, pp. 119–163.
- Chollet, F. et al. (2015). *Keras*. <https://keras.io>.

- Choueiri, G. H., Lopez, J. M., and Hof, B. (2018). “Exceeding the Asymptotic Limit of Polymer Drag Reduction”. *Physical Review Letters* 120.12, p. 124501.
- Clever, R. M. and Busse, F. H. (1997). “Tertiary and quaternary solutions for plane Couette flow”. *Journal of Fluid Mechanics* 344, pp. 137–153.
- Cossu, C., Pujals, G., and Depardon, S. (2009). “Optimal transient growth and very large-scale structures in turbulent boundary layers”. *Journal of Fluid Mechanics* 619, pp. 79–94.
- Cruz, D., Pinho, F., and Oliveira, P. (2005). “Analytical solutions for fully developed laminar flow of some viscoelastic liquids with a Newtonian solvent contribution”. *Journal of Non-Newtonian Fluid Mechanics* 132.1, pp. 28–35.
- Dawson, S. T. M. and McKeon, B. J. (2019). “On the shape of resolvent modes in wall-bounded turbulence”. *Journal of Fluid Mechanics* 877, pp. 682–716.
- de Gennes, P.-G. (1990). *Introduction to polymer dynamics*. Cambridge University Press Archive.
- del Álamo, J. C. and Jiménez, J. (2006). “Linear energy amplification in turbulent channels”. *Journal of Fluid Mechanics* 559, pp. 205–213.
- Doering, C. R., Eckhardt, B., and Schumacher, J. (2006). “Failure of energy stability in Oldroyd-B fluids at arbitrarily low Reynolds numbers”. *Journal of Non-Newtonian Fluid Mechanics* 135.2-3, pp. 92–96.
- Drazin, P. G. and Reid, W. H. (2004). *Hydrodynamic Stability*. 2nd ed. Cambridge Mathematical Libraries. Cambridge University Press.
- Driscoll, T. A., Hale, N., and Trefethen, L. N. (2014). *Chebfun guide*.
- Dubief, Y., Terrapon, V. E., and Soria, J. (2013). “On the mechanism of elasto-inertial turbulence”. *Physics of Fluids* 25.11, p. 110817.
- Dubief, Y., Terrapon, V. E., White, C. M., Shaqfeh, E. S., Moin, P., and Lele, S. K. (2005). “New answers on the interaction between polymers and vortices in turbulent flows”. *Flow, Turbulence and Combustion* 74.4, pp. 311–329.
- Dubief, Y., White, C. M., Terrapon, V. E., Shaqfeh, E. S. G., Moin, P., and Lele, S. K. (2004). “On the coherent drag-reducing and turbulence-enhancing behaviour of polymers in wall flows”. *Journal of Fluid Mechanics* 514, pp. 271–280.
- Duguet, Y., Pringle, C. C. T., and Kerswell, R. R. (2008). “Relative periodic orbits in transitional pipe flow”. *Physics of Fluids* 20.11, p. 114102.
- Elsnab, J. R., Monty, J. P., White, C. M., Koochesfahani, M. M., and Klewicki, J. C. (2019). “High-fidelity measurements in channel flow with polymer wall injection”. *Journal of Fluid Mechanics* 859, pp. 851–886.
- Faisst, H. and Eckhardt, B. (2003). “Traveling waves in pipe flow”. *Physical Review Letters* 91 (22), p. 224502.

- Garg, P., Chaudhary, I., Khalid, M., Shankar, V., and Subramanian, G. (2018). “Viscoelastic pipe flow is linearly unstable”. *Physical Review Letters* 121.2, p. 024502.
- Gibson, J. F., Halcrow, J., and Cvitanovic, P. (2009). “Equilibrium and travelling-wave solutions of plane Couette flow”. *Journal of Fluid Mechanics* 638, pp. 243–266.
- Gibson, J. F., Halcrow, J., and Cvitanović, P. (2008). “Visualizing the geometry of state space in plane Couette flow”. *Journal of Fluid Mechanics* 611, pp. 107–130.
- Gibson, J. F. (2014). *Channelflow: A spectral Navier-Stokes simulator in C++*. Tech. rep. Channelflow.org. University of New Hampshire.
- Gómez, F., Blackburn, H. M., Rudman, M., Sharma, A. S., and McKeon, B. J. (2016). “A reduced-order model of three-dimensional unsteady flow in a cavity based on the resolvent operator”. *Journal of Fluid Mechanics* 798, R2.
- Graham, M. D. (1998). “Effect of axial flow on viscoelastic Taylor-Couette instability”. *Journal of Fluid Mechanics* 360, pp. 341–374.
- Graham, M. D. (2014). “Drag reduction and the dynamics of turbulence in simple and complex fluids”. *Physics of Fluids* 26.10, pp. 625–656.
- Graham, M. D. (2018). *Microhydrodynamics, Brownian Motion, and Complex Fluids*. Vol. 58. Cambridge University Press.
- Grant, M. and Boyd, S. (2014). *CVX: Matlab Software for Disciplined Convex Programming, version 2.1*. <http://cvxr.com/cvx>.
- Groisman, A. and Steinberg, V. (2000). “Elastic turbulence in a polymer solution flow”. *Nature* 405.6782, pp. 53–55.
- Groisman, A. and Steinberg, V. (2001). “Efficient mixing at low Reynolds numbers using polymer additives”. *Nature* 410.6831, pp. 905–908.
- Guala, M., Hommema, S. E., and Adrian, R. J. (2006). “Large-scale and very-large-scale motions in turbulent pipe flow”. *Journal of Fluid Mechanics* 554, pp. 521–542.
- Halko, N., Martinsson, P. G., and Tropp, J. A. (2011). “Finding Structure with Randomness: Probabilistic Algorithms for Constructing Approximate Matrix Decompositions”. *SIAM Review* 53.2, pp. 217–288.
- Hall, P. and Sherwin, S. (2010). “Streamwise vortices in shear flows: harbingers of transition and the skeleton of coherent structures”. *Journal of Fluid Mechanics* 661, pp. 178–205.
- Hameduddin, I., Gayme, D. F., and Zaki, T. A. (2019). “Perturbative expansions of the conformation tensor in viscoelastic flows”. *Journal of Fluid Mechanics* 858, pp. 377–406.
- Hameduddin, I., Meneveau, C., Zaki, T. A., and Gayme, D. F. (2018). “Geometric decomposition of the conformation tensor in viscoelastic turbulence”. *Journal of Fluid Mechanics* 842, pp. 395–427.

- Hameduddin, I. and Zaki, T. A. (2019). “The mean conformation tensor in viscoelastic turbulence”. *Journal of Fluid Mechanics* 865, pp. 363–380.
- Hamilton, J. M., Kim, J., and Waleffe, F. (1995). “Regeneration mechanisms of near-wall turbulence structures”. *Journal of Fluid Mechanics* 287, pp. 317–348.
- Haward, S. J. and McKinley, G. H. (2013). “Instabilities in stagnation point flows of polymer solutions”. *Physics of Fluids* 25.8, p. 083104.
- Haward, S. J., Page, J., Zaki, T. A., and Shen, A. Q. (2018). “Inertioelastic Poiseuille flow over a wavy surface”. *Physical Review Fluids* 3.9, p. 091302.
- Hoda, N., Jovanović, M. R., and Kumar, S. (2008). “Energy amplification in channel flows of viscoelastic fluids”. *Journal of Fluid Mechanics* 601.
- Hoda, N., Jovanović, M. R., and Kumar, S. (2009). “Frequency responses of streamwise-constant perturbations in channel flows of Oldroyd-B fluids”. *Journal of Fluid Mechanics* 625, pp. 411–434.
- Hoyas, S. and Jiménez, J. (2006). “Scaling of the velocity fluctuations in turbulent channels up to $Re_\tau = 2003$ ”. *Physics of Fluids* 18.1, p. 011702.
- Huang, Y. and Palomar, D. P. (2010). “Rank-constrained separable semidefinite programming with applications to optimal beamforming”. *IEEE Transactions on Signal Processing* 58.2, pp. 664–678.
- Hunt, J. C., Wray, A. A., and Moin, P. (1988). “Eddies, streams, and convergence zones in turbulent flows”. *Studying Turbulence Using Numerical Simulation Databases, 2. Proceedings of the 1988 Summer Program*. Center for Turbulence Research, Stanford University, pp. 193–208.
- Hutchins, N. and Marusic, I. (2007). “Evidence of very long meandering features in the logarithmic region of turbulent boundary layers”. *Journal of Fluid Mechanics* 579, pp. 1–28.
- Hwang, Y. and Cossu, C. (2010). “Linear non-normal energy amplification of harmonic and stochastic forcing in the turbulent channel flow”. *Journal of Fluid Mechanics* 664, pp. 51–73.
- Hwang, Y. (2016). “Mesolayer of attached eddies in turbulent channel flow”. *Physical Review Fluids* 1 (6), p. 064401.
- Illingworth, S. J., Monty, J. P., and Marusic, I. (2018). “Estimating large-scale structures in wall turbulence using linear models”. *Journal of Fluid Mechanics* 842, pp. 146–162.
- Itano, T. and Generalis, S. C. (2009). “Hairpin vortex solution in planar Couette Flow: A tapestry of knotted vortices”. *Physical Review Letters* 102 (11), p. 114501.
- Jovanović, M. R. and Bamieh, B. (2005). “Componentwise energy amplification in channel flows”. *Journal of Fluid Mechanics* 534, pp. 145–183.

- Jovanović, M. R. and Kumar, S. (2010). “Transient growth without inertia”. *Physics of Fluids* 22.2, p. 023101.
- Jovanović, M. R. and Kumar, S. (2011). “Nonmodal amplification of stochastic disturbances in strongly elastic channel flows”. *Journal of Non-Newtonian Fluid Mechanics* 166.14-15, pp. 755–778.
- Juttijudata, V., Lumley, J. L., and Rempfer, D. (2005). “Proper orthogonal decomposition in Squire’s coordinate system for dynamical models of channel turbulence”. *Journal of Fluid Mechanics* 534, pp. 195–225.
- Kawahara, G. and Kida, S. (2001). “Periodic motion embedded in plane Couette turbulence: regeneration cycle and burst”. *Journal of Fluid Mechanics* 449, pp. 291–300.
- Kawahara, G., Uhlmann, M., and van Veen, L. (2012). “The significance of simple invariant solutions in turbulent flows”. *Annual Review of Fluid Mechanics* 44.1, pp. 203–225.
- Kim, K., Adrian, R. J., Balachandar, S., and Sureshkumar, R. (2008). “Dynamics of Hairpin Vortices and Polymer-Induced Turbulent Drag Reduction”. *Physical Review Letters* 100 (13), p. 134504.
- Kim, K. C. and Adrian, R. J. (1999). “Very large-scale motion in the outer layer”. *Physics of Fluids* 11.2, pp. 417–422.
- Kingma, D. P. and Ba, J. L. (2015). “Adam: A method for stochastic gradient descent”. *ICLR: International Conference on Learning Representations*.
- Klewicki, J., Fife, P., and Wei, T. (2009). “On the logarithmic mean profile”. *Journal of Fluid Mechanics* 638, pp. 73–93.
- Kupferman, R. (2005). “On the linear stability of plane Couette flow for an Oldroyd-B fluid and its numerical approximation”. *Journal of Non-Newtonian Fluid Mechanics* 127.2-3, pp. 169–190.
- L’vov, V. S., Pomyalov, A., Procaccia, I., and Tiberkovich, V. (2004). “Drag reduction by polymers in wall bounded turbulence”. *Physical Review Letters* 94.24, p. 244503.
- Landahl, M. T. (1967). “A wave-guide model for turbulent shear flow”. *Journal of Fluid Mechanics* 29.3, pp. 441–459.
- Lee, S. J. and Zaki, T. A. (2017). “Simulations of natural transition in viscoelastic channel flow”. *Journal of Fluid Mechanics* 820, pp. 232–262.
- LeHew, J., Guala, M., and McKeon, B. J. (2011). “A study of the three-dimensional spectral energy distribution in a zero pressure gradient turbulent boundary layer”. *Experiments in Fluids* 51.4, pp. 997–1012.
- Lieu, B. K., Jovanović, M. R., and Kumar, S. (2013). “Worst-case amplification of disturbances in inertialess Couette flow of viscoelastic fluids”. *Journal of Fluid Mechanics* 723, pp. 232–263.

- Lieu, B. K. and Jovanović, M. R. (2013). “Computation of frequency responses for linear time-invariant PDEs on a compact interval”. *Journal of Computational Physics* 250, pp. 246–269.
- Lopez, J. M., Choueiri, G. H., and Hof, B. (2019). “Dynamics of viscoelastic pipe flow at low Reynolds numbers in the maximum drag reduction limit”. *Journal of Fluid Mechanics* 874, pp. 699–719.
- Lozano-Durán, A. and Jiménez, J. (2014). “Effect of the computational domain on direct simulations of turbulent channels up to $Re_\tau = 4200$ ”. *Physics of Fluids* 26.1, p. 011702.
- Lumley, J. L. (1969). “Drag reduction by additives”. *Annual Review of Fluid Mechanics* 1.1, pp. 367–384.
- Madhusudanan, A., Illingworth, S. J., and Marusic, I. (2019). “Coherent large-scale structures from the linearized Navier–Stokes equations”. *Journal of Fluid Mechanics* 873, pp. 89–109.
- Marusic, I., McKeon, B. J., Monkewitz, P. A., Nagib, H. M., Smits, A. J., and Sreenivasan, K. R. (2010). “Wall-bounded turbulent flows at high Reynolds numbers: Recent advances and key issues”. *Physics of Fluids* 22.6, p. 065103.
- Marusic, I., Monty, J. P., Hultmark, M., and Smits, A. J. (2013). “On the logarithmic region in wall turbulence”. *Journal of Fluid Mechanics* 716, R3.
- McKeon, B. J., Sharma, A. S., and Jacobi, I. (2013). “Experimental manipulation of wall turbulence: A systems approach”. *Physics of Fluids* 25.3, p. 031301.
- McKeon, B. J. and Sharma, A. S. (2010). “A critical-layer framework for turbulent pipe flow”. *Journal of Fluid Mechanics* 658, pp. 336–382.
- Moarref, R., Jovanović, M. R., Tropp, J. A., Sharma, A. S., and McKeon, B. J. (2014a). “A low-order decomposition of turbulent channel flow via resolvent analysis and convex optimization”. *Physics of Fluids* 26.5, p. 051701.
- Moarref, R., Sharma, A. S., Tropp, J. A., and McKeon, B. J. (2013a). “Model-based scaling of the streamwise energy density in high-Reynolds-number turbulent channels”. *Journal of Fluid Mechanics* 734, pp. 275–316.
- Moarref, R., Sharma, A. S., Tropp, J. A., and McKeon, B. J. (2013b). “On effectiveness of a rank-1 model of turbulent channels for representing the velocity spectra”. *AIAA 43rd Fluid Dynamics Conference*.
- Moarref, R., Sharma, A. S., Tropp, J. A., and McKeon, B. J. (2014b). “A foundation for analytical developments in the logarithmic region of turbulent channels”. arXiv: 1409.6047 [physics.flu-dyn].
- Nagata, M. (1990). “Three-dimensional finite-amplitude solutions in plane Couette flow: Bifurcation from infinity”. *Journal of Fluid Mechanics* 217, pp. 519–527.
- Nagata, M. (1997). “Three-dimensional travelling-wave solutions in plane Couette flow”. *Physical Review E* 55, p. 20232025.

- Page, J. and Kerswell, R. R. (2020). “Searching turbulence for periodic orbits with dynamic mode decomposition”. *Journal of Fluid Mechanics* 886, A28.
- Page, J. and Zaki, T. A. (2015). “The dynamics of spanwise vorticity perturbations in homogeneous viscoelastic shear flow”. *Journal of Fluid Mechanics* 777, pp. 327–363.
- Park, J. S. and Graham, M. D. (2015). “Exact coherent states and connections to turbulent dynamics in minimal channel flow”. *J. Fluid Mech.* 782, pp. 430–454.
- Pringle, C. C. T. and Kerswell, R. R. (2007). “Asymmetric, helical, and mirror-symmetric traveling waves in pipe flow”. *Physical Review Letters* 99 (7), p. 074502.
- Renardy, M. (2006). “A comment on smoothness of viscoelastic stresses”. *Journal of Non-Newtonian Fluid Mechanics* 138.2, pp. 204–205.
- Rosenberg, K. (2018). “Resolvent-based modeling of flows in a channel”. PhD thesis. California Institute of Technology.
- Rosenberg, K. and McKeon, B. J. (2019a). “Computing exact coherent states in channels starting from the laminar profile: A resolvent-based approach”. *Physical Review E* 100 (2), p. 021101.
- Rosenberg, K. and McKeon, B. J. (2019b). “Efficient representation of exact coherent states of the Navier–Stokes equations using resolvent analysis”. *Fluid Dynamics Research* 51.1, p. 011401.
- Rosenberg, K., Symon, S., and McKeon, B. J. (2019). “Role of parasitic modes in nonlinear closure via the resolvent feedback loop”. *Physical Review Fluids* 4 (5), p. 052601.
- Samanta, D., Dubief, Y., Holzner, M., Schäfer, C., Morozov, A. N., Wagner, C., and Hof, B. (2013). “Elasto-inertial turbulence”. *Proceedings of the National Academy of Sciences* 110.26, pp. 10557–10562.
- Schmid, P. J. (2007). “Nonmodal stability theory”. *Annual Review of Fluid Mechanics* 39, pp. 129–162.
- Schmid, P. J. (2010). “Dynamic mode decomposition of numerical and experimental data”. *Journal of Fluid Mechanics* 656, pp. 5–28.
- Schmid, P. J. and Henningson, D. S. (2001). *Stability and transition in shear flows*. Springer.
- Sharma, A. S. and McKeon, B. J. (2013). “On coherent structure in wall turbulence”. *Journal of Fluid Mechanics* 728, pp. 196–238.
- Sharma, A. S., Moarref, R., and McKeon, B. J. (2017). “Scaling and interaction of self-similar modes in models of high Reynolds number wall turbulence”. *Philosophical Transactions of the Royal Society A: Mathematical, Physical and Engineering Sciences* 375.2089, p. 20160089.

- Sharma, A. S., Moarref, R., McKeon, B. J., Park, J. S., Graham, M. D., and Willis, A. P. (2016). “Low-dimensional representations of exact coherent states of the Navier-Stokes equations from the resolvent model of wall turbulence”. *Physical Review E* 93 (2), p. 021102.
- Shekar, A., McMullen, R. M., McKeon, B. J., and Graham, M. D. (2020). “Self-sustained elastoinertial Tollmien-Schlichting waves”. *Journal of Fluid Mechanics*. To appear.
- Shekar, A., McMullen, R. M., Wang, S.-N., McKeon, B. J., and Graham, M. D. (2019). “Critical-layer structures and mechanisms in elastoinertial turbulence”. *Physical Review Letters* 122 (12), p. 124503.
- Sid, S., Terrapon, V. E., and Dubief, Y. (2018). “Two-dimensional dynamics of elasto-inertial turbulence and its role in polymer drag reduction”. *Physical Review Fluids* 3.1, p. 011301.
- Smits, A. J. and Marusic, I. (2013). “Wall-bounded turbulence”. *Physics Today* 66.9, pp. 25–30.
- Sreenivasan, K. R. and White, C. M. (2000). “The onset of drag reduction by dilute polymer additives, and the maximum drag reduction asymptote”. *Journal of Fluid Mechanics* 409, pp. 149–164.
- Sureshkumar, R. and Beris, A. N. (1995a). “Effect of artificial stress diffusivity on the stability of numerical calculations and the flow dynamics of time-dependent viscoelastic flows”. *Journal of Non-Newtonian Fluid Mechanics* 60.1, pp. 53–80.
- Sureshkumar, R. and Beris, A. N. (1995b). “Linear stability analysis of viscoelastic Poiseuille flow using an Arnoldi-based orthogonalization algorithm”. *Journal of Non-Newtonian Fluid Mechanics* 56.2, pp. 151–182.
- Tabor, M. and de Gennes, P.-G. (1986). “A cascade theory of drag reduction”. *Europhysics Letters (EPL)* 2.7, pp. 519–522.
- Terrapon, V. E., Dubief, Y., and Soria, J. (2014). “On the role of pressure in elasto-inertial turbulence”. *Journal of Turbulence* 16.1, pp. 26–43.
- Toedtli, S. S., Luhar, M., and McKeon, B. J. (2019). “Predicting the response of turbulent channel flow to varying-phase opposition control: Resolvent analysis as a tool for flow control design”. *Physical Review Fluids* 4 (7), p. 073905.
- Toms, B. A. (1948). “Some observations on the flow of linear polymer solutions through straight tubes at large Reynolds numbers”. *Proceedings of the 1st International Congress on Rheology*. Vol. 2, pp. 135–141.
- Towne, A., Lozano-Durán, A., and Yang, X. (2020). “Resolvent-based estimation of space–time flow statistics”. *Journal of Fluid Mechanics* 883, A17.
- Towne, A., Schmidt, O. T., and Colonius, T. (2018). “Spectral proper orthogonal decomposition and its relationship to dynamic mode decomposition and resolvent analysis”. *Journal of Fluid Mechanics* 847, pp. 821–867.

- Townsend, A. A. (1961). "Equilibrium layers and wall turbulence". *Journal of Fluid Mechanics* 11.1, pp. 97–120.
- Trefethen, L. N., Trefethen, A. E., Reddy, S., and Driscoll, T. A. (1993). "Hydrodynamic stability without eigenvalues". *Science* 261.5121.
- Vadarevu, S. B., Symon, S., Illingworth, S. J., and Marusic, I. (2019). "Coherent structures in the linearized impulse response of turbulent channel flow". *Journal of Fluid Mechanics* 863, pp. 1190–1203.
- Virk, P. S., Mickley, H. S., and Smith, K. A. (1970). "The ultimate asymptote and mean flow structure in Toms' phenomenon". *Journal of Applied Mechanics* 37.2, pp. 488–493.
- Virk, P. S. (1975). "Drag reduction fundamentals". *AIChE Journal* 21.4, pp. 625–656.
- Virk, P. S., Merrill, E. W., Mickley, H. S., Smith, K. A., and Mollo-Christensen, E. L. (1967). "The Toms phenomenon: turbulent pipe flow of dilute polymer solutions". *Journal of Fluid Mechanics* 30.2, pp. 305–328.
- Viswanath, D. (2007a). "Recurrent motions within plane Couette turbulence". *J. Fluid Mech.* 580, pp. 339–358.
- Viswanath, D. (2007b). "Recurrent motions within plane Couette turbulence". *Journal of Fluid Mechanics* 580, pp. 339–358.
- Waleffe, F. (1998). "Three-dimensional coherent states in plane shear flows". *Physical Review Letters* 81 (19), pp. 4140–4143.
- Waleffe, F. (2001). "Exact coherent structures in channel flow". *Journal of Fluid Mechanics* 435, pp. 93–102.
- Wang, S.-N., Graham, M. D., Hahn, F. J., and Xi, L. (2014). "Time-series and extended Karhunen–Loève analysis of turbulent drag reduction in polymer solutions". *AIChE Journal* 60.4, pp. 1460–1475.
- Warholic, M. D., Heist, D. K., Katcher, M., and Hanratty, T. J. (2001). "A study with particle-image velocimetry of the influence of drag-reducing polymers on the structure of turbulence". *Experiments in Fluids* 31.5, pp. 474–483.
- Weideman, J. A. and Reddy, S. C. (2000). "A MATLAB differentiation matrix suite". *ACM Transactions on Mathematical Software* 26.4, pp. 465–519.
- Whalley, R. D., Park, J. S., Kushwaha, A., Dennis, D. J. C., Graham, M. D., and Poole, R. J. (2017). "Low-drag events in transitional wall-bounded turbulence". *Physical Review Fluids* 2, p. 034602.
- White, C. M., Dubief, Y., and Klewicki, J. (2012). "Re-examining the logarithmic dependence of the mean velocity distribution in polymer drag reduced wall-bounded flow". *Physics of Fluids* 24.2, p. 021701.

- White, C. M., Dubief, Y., and Klewicki, J. (2018). “Properties of the mean momentum balance in polymer drag-reduced channel flow”. *Journal of Fluid Mechanics* 834, pp. 409–433.
- White, C. M. and Mungal, M. G. (2008). “Mechanics and prediction of turbulent drag reduction with polymer additives”. *Annual Review of Fluid Mechanics* 40, pp. 235–256.
- White, C. M., Somandepalli, V. S. R., and Mungal, M. G. (2004). “The turbulence structure of drag-reduced boundary layer flow”. *Experiments in Fluids* 36.1, pp. 62–69.
- Willis, A. P., Hwang, Y., and Cossu, C. (2010). “Optimally amplified large-scale streaks and drag reduction in turbulent pipe flow”. *Physical Review E* 82 (3), p. 036321.
- Willis, A. P., Short, K. Y., and Cvitanović, P. (2016). “Symmetry reduction in high dimensions, illustrated in a turbulent pipe”. *Phys. Rev. E* 93 (2), p. 022204.
- Zare, A., Jovanović, M. R., and Georgiou, T. T. (2017). “Colour of turbulence”. *Journal of Fluid Mechanics* 812, pp. 636–680.
- Zhang, M., Lashgari, I., Zaki, T. A., and Brandt, L. (2013). “Linear stability analysis of channel flow of viscoelastic Oldroyd-B and FENE-P fluids”. *Journal of Fluid Mechanics* 737, pp. 249–279.
- Zhou, J., Adrian, R. J., Balachandar, S., and Kendall, T. M. (1999). “Mechanisms for generating coherent packets of hairpin vortices in channel flow”. *Journal of Fluid Mechanics* 387, pp. 353–396.
- Zhou, K., Doyle, J. C., and Glover, K. (1996). *Robust and optimal control*. Vol. 40. Prentice Hall.

Appendix A

ADDITIONAL DETAILS OF THE VISCOELASTIC RESOLVENT FORMULATION

A.1 Base flow

Here we provide the details of the laminar steady-state solutions $\mathbf{u} = \mathbf{U}$, $p = P$, $\tilde{\mathbf{r}} = \mathbf{R}$ to Equations (3.10)–(3.12), referred to as the base flow, for pressure-driven flow of a FENE-P fluid through an infinite channel. The streamwise, spanwise, and wall-normal coordinates are $x, z \in \mathbb{R}$, and $y \in [-1, 1]$, respectively. The velocity is subject to the no-slip condition at $y = \pm 1$. Due to the hyperbolic nature of Equation (3.12), there are no boundary conditions imposed on the conformation tensor.

The base velocity has the form $\mathbf{U} = \left(U(y) \ 0 \ 0 \right)^T$. An analytical solution is provided in Cruz et al., 2005:

$$U(y) = -\frac{Re}{2\beta} \frac{dP}{dx} (1 - y^2) - \frac{(1 - \beta)}{\beta} \frac{3}{8B} \left(F^+|_{-1}^y G^-|_{-1}^y + F^-|_{-1}^y G^+|_{-1}^y \right), \quad (\text{A.1})$$

where

$$F^\pm(y) = \left(By \pm \sqrt{B^2 y^2 + A^3} \right)^{1/3}, \quad (\text{A.2})$$

$$G^\pm(y) = 3By \pm \sqrt{B^2 y^2 + A^3}, \quad (\text{A.3})$$

and

$$A = \frac{\ell^2}{6Wi^2} \left(\frac{3}{\ell^2} + \frac{1}{\beta} \right), \quad B = \frac{\ell^2 Re}{4\beta Wi^2} \frac{dP}{dx}. \quad (\text{A.4})$$

The nonzero conformation tensor components R_{xx} , R_{yy} , R_{zz} , and R_{xy} are expressed in terms of the shear stress T_{xy} :

$$R_{xx} = \frac{\ell^2 \left(1 + 2Wi^2 T_{xy}^2 \right)}{3 + \ell^2 + 2Wi^2 T_{xy}^2}, \quad (\text{A.5})$$

$$R_{yy} = R_{zz} = \frac{\ell^2}{3 + \ell^2 + 2Wi^2 T_{xy}^2}, \quad (\text{A.6})$$

$$R_{xy} = Wi T_{xy} R_{yy}, \quad (\text{A.7})$$

where

$$T_{xy} = F^+(y) + F^-(y). \quad (\text{A.8})$$

A.2 Operator definitions

Here we provide the details of the sub-operators for the viscoelastic resolvent given in Equation (3.21). The linearized Navier-Stokes operator is

$$\mathcal{L}_{11} = \begin{pmatrix} -ik_x U + \beta Re^{-1} \Delta & -U' & 0 & -ik_x \\ 0 & -ik_x U + \beta Re^{-1} \Delta & 0 & \mathcal{D} \\ 0 & 0 & -ik_x U + \beta Re^{-1} \Delta & -ik_z \\ -ik_x & -\mathcal{D} & -ik_z & 0 \end{pmatrix}, \quad (\text{A.9})$$

where $\Delta := \mathcal{D}^2 - k^2$, with $\mathcal{D} := d/dy$, and $k^2 := k_x^2 + k_z^2$. The polymer advection and stretching operator is

$$\mathcal{L}_{22} = \begin{pmatrix} -ik_x U & 0 & 0 & 2U' & 0 & 0 \\ 0 & -ik_x U & 0 & 0 & 0 & 0 \\ 0 & 0 & -ik_x U & 0 & 0 & 0 \\ 0 & U' & 0 & -ik_x U & 0 & 0 \\ 0 & 0 & 0 & 0 & -ik_x U & U' \\ 0 & 0 & 0 & 0 & 0 & -ik_x U \end{pmatrix}. \quad (\text{A.10})$$

The polymer stresses in the momentum equations are represented by

$$\mathcal{L}_{12} = \frac{1 - \beta}{ReWi} \mathcal{T} \mathcal{P}, \quad (\text{A.11})$$

where

$$\mathcal{T} = \begin{pmatrix} ik_x & 0 & 0 & \mathcal{D} & ik_z & 0 \\ 0 & \mathcal{D} & 0 & ik_x & 0 & ik_z \\ 0 & 0 & ik_z & 0 & ik_x & \mathcal{D} \\ 0 & 0 & 0 & 0 & 0 & 0 \end{pmatrix}, \quad (\text{A.12})$$

and

$$\mathcal{P} = \begin{pmatrix} \bar{P} + \bar{P}^2 \ell^{-2} R_{xx} & \bar{P}^2 \ell^{-2} R_{xx} & \bar{P}^2 \ell^{-2} R_{xx} & 0 & 0 & 0 \\ \bar{P}^2 \ell^{-2} R_{yy} & \bar{P} + \bar{P}^2 \ell^{-2} R_{yy} & \bar{P}^2 \ell^{-2} R_{yy} & 0 & 0 & 0 \\ \bar{P}^2 \ell^{-2} R_{zz} & \bar{P}^2 \ell^{-2} R_{zz} & \bar{P} + \bar{P}^2 \ell^{-2} R_{zz} & 0 & 0 & 0 \\ \bar{P}^2 \ell^{-2} R_{xy} & \bar{P}^2 \ell^{-2} R_{xy} & \bar{P}^2 \ell^{-2} R_{xy} & \bar{P} & 0 & 0 \\ 0 & 0 & 0 & 0 & \bar{P} & 0 \\ 0 & 0 & 0 & 0 & 0 & \bar{P} \end{pmatrix}. \quad (\text{A.13})$$

Finally, the effects of the velocity fluctuations on the polymer field are given by

$$\mathcal{L}_{21} = \begin{pmatrix} 2(ik_x R_{xx} + R_{xy} \mathcal{D}) & -R'_{xx} & 0 \\ 0 & 2(ik_x R_{xy} + R_{yy} \mathcal{D}) - R'_{yy} & 0 \\ 0 & -R'_{zz} & 2ik_z R_{zz} \\ ik_x R_{xy} + R_{yy} \mathcal{D} & -ik_x R_{xx} + R_{xy} \mathcal{D} - R'_{xy} & 0 \\ ik_z R_{zz} & 0 & ik_x R_{xx} + R_{xy} \mathcal{D} \\ 0 & ik_z R_{zz} & ik_x R_{xy} + R_{yy} \mathcal{D} \end{pmatrix}. \quad (\text{A.14})$$

A.3 Geometric inner product

Starting from the definition of the inner product on the tangent space to the manifold of positive definite tensors, given in Hameduddin et al. (2019), we derive the norm relevant for the Fourier transforms of infinitesimal perturbations to the conformation tensor. It turns out to be the natural extension to the setting of complex matrices.

Let \mathbf{r} be an infinitesimal perturbation to the base state conformation tensor \mathbf{R} . A measure of the size of the perturbation *at the point* \mathbf{R} that is consistent with the Riemannian metric on the manifold of positive definite tensors is (Hameduddin et al., 2019)

$$[\mathbf{r}, \mathbf{r}]_{\mathbf{R}} := \text{tr} \left(\mathbf{R}^{-1} \tilde{\mathbf{r}} \right)^2 = \text{tr} \mathbf{g}^2 = [\mathbf{g}, \mathbf{g}], \quad (\text{A.15})$$

where $\mathbf{g} := \mathbf{R}^{-1/2} \mathbf{r} \mathbf{R}^{-1/2}$. A sensible global measure of the disturbance ‘‘energy’’ is thus

$$\mathcal{E} := \int_{\Omega} [\mathbf{r}, \mathbf{r}]_{\mathbf{R}} \, d\Omega \quad (\text{A.16})$$

$$= \int_{\Omega} [\mathbf{g}, \mathbf{g}] \, d\Omega \quad (\text{A.17})$$

$$= \int_{\Omega} \left(\mathbf{g}_{11}^2 + \mathbf{g}_{22}^2 + \mathbf{g}_{33}^2 + 2\mathbf{g}_{12}^2 + 2\mathbf{g}_{13}^2 + 2\mathbf{g}_{23}^2 \right) \, d\Omega \quad (\text{A.18})$$

$$= \int_{k_z} \int_{k_x} \int_{-1}^1 \left(|\hat{\mathbf{g}}_{11}|^2 + |\hat{\mathbf{g}}_{22}|^2 + |\hat{\mathbf{g}}_{33}|^2 + 2|\hat{\mathbf{g}}_{12}|^2 + 2|\hat{\mathbf{g}}_{13}|^2 + 2|\hat{\mathbf{g}}_{23}|^2 \right) \, dy \, dk_x \, dk_z \quad (\text{A.19})$$

$$= \int_{k_z} \int_{k_x} \int_{-1}^1 [\hat{\mathbf{g}}, \hat{\mathbf{g}}] \, dy \, dk_x \, dk_z, \quad (\text{A.20})$$

where the third equality is due to Parseval’s theorem. Since the base state \mathbf{R} does not depend on the transformed directions x and z , we have $\hat{\mathbf{g}} = \mathbf{R}^{-1/2} \hat{\mathbf{r}} \mathbf{R}^{-1/2}$. Note that since $\tilde{\mathbf{r}}$ and \mathbf{g} are real symmetric tensors, their Fourier transforms $\hat{\mathbf{r}}$ and $\hat{\mathbf{g}}$ are

complex symmetric (not Hermitian). Substituting for $\hat{\mathbf{g}}$ in Equation (A.20), we see that the relevant norm for the Fourier components is

$$\|\hat{\mathbf{r}}\|_{\mathbf{R}}^2 := \int_{-1}^1 \text{tr } \mathbf{R}^{-1} \hat{\mathbf{r}}^* \mathbf{R}^{-1} \hat{\mathbf{r}} \, dy, \quad (\text{A.21})$$

where the superscript $*$ denotes the conjugate transpose.

A.4 Implementation in resolvent code

The integrand in Equation (A.21) can be expanded as

$$\begin{aligned} \text{tr } \mathbf{R}^{-1} \hat{\mathbf{r}}^* \mathbf{R}^{-1} \hat{\mathbf{r}} &= \frac{R_{yy}^2}{\varrho^2} |\hat{r}_{xx}|^2 + \frac{R_{xy}^2}{\varrho^2} \left(\hat{r}_{xx}^* \hat{r}_{yy} + \hat{r}_{xx} \hat{r}_{yy}^* \right) - 2 \frac{R_{xy} R_{yy}}{\varrho^2} \left(\hat{r}_{xx}^* \hat{r}_{xy} + \hat{r}_{xx} \hat{r}_{xy}^* \right) \\ &+ \frac{R_{xx}^2}{\varrho^2} |\hat{r}_{yy}|^2 - 2 \frac{R_{xx} R_{xy}}{\varrho^2} \left(\hat{r}_{yy}^* \hat{r}_{xy} + \hat{r}_{yy} \hat{r}_{xy}^* \right) + \frac{1}{R_{zz}^2} |\hat{r}_{zz}|^2 + \frac{R_{xx} R_{yy} + R_{xy}^2}{\varrho^2} |\hat{r}_{xy}|^2 \\ &+ 2 \frac{R_{yy}}{R_{zz} \varrho} |\hat{r}_{xz}|^2 - 2 \frac{R_{xy}}{R_{zz} \varrho} \left(\hat{r}_{xz}^* \hat{r}_{yz} + \hat{r}_{xz} \hat{r}_{yz}^* \right) + 2 \frac{R_{xx}}{R_{zz} \varrho} |\hat{r}_{yz}|^2, \end{aligned} \quad (\text{A.22})$$

where $\varrho := \det \mathbf{R} / R_{zz} = R_{xx} R_{yy} - R_{xy}^2$. Defining the vectorized conformation $\hat{\boldsymbol{\phi}} := [\hat{r}_{xx}, \hat{r}_{yy}, \hat{r}_{zz}, \hat{r}_{xy}, \hat{r}_{xz}, \hat{r}_{yz}]^T$, Equation (A.22) can be expressed as a matrix-vector inner product suitable for implementation in the resolvent code:

$$\text{tr } \mathbf{R}^{-1} \hat{\mathbf{r}}^* \mathbf{R}^{-1} \hat{\mathbf{r}} = \hat{\boldsymbol{\phi}}^* \mathbf{W} \hat{\boldsymbol{\phi}}, \quad (\text{A.23})$$

with

$$\mathbf{W} = \mathbf{W}^T = \begin{pmatrix} \frac{R_{yy}^2}{\varrho^2} & \frac{R_{xy}^2}{\varrho^2} & 0 & -2 \frac{R_{xy} R_{yy}}{\varrho^2} & 0 & 0 \\ & \frac{R_{xx}^2}{\varrho^2} & 0 & -2 \frac{R_{xx} R_{xy}}{\varrho^2} & 0 & 0 \\ & & \frac{1}{R_{zz}^2} & 0 & 0 & 0 \\ & & & \frac{R_{xx} R_{yy} + R_{xy}^2}{\varrho^2} & 0 & 0 \\ & & & & 2 \frac{R_{yy}}{R_{zz} \varrho} & -2 \frac{R_{xy}}{R_{zz} \varrho} \\ & & & & & 2 \frac{R_{xx}}{R_{zz} \varrho} \end{pmatrix}. \quad (\text{A.24})$$

Appendix B

UNIVERSAL SCALING OF THE ORR-SOMMERFELD AND SQUIRE RESOLVENT OPERATORS

We derive the Reynolds number scaling for the components of the resolvent response and forcing modes belonging to the universal outer and geometrically self-similar classes described in Moarref et al. (2013a). These scalings have also been reported in Sharma et al. (2017). However, here, we perform the decomposition into OS and SQ bases (Rosenberg and McKeon, 2019b), from which it is apparent that for outer and geometrically self-similar modes, each set has a unique scaling for the singular values and forcing modes. The singular values of the OS resolvent have the same scaling as those for the full resolvent. Results for the inner class modes are not reported here since, as is apparent from Equation (4.28), the OS and SQ resolvent both exhibit the same scaling and, therefore, the same scaling as the full resolvent.

B.1 Outer class

We have

$$\mathcal{H}^{\text{OS}} = \begin{pmatrix} Re_\tau \tilde{\mathcal{H}}_{vv} \\ Re_\tau^2 \tilde{\mathcal{H}}_{\eta v} \end{pmatrix}, \quad (\text{B.1})$$

and

$$\mathcal{H}^{\text{SQ}} = Re_\tau \tilde{\mathcal{H}}_{\eta\eta}, \quad (\text{B.2})$$

where $(\tilde{\cdot})$ indicates a quantity that is Re_τ -invariant for the universal outer class. Let $\boldsymbol{\xi} = (\xi_v \ \xi_\eta)^\text{T}$ and $\boldsymbol{\varphi} = (\varphi_v \ \varphi_\eta)^\text{T}$ be left and right singular vectors of \mathcal{H} , respectively. Each set of singular vectors is orthonormal with respect to the energy inner product

$$(\mathbf{f}, \mathbf{g})_E = \int_{-1}^{-1} \mathbf{g}^* \mathbf{Q} \mathbf{f} \, dy, \quad (\text{B.3})$$

where

$$\mathbf{Q} = \begin{pmatrix} \tilde{\mathbf{Q}}_v & 0 \\ 0 & \tilde{\mathbf{Q}}_\eta \end{pmatrix}. \quad (\text{B.4})$$

Let $\boldsymbol{\psi} = C\boldsymbol{\xi} = (\psi_u \ \psi_v \ \psi_w)^\text{T}$ and $\boldsymbol{\phi} = C\boldsymbol{\varphi} = (\phi_u \ \phi_v \ \phi_w)^\text{T}$, where

$$C = \begin{pmatrix} Re_\tau^{-1} \tilde{C}_{11} & \tilde{C}_{12} \\ 1 & 0 \\ \tilde{C}_{31} & Re_\tau^{-1} \tilde{C}_{32} \end{pmatrix}. \quad (\text{B.5})$$

Response modes

Using $\tilde{k}_x = Re_\tau k_x$, $\tilde{y} = y$, $\tilde{k}_z = k_z$, continuity gives

$$\begin{aligned}\nabla \cdot \boldsymbol{\psi} &= ik_x \psi_u + \mathcal{D} \psi_v + ik_z \psi_w \\ &= iRe_\tau^{-1} \tilde{k}_x \psi_u + \tilde{\mathcal{D}} \psi_v + i\tilde{k}_z \psi_w \\ &= 0.\end{aligned}\tag{B.6}$$

Fixing $\tilde{\psi}_u = \psi_u$, we thus require $\tilde{\psi}_v = Re_\tau \psi_v$ and $\tilde{\psi}_w = Re_\tau \psi_w$. That is,

$$\tilde{\boldsymbol{\psi}} = \begin{pmatrix} \psi_u \\ Re_\tau \psi_v \\ Re_\tau \psi_w \end{pmatrix}\tag{B.7}$$

should be Re_τ -invariant for modes in the outer class.

OS singular values and forcing modes

Now, the energy inner product weighted OS resolvent is

$$\mathcal{F} \mathcal{H}^{\text{OS}} \mathcal{F}^{-1} = \begin{pmatrix} Re_\tau \tilde{\mathcal{F}}_v \tilde{\mathcal{H}}_{vv} \tilde{\mathcal{F}}_v^{-1} \\ Re_\tau^2 \tilde{\mathcal{F}}_\eta \tilde{\mathcal{H}}_{\eta v} \tilde{\mathcal{F}}_v^{-1} \end{pmatrix},\tag{B.8}$$

where $\mathcal{F}^* \mathcal{F} = \mathcal{Q}$. The (leading) singular values therefore scale as

$$\sigma^{\text{OS}} = Re_\tau^2 \tilde{\sigma}^{\text{OS}}.\tag{B.9}$$

We note that this is the same scaling as that for the singular values of the entire resolvent, i.e., without performing the OS-SQ decomposition. We then have

$$\boldsymbol{\psi}^{\text{OS}} = \frac{1}{\sigma^{\text{OS}}} C \mathcal{H}^{\text{OS}} \boldsymbol{\varphi} = \frac{1}{\tilde{\sigma}^{\text{OS}}} \begin{pmatrix} Re_\tau^{-2} \tilde{\mathcal{C}}_{11} \tilde{\mathcal{H}}_{vv} + \tilde{\mathcal{C}}_{12} \tilde{\mathcal{H}}_{\eta v} \\ Re_\tau^{-1} \tilde{\mathcal{H}}_{vv} \\ Re_\tau^{-1} \tilde{\mathcal{C}}_{31} \tilde{\mathcal{H}}_{vv} + Re_\tau^{-1} \tilde{\mathcal{C}}_{32} \tilde{\mathcal{H}}_{\eta v} \end{pmatrix} \boldsymbol{\varphi}_v,\tag{B.10}$$

and

$$\tilde{\boldsymbol{\psi}}^{\text{OS}} = \begin{pmatrix} \psi_u^{\text{OS}} \\ Re_\tau \psi_v^{\text{OS}} \\ Re_\tau \psi_w^{\text{OS}} \end{pmatrix} = \frac{1}{\tilde{\sigma}^{\text{OS}}} \begin{pmatrix} Re_\tau^{-2} \tilde{\mathcal{C}}_{11} \tilde{\mathcal{H}}_{vv} + \tilde{\mathcal{C}}_{12} \tilde{\mathcal{H}}_{\eta v} \\ \tilde{\mathcal{H}}_{vv} \\ \tilde{\mathcal{C}}_{31} \tilde{\mathcal{H}}_{vv} + \tilde{\mathcal{C}}_{32} \tilde{\mathcal{H}}_{\eta v} \end{pmatrix} \boldsymbol{\varphi}_v\tag{B.11}$$

is independent of Re_τ (to leading order) if $\tilde{\varphi}_v = \varphi_v$. Finally,

$$\boldsymbol{\phi}^{\text{OS}} = C \begin{pmatrix} \varphi_v \\ 0 \end{pmatrix} = \begin{pmatrix} Re_\tau^{-1} \tilde{\mathcal{C}}_{11} \\ 1 \\ \tilde{\mathcal{C}}_{31} \end{pmatrix} \tilde{\varphi}_v.\tag{B.12}$$

Defining $\tilde{\phi}_u^{\text{OS}} = \tilde{C}_{11}\tilde{\varphi}_v$, $\tilde{\phi}_v^{\text{OS}} = \tilde{\varphi}_v$, and $\tilde{\phi}_w^{\text{OS}} = \tilde{C}_{31}\tilde{\varphi}_v$, we have

$$\tilde{\phi}^{\text{OS}} = \begin{pmatrix} Re_\tau \phi_u^{\text{OS}} \\ \phi_v^{\text{OS}} \\ \phi_w^{\text{OS}} \end{pmatrix}. \quad (\text{B.13})$$

SQ singular values and forcing modes

Proceeding as before,

$$\mathcal{F}_\eta \mathcal{H}^{\text{SQ}} \mathcal{F}_\eta^{-1} = Re_\tau \tilde{\mathcal{F}}_\eta \tilde{\mathcal{H}}_{\eta\eta} \tilde{\mathcal{F}}_\eta^{-1}. \quad (\text{B.14})$$

Then

$$\sigma^{\text{SQ}} = Re_\tau \tilde{\sigma}^{\text{SQ}}, \quad (\text{B.15})$$

and

$$\psi^{\text{SQ}} = \frac{1}{\sigma^{\text{SQ}}} C \mathcal{H}^{\text{SQ}} \varphi = \frac{1}{\tilde{\sigma}^{\text{SQ}}} \begin{pmatrix} \tilde{C}_{12} \tilde{\mathcal{H}}_{\eta\eta} \\ 0 \\ Re_\tau^{-1} \tilde{C}_{32} \tilde{\mathcal{H}}_{\eta\eta} \end{pmatrix} \varphi_\eta, \quad (\text{B.16})$$

so that

$$\tilde{\psi}^{\text{SQ}} = \begin{pmatrix} \psi_u^{\text{SQ}} \\ 0 \\ Re_\tau \psi_w^{\text{SQ}} \end{pmatrix} = \frac{1}{\tilde{\sigma}^{\text{SQ}}} \begin{pmatrix} \tilde{C}_{12} \tilde{\mathcal{H}}_{\eta\eta} \\ 0 \\ \tilde{C}_{32} \tilde{\mathcal{H}}_{\eta\eta} \end{pmatrix} \varphi_\eta \quad (\text{B.17})$$

is independent of Re_τ if $\tilde{\varphi}_\eta = \varphi_\eta$. Then

$$\phi^{\text{SQ}} = C \begin{pmatrix} 0 \\ \varphi_\eta \end{pmatrix} = \begin{pmatrix} \tilde{C}_{12} \\ 0 \\ Re_\tau^{-1} \tilde{C}_{32} \end{pmatrix} \tilde{\varphi}_\eta. \quad (\text{B.18})$$

Defining $\tilde{\phi}_u^{\text{SQ}} = \tilde{C}_{12}\tilde{\varphi}_\eta$ and $\tilde{\phi}_w^{\text{SQ}} = \tilde{C}_{32}\tilde{\varphi}_\eta$, we have

$$\tilde{\phi}^{\text{SQ}} = \begin{pmatrix} \phi_u^{\text{SQ}} \\ 0 \\ Re_\tau \phi_w^{\text{SQ}} \end{pmatrix}. \quad (\text{B.19})$$

B.2 Geometrically self-similar class

We have

$$\mathcal{H}^{\text{OS}} = \begin{pmatrix} y_c y_c^+ \check{\mathcal{H}}_{vv} \\ y_c^+ \check{\mathcal{H}}_{\eta v} \end{pmatrix}, \quad (\text{B.20})$$

$$\mathcal{H}^{\text{SQ}} = y_c y_c^+ \check{\mathcal{H}}_{\eta\eta}, \quad (\text{B.21})$$

$$Q = \begin{pmatrix} y_c \check{Q}_v & 0 \\ 0 & y_c^3 \check{Q}_\eta \end{pmatrix}, \quad (\text{B.22})$$

and

$$C = \begin{pmatrix} y_c^{+-1} \check{C}_{11} & y_c \check{C}_{12} \\ 1 & 0 \\ \check{C}_{31} & Re_\tau^{-1} \check{C}_{32} \end{pmatrix}, \quad (\text{B.23})$$

where $(\check{\cdot})$ indicates a quantity that is y_c - and Re_τ -invariant for the geometrically self-similar class.

Response modes

Using $\check{k}_x = y_c y_c^+ k_x$, $\check{y} = y/y_c$, $\check{k}_z = y_c k_z$, continuity gives

$$\begin{aligned} \nabla \cdot \psi &= ik_x \psi_u + \mathcal{D} \psi_v + ik_z \psi_w \\ &= iy_c^{-1} y_c^{+-1} \check{k}_x \psi_u + y_c^{-1} \check{\mathcal{D}} \psi_v + iy_c^{-1} \check{k}_z \psi_w \\ &= 0. \end{aligned} \quad (\text{B.24})$$

Furthermore, the orthonormality constraint $\|\psi\| = \|\xi\|_E = 1$ imposes $\psi \sim y_c^{-1/2}$. Fixing $\check{\psi}_u = y_c^{1/2} \psi_u$, we thus require $\check{\psi}_v = y_c^{1/2} y_c^+ \psi_v$ and $\check{\psi}_w = y_c^{1/2} y_c^+ \psi_w$. That is,

$$\check{\psi} = y_c^{1/2} \begin{pmatrix} \psi_u \\ y_c^+ \psi_v \\ y_c^+ \psi_w \end{pmatrix} \quad (\text{B.25})$$

should be y_c - and Re_τ -invariant for modes in the geometrically self-similar class.

OS singular values and forcing modes

Now, the energy inner product weighted OS resolvent is

$$\mathcal{F} \mathcal{H}^{\text{OS}} \mathcal{F}^{-1} = \begin{pmatrix} y_c y_c^+ \check{\mathcal{F}}_v \check{\mathcal{H}}_{vv} \check{\mathcal{F}}_v^{-1} \\ y_c y_c^{+2} \check{\mathcal{F}}_\eta \check{\mathcal{H}}_{\eta v} \check{\mathcal{F}}_v^{-1} \end{pmatrix}. \quad (\text{B.26})$$

The (leading) singular values therefore scale as

$$\sigma^{\text{OS}} = y_c y_c^{+2} \check{\sigma}^{\text{OS}}. \quad (\text{B.27})$$

We note that this is the same scaling as that for the singular values of the entire resolvent, i.e., without performing the OS-SQ decomposition. We then have

$$\psi^{\text{OS}} = \frac{1}{\sigma^{\text{OS}}} C \mathcal{H}^{\text{OS}} \varphi = \frac{1}{\check{\sigma}^{\text{OS}}} \begin{pmatrix} y_c^{+-2} \check{C}_{11} \check{\mathcal{H}}_{vv} + \check{C}_{12} \check{\mathcal{H}}_{\eta v} \\ y_c^{+-1} \check{\mathcal{H}}_{vv} \\ y_c^{+-1} \check{C}_{31} \check{\mathcal{H}}_{vv} + y_c^{+-1} \check{C}_{32} \check{\mathcal{H}}_{\eta v} \end{pmatrix} \varphi_v. \quad (\text{B.28})$$

Thus,

$$\check{\psi}^{\text{OS}} = y_c^{1/2} \begin{pmatrix} \psi_u^{\text{OS}} \\ y_c^+ \psi_v^{\text{OS}} \\ y_c^+ \psi_w^{\text{OS}} \end{pmatrix} = \frac{y_c^{1/2}}{\check{\sigma}^{\text{OS}}} \begin{pmatrix} y_c^{+-2} \check{C}_{11} \check{\mathcal{H}}_{vv} + \check{C}_{12} \check{\mathcal{H}}_{\eta v} \\ \check{\mathcal{H}}_{vv} \\ \check{C}_{31} \check{\mathcal{H}}_{vv} + \check{C}_{32} \check{\mathcal{H}}_{\eta v} \end{pmatrix} \varphi_v \quad (\text{B.29})$$

is independent of Re_τ and y_c (to leading order) if $\check{\varphi}_v = y_c^{1/2} \varphi_v$. Finally,

$$\phi^{\text{OS}} = C \begin{pmatrix} \varphi_v \\ 0 \end{pmatrix} = y_c^{-1/2} \begin{pmatrix} y_c^{+-1} \check{C}_{11} \\ 1 \\ \check{C}_{31} \end{pmatrix} \check{\varphi}_v. \quad (\text{B.30})$$

Defining $\check{\phi}_u^{\text{OS}} = \check{C}_{11} \check{\varphi}_v$, $\check{\phi}_v^{\text{OS}} = \check{\varphi}_v$, and $\check{\phi}_w^{\text{OS}} = \check{C}_{31} \check{\varphi}_v$, we have

$$\boxed{\check{\phi}^{\text{OS}} = y_c^{1/2} \begin{pmatrix} y_c^+ \phi_u^{\text{OS}} \\ \phi_v^{\text{OS}} \\ \phi_w^{\text{OS}} \end{pmatrix}.} \quad (\text{B.31})$$

SQ singular values and forcing modes

Proceeding as before,

$$\mathcal{F}_\eta \mathcal{H}^{\text{SQ}} \mathcal{F}_\eta^{-1} = y_c y_c^+ \check{\mathcal{F}}_\eta \check{\mathcal{H}}_{\eta\eta} \check{\mathcal{F}}_\eta^{-1}. \quad (\text{B.32})$$

Then

$$\boxed{\sigma^{\text{SQ}} = y_c y_c^+ \check{\sigma}^{\text{SQ}},} \quad (\text{B.33})$$

and

$$\psi^{\text{SQ}} = \frac{1}{\sigma^{\text{SQ}}} C \mathcal{H}^{\text{SQ}} \varphi = \frac{1}{\check{\sigma}^{\text{SQ}}} \begin{pmatrix} y_c \check{C}_{12} \check{\mathcal{H}}_{\eta\eta} \\ 0 \\ Re_\tau^{-1} \check{C}_{32} \check{\mathcal{H}}_{\eta\eta} \end{pmatrix} \varphi_\eta, \quad (\text{B.34})$$

so that

$$\check{\psi}^{\text{SQ}} = y_c^{1/2} \begin{pmatrix} \psi_u^{\text{SQ}} \\ 0 \\ y_c^+ \psi_w^{\text{SQ}} \end{pmatrix} = \frac{y_c^{1/2}}{\check{\sigma}^{\text{SQ}}} \begin{pmatrix} y_c \check{C}_{12} \check{\mathcal{H}}_{\eta\eta} \\ 0 \\ y_c \check{C}_{32} \check{\mathcal{H}}_{\eta\eta} \end{pmatrix} \varphi_\eta \quad (\text{B.35})$$

is independent of Re_τ and y_c if $\check{\varphi}_\eta = y_c^{3/2} \varphi_\eta$. Then

$$\phi^{\text{SQ}} = C \begin{pmatrix} 0 \\ \varphi_\eta \end{pmatrix} = y_c^{-3/2} \begin{pmatrix} y_c \check{C}_{12} \\ 0 \\ Re_\tau^{-1} \check{C}_{32} \end{pmatrix} \check{\varphi}_\eta. \quad (\text{B.36})$$

Defining $\check{\phi}_u^{\text{SQ}} = \check{C}_{12}\check{\varphi}_\eta$ and $\check{\phi}_w^{\text{SQ}} = \check{C}_{32}\check{\varphi}_\eta$, we have

$$\check{\phi}^{\text{SQ}} = y_c^{1/2} \begin{pmatrix} \phi_u^{\text{SQ}} \\ 0 \\ y_c^+ \phi_w^{\text{SQ}} \end{pmatrix}.$$

(B.37)